

VARIABILITY-AWARE LOW-POWER TECHNIQUES  
FOR NANOSCALE MIXED-SIGNAL CIRCUITS

Dhruva V. Ghai, B.E., M.Tech.

Dissertation Prepared for the Degree of  
DOCTOR OF PHILOSOPHY

UNIVERSITY OF NORTH TEXAS

May 2009

APPROVED:

Saraju P. Mohanty, Major Professor  
Elias Kougianos, Co-Major Professor  
Murali Varanasi, Committee Member  
Armin Mikler, Committee Member  
and Coordinator of Graduate Studies  
Krishna Kavi, Chair of the Department  
of Computer Science and Engineering  
Costas Tsatsoulis, Dean of College of  
Engineering  
Michael Monticino, Interim Dean of the Robert  
B. Toulouse School of Graduate Studies

Ghai, Dhruva V. Variability-aware low-power techniques for nanoscale mixed-signal circuits. Doctor of Philosophy (Computer Science and Engineering), May 2009, 131 pp., 27 tables, 63 illustrations, 130 references.

New circuit design techniques that accommodate lower supply voltages necessary for portable systems need to be integrated into the semiconductor intellectual property (IP) core. Systems that once worked at 3.3 V or 2.5 V now need to work at 1.8 V or lower, without causing any performance degradation. Also, the fluctuation of device characteristics caused by process variation in nanometer technologies is seen as design yield loss. The numerous parasitic effects induced by layouts, especially for high-performance and high-speed circuits, pose a problem for IC design. Lack of exact layout information during circuit sizing leads to long design iterations involving time-consuming runs of complex tools. There is a strong need for low-power, high-performance, parasitic-aware and process-variation-tolerant circuit design. This dissertation proposes methodologies and techniques to achieve variability, power, performance, and parasitic-aware circuit designs. Three approaches are proposed: the single iteration automatic approach, the hybrid Monte Carlo and design of experiments (DOE) approach, and the corner-based approach. Widely used mixed-signal circuits such as analog-to-digital converter (ADC), voltage controlled oscillator (VCO), voltage level converter and active pixel sensor (APS) have been designed at nanoscale complementary metal oxide semiconductor (CMOS) and subjected to the proposed methodologies. The effectiveness of the proposed methodologies has been demonstrated through exhaustive simulations. Apart from these methodologies, the application of dual-oxide and dual-threshold techniques at circuit level in order to minimize power and leakage is also explored.

Copyright 2009

by

Dhruva V. Ghai

## ACKNOWLEDGMENTS

The writing of a dissertation is not possible without the personal and practical support of numerous people. I would like to express my profound gratitude and deep appreciation to my major professor, Dr. Saraju P. Mohanty, and my co-major professor, Dr. Elias Kougianos, for supervising my overall research and guiding me throughout the course of my Ph.D. Without their help and guidance this research would not have been possible. The numerous brainstorming sessions with them helped me to not only embolden my knowledge but also to cultivate new ideas. I am grateful to my doctoral committee member, Dr. Armin Mikler, for offering his insight and spending his valuable time in reviewing my dissertation. I also thank Dr. Murali Varanasi for being on my doctoral committee and offering guidance. I would like to acknowledge the National Science Foundation for funding my research through NSF award number 0702361. Thanks to my colleagues at VDCL (VLSI Design and CAD Laboratory), Garima, Ruchi, Manish and Sahasan, for lively discussions, insightful comments, and honest opinions on my research. Finally, I would like to thank my family, who encouraged me to join the Ph.D. program at UNT and supported me throughout.

# TABLE OF CONTENTS

	Page
ACKNOWLEDGMENTS.....	iii
LIST OF TABLES .....	viii
LIST OF FIGURES.....	x
Chapter	
1. INTRODUCTION AND MOTIVATION .....	1
1.1. Issues Faced by Digital, Analog, and Mixed-Signal Circuits .....	3
1.1.1. Technology Scaling.....	3
1.1.2. Power Performance .....	5
1.1.3. Process Variation .....	5
1.1.4. Parasitics.....	6
1.1.5. Temperature Variation .....	6
1.2. Organization of This Dissertation .....	7
2. THEORETICAL BACKGROUND.....	9
2.1. Emerging Technologies .....	9
2.1.1. Nanoscale CMOS (Nano-CMOS).....	11
2.1.2. High- $\kappa$ /Metal Gate.....	15
2.1.3. Fin FET/Dual-Gate FET .....	16
2.1.4. Carbon Nanotube (CNT) .....	18
2.2. Power Leakage and Delay Models.....	20
2.2.1. Dynamic Power .....	21
2.2.4. Total Power Dissipation.....	23
2.2.5. Delay Model .....	23

2.3. Low-Power Design Techniques.....	24
2.3.1. Dual Threshold (Dual $V_T$ )	
.....	26
2.3.2. Dual Oxide (Dual $T_{ox}$ )	
.....	26
2.3.3. Dual Supply (Dual $V_{dd}$ ).....	
27	
3. RELATED PRIOR RESEARCH .....	29
3.1. Dual Supply and Dual Threshold .....	29
3.2. Dual Oxide.....	30
3.3. Process Variation.....	31
3.4. Parasitics.....	31
3.5. Literature Related to Mixed-Signal Circuits .....	32
3.5.1. Analog-to-digital Converters .....	32
3.5.2. Voltage-controlled Oscillators .....	33
3.5.3. Level Converters.....	35
3.5.4. Active Pixel Sensors .....	37
4. PROPOSED LOW-POWER DESIGN AND OPTIMIZATION METHODOLOGIES.....	39
4.1. Issue of Process Variation.....	39
4.2. Single-Iteration Automatic Approach.....	41
Algorithm Used for Optimization in the Single-iteration Automatic Approach.....	44
4.3. Hybrid Monte Carlo and Design of Experiments (DOE) Approach.....	46
Proposed Monte Carlo/DOE-based Algorithm for Variability-Aware Optimization .....	46

4.4. Corner-based Methodology .....	49
5. CASE STUDIES USING SAMPLE DIGITAL, ANALOG AND MIXED-SIGNAL CIRCUITS .....	51
5.1. Analog-to-digital Converter.....	51
5.1.1. Comparator Design .....	52
5.1.2. 1 of $n$ Code Generator Design.....	54
5.1.3. NOR ROM Design.....	55
5.1.4. Physical Design and Characterization of ADC.....	56
5.1.5. Transistor-Level Design and Characterization of the ADC at 45 nm Technology .....	63
5.2. Voltage-controlled Oscillator (VCO) .....	68
5.3. Universal Voltage Level Converter (ULC) .....	71
5.3.1. Design of ULC .....	72
5.4. Active Pixel Sensor (APS) .....	80
5.4.1. Models for the Figures of Merit of the APS array.....	84
6. PROCESS VARIATION ANALYSIS AND DESIGN OPTIMIZATION .....	86
6.1. Analog-to-digital Converter (ADC) .....	86
6.1.1. Process and Supply Variation .....	86
6.1.2. Temperature Variation Characterization .....	88
6.2. Voltage-controlled Oscillator (VCO) .....	89
6.2.1. Parasitic-aware Optimization .....	89
6.2.2. Process Variation Study .....	93
6.2.3. Parasitic- and Process-variation-aware Optimization .....	97

6.2.4. Physical Design of the Optimal VCO .....	102
6.3. Universal Voltage Level Converter (ULC).....	102
6.3.1. Dual $T_{ox}$ Technique .....	102
6.3.2. Dual $V_T$ Technique .....	104
6.3.3. Characterization .....	105
6.4. Active Pixel Sensor (APS) .....	109
7. CONCLUSION AND FUTURE WORKS .....	119
7.1. Summary .....	119
7.2. Conclusions .....	119
7.3. Future Research .....	122
REFERENCES .....	123



## LIST OF TABLES

	Page
Table 3.1. Comparative Perspective of Existing 6-bit Flash ADCs .....	33
Table 3.2. VCO Performance Comparison .....	34
Table 3.3. Comparative Perspective of Level-converters .....	37
Table 3.4. Comparative Perspective of Existing APS Designs .....	38
Table 5.1. Componentwise Power Consumption of ADC .....	61
Table 5.2 ADC Performance with Nominal Supply and Threshold Voltages .....	62
Table 5.3. Comparator Transistor Sizes for Input Voltage Range at 45 nm Technology .....	64
Table 5.4. ADC Performance at 45 nm Technology .....	67
Table 5.5. Truth Table for Functionality of Baseline ULC Design .....	72
Table 5.6. Transistor Sizes .....	81
Table 5.7. Baseline Characterization of APS Array .....	85
Table 6.1 Process Variation Results .....	87
Table 6.2. Supply Voltage Variation Results .....	88
Table 6.3. Effect of Temperature Variation .....	89
Table 6.4. Final Values of the Design Variables fro Parasitic-aware Design .....	91
Table 6.5. Measured Performance of the Parasitic-aware VCO .....	91
Table 6.6. Mean and Standard Deviation of Oscillation Frequency for 5 Cases .....	96
Table 6.7. Frequency Discrepancy and Worst-case Process Values for a Target Frequency $\geq 2$ GHz .....	97
Table 6.8. Final Optimal Values for Design Variables .....	99
Table 6.9. Performance Summary of the Parasitic and Process-variation-aware VCO .....	101

Table 6.10. Final Values of the Optimization Parameters Using the DOX-CMOS Technique .	103
Table 6.11. Optimal Design Variable Values Using the DVTCMOS Technique .....	104
Table 6.12. Power Consumption .....	109
Table 6.13. Monte Carlo Simulation Results .....	113
Table 6.14. Baseline and Optimal Values of the Figures of Merit .....	117
Table 7.1. Comparison of Results of Optimization Approaches .....	121

## LIST OF FIGURES

	Page
Figure 2.1. Various leakage currents in a nanoscale CMOS transistor. ....	14
Figure 2.2. Structure of high- $\kappa$ metal gate transistor. ....	16
Figure 2.3. Structure of the fin FET transistor. ....	18
Figure 2.4. Structure of a CNT transistor. ....	20
Figure 4.1. Standard IC design flow. ....	42
Figure 4.2. Proposed parasitic-aware IC design flow. ....	43
Figure 4.3 Parasitic- and process-variation-aware IC design flow ....	45
Figure 4.4. Aim of the hybrid Monte Carlo and DOE-based optimization. ....	49
Figure 4.5. The corner-based methodology used for process variation. ....	50
Figure 5.1. High-level representation of the ADC. ....	52
Figure 5.2. Detailed block diagram of the flash ADC. ....	52
Figure 5.3. Threshold inverter (TI) comparator. ....	54
Figure 5.4. Complete circuit diagram for a 3-bit flash ADC shown for brevity. ....	55
Figure 5.5. Complete layout of the 90 nm ADC. ....	56
Figure 5.6. Functional simulation of the 6-bit ADC operating at 1 GS/s. ....	57
Figure 5.7. INL plot of the ADC. ....	59
Figure 5.8. DNL plot of the ADC. ....	59
Figure 5.9. FFT plot of the ADC at a sinusoidal input frequency $f_{in}$ of 1 MHz for SNDR calculation. ....	60
Figure 5.10. Instantaneous power plot of ADC with a load capacitance of 100 fF. ....	62
Figure 5.11. Functional simulation of the ADC at 45 nm mode. ....	64

Figure 5.12. INL plot of the ADC at 45 nm node. ....	65
Figure 5.13. DNL plot of the ADC at 45 nm node. ....	66
Figure 5.14. SNDR plot of ADC at 45 nm node. ....	66
Figure 5.15. Instantaneous power plot of the ADC at 45 nm node. ....	67
Figure 5.16. Nominal-case logical design of the VCO. ....	69
Figure 5.17. High level representation of the ULC. ....	71
Figure 5.18. Schematic logical block diagram of the baseline (unoptimized) ULC. ....	72
Figure 5.19. Circuit used for pass/block ....	73
Figure 5.20. Functional simulation result of up-converter circuit. ....	74
Figure 5.21. Down-converter circuit. ....	75
Figure 5.22. Functional simulation of down-converter circuit. ....	75
Figure 5.23. Transistor-level realization of the baseline design of the ULC with 32 transistors. ....	76
Figure 5.24. Functional simulation for pass/block circuit at $V_{ddl} = 1.02$ V, $V_{ddh} = 1.2$ V and load = 45 fF. .....	77
Figure 5.25. Transistor-level realization of the baseline design of the ULC with 32 transistors. ....	78
Figure 5.26. Transistor-level circuit realization of the area optimal ULC. ....	79
Figure 5.27. Functional simulation of the area optimal ULC. ....	79
Figure 5.28. Circuit diagram of an APS. ....	81
Figure 5.29. An $8 \times 8$ APS array constructed by using a collection of APS. ....	82
Figure 5.30. Circuit diagram of an APS. ....	83
Figure 5.31. Circuit simulation of the $8 \times 8$ APS array. ....	83
Figure 6.1. Corner methodology used for the process variation study. ....	87

Figure 6.2. Comparison of frequency-voltage characteristics of the logical design and parasitic extracted physical design of the VCO. ....	90
Figure 6.3. Final layout of the VCO optimized for parasitic-aware design flow. ....	92
Figure 6.4. Frequency-voltage transfer characteristics of the VCO optimized for design flow accounting for parasitics. ....	92
Figure 6.5. Statistical $V_{dd}$ variation. ....	94
Figure 6.6. Statistical $V_{Tnmos}$ variation. ....	94
Figure 6.7. Statistical $V_{Tpmos}$ variation. ....	95
Figure 6.8. Statistical simultaneous $T_{oxnmos} + T_{oxpmos}$ variation. ....	95
Figure 6.9. $V_{dd} + V_{Tnmos} + V_{Tpmos} + T_{oxnmos} + T_{oxpmos}$ variation. ....	96
Figure 6.10. Comparison of frequency-voltage characteristics of the logical design, parasitic extracted physical design, and parasitic extracted physical design subjected to worst-case process variation. ....	98
Figure 6.11. Final VCO layout optimized for parasitic- and process-variation-aware design flow.....	100
Figure 6.12. Frequency-voltage transfer characteristics of the VCO optimized for design flow accounting for parasitics and process variation. ....	101
Figure 6.13. Parametric analysis with input voltage sweep. ....	107
Figure 6.14. Performance of the ULC under varying output capacitive load. ....	108

Figure 6.15. Instantaneous power plot of the ULC at a load capacitance of 45 fF. Average power consumed = 19.89 $\mu$ W.....	109
Figure 6.16. Proposed design flow for optimal design of nano-CMOS APS array. ....	110
Figure 6.17. Distribution of (a) average power $P_{APS}$ and (b) output voltage swing $V_{swing}$ for the case $V_{dd} = V_{dd-H}$ and $T_{xo} = T_{ox-L}$ . .....	112
Figure 6.18. Distribution of (a) average power $P_{APS}$ and (b) output voltage swing $V_{swing}$ for the case $V_{dd} = V_{dd-L}$ and $T_{xo} = T_{ox-L}$ . ....	114
Figure 6.19. Distribution of (a) average power $P_{APS}$ and (b) output voltage swing $V_{swing}$ for the case $V_{dd} = V_{dd-L}$ and $T_{xo} = T_{ox-H}$ . ....	114
Figure 6.20. Distribution of (a) average power $P_{APS}$ and (b) output voltage swing $V_{swing}$ for the case $V_{dd} = V_{dd-H}$ and $T_{xo} = T_{ox-H}$ . .....	115
Figure 6.21. Pareto plots for (a) $fP_{APS}$ and (b) $fV_{swing}$ . .....	117
Figure 6.22. Flowchart of the proposed algorithm. ....	118

## CHAPTER 1

### INTRODUCTION AND MOTIVATION

The demand for low-power consuming circuits is increasing with the requirements for personal computing devices and wireless communications equipment. Several factors, such as battery life, heat dissipation, packaging costs, environmental concerns, and reliability issues are driving this demand [83]. Mechanisms such as voltage reduction, frequency scaling, and clock gating are helpful in reducing power consumption of the target systems for different applications [85]. Power management is fast becoming one of the most critical design constraints in the world of integrated circuit (IC) designers. New 90 nanometer (nm) processes deliver greater silicon (Si) performance and integration, but battery technology has not kept up. To compensate, new design techniques are being developed to address the need for low-power silicon. Dynamic power management techniques using variable supply voltage (variable  $V_{dd}$ ) are popular for system-level power reduction, and multiple supply voltage (MSV) is a static solution for switching power reduction in application specific ICs (ASICs) [18].

The major components of total power dissipation in any circuit can be identified as  $P_{switching}$ , the switching power dissipation;  $P_{short-circuit}$ , the short-circuit power dissipation; and  $P_{leakage}$ , the leakage power from various sources. Each one of these power dissipation sources is dependent on supply voltage, some linearly and some quadratically. For example, switching power has a quadratic relationship with the power supply voltage  $V_{dd}$ . Hence, a significant amount of power can be saved by simply reducing the supply voltage  $V_{dd}$ . However, the power reduction puts a strain on the performance targets. Since lowering the supply voltage slows down the speed at which transistors can switch, one must be selective in determining which parts of the design should have the voltage reduced (known as voltage scaling). Voltage scaling requires

partitioning of the design into voltage islands or voltage domains. Each domain operates at a different supply voltage depending on its timing characteristics [86]. The blocks that are time-critical in one domain operate at the standard supply voltage. The less time-critical blocks are aggregated into a second domain, with the voltage scaled down. A challenge with voltage scaling is the need to translate the voltages for the signals that interface between voltage domains. This translation is accomplished by inserting level shifters, which are special cells that perform voltage translation [57], and clamp cells to provide isolation. Basically, there are two types of voltage converters: level-up and level-down. A level-up converter is used as an interface in which low  $V_{dd}$  cells ( $V_{ddl}$ ) drive high  $V_{dd}$  cells ( $V_{ddh}$ ) in order to reduce the short-circuit power dissipation [129]. One application is the dual- $V_{dd}$  field programmable gate array (FPGA) fabric [78]. Level-down converter is required for switching power reduction, where the non-critical blocks of the circuit are made to operate at a lower-power supply voltage [57]. In the standby mode of a circuit, no active switching occurs, and all power dissipation is due to standby leakage. A simple power-saving scheme could be to shut off unused blocks in the standby mode.

Portable electronic components such as cell phones, which are realized as systems on a chip (SoCs) and supplied with power from a single battery source require level converters. Such electronic devices often contain several sub-circuits, with each sub-circuit requiring a unique voltage level different from that supplied by the battery (sometimes higher or lower than the battery voltage). Level converters offer a method of generating multiple controlled voltages from a single, rather than multiple batteries, thereby saving space and cost to supply different parts of the device. They can also be effectively applicable for large-scale integration (LSI) high-speed input-output circuits, as an interface between internal and external buses as a server or



exchanger. They can also be used as an interface circuit between optical devices for optical communications [129] or as interfaces between different logic families.

### 1.1. Issues Faced by Digital, Analog, and Mixed-Signal Circuits

The main issues faced by digital, analog, and mixed-signal circuits of today are as follows:

#### 1.1.1. Technology Scaling

A large number of SoCs are manufactured nowadays in the 90 nm process node, and the ramp up for 65 nm design has become more aggressive than expected. The 45 nm process design is following close behind, with early versions of design rules and process parameters already available [5, 4]. Intellectual property (IP) core providers are faced with the challenge of meeting analog performance in a technology that has been targeted for digital logic. New circuit design techniques that accommodate lower supply voltages necessary for portable systems also need to be integrated into the IP core. Systems that once worked at 3.3 volts (V) or 2.5 V now need to work at 1.8 V or lower without causing any performance degradation. The need for greater processing speed has designers craving smaller device geometries. Smaller devices provide higher packing density and lower overall power consumption, due to lower parasitics and lower supply voltages. This shortening of the minimum channel length has resulted in the reduction of power supply voltage to the 1 V - 0.7 V range. The SoC trend also forces analog circuits to be integrated with digital circuits. To keep up with the scaling of the minimum channel length and SoC trend, analog circuits need to be operated at low voltages, especially in portable devices. However, the minimum supply voltage for analog circuits predicted in the semiconductor road map [5] does not follow the reduction of digital supply voltage. Analog supply voltages between 1.8 V and 2.5 V are still being used with channel lengths of 0.18 micrometer ( $\mu\text{m}$ ) and 0.13  $\mu\text{m}$

[30]. Hence, it is a great challenge to design low supply voltage operating analog/mixed-signal circuits while considering the relatively high threshold voltage of short channel length transistors.

Another important consideration for an SoC is that the analog/mixed-signal circuits should be designed by using a standard complementary metal oxide semiconductor (CMOS) digital process without having process options such as deep n-well or on-chip inductors or varactors.

Analog circuit designs often contain matched transistors [98]. The threshold voltage of a metal oxide semiconductor (MOS) transistor is defined as the gate voltage required to induce a channel for current flow through the transistor [99]. Matched CMOS transistors are designed to be necessarily identical. During fabrication, the threshold voltage of an MOS transistor is engineered to a desired voltage using processing. In a typical MOS field effect transistor (FET) process, ion-implanted charges are used to shift the threshold voltage. This processing step, called the threshold voltage adjustment implant, is random, consisting of varying energy levels of the implanted ions and subsequent temperature ramp step to diffuse the ions. The random nature of this process results in the random fluctuations in threshold voltage as a function of transistor area. Additionally, random variations in the lithography result in small geometric inaccuracies. The variation of the effective threshold voltage ( $V_T$ ) increases as the transistor areas decrease. In CMOS analog circuits, it is the variation of the threshold voltages between two transistors rather than their absolute voltage values that is of interest for the majority of applications. Hence, it is essential to analyze the effect of threshold voltage mismatch on the analog circuit performance. Because the threshold voltage, mobility, and channel length of a device are sensitive to temperature variations [10], a temperature sensitivity analysis also needs

to be carried out. In addition, the power supply voltage variations in the analog design have been accounted for, to verify its system-on-chip capability.

### 1.1.2. Power Performance

A dichotomy exists in the design of ICs: They must be simultaneously low power and high performance. Minimum power expenditure is joined at the hip to performance today. The goal of power-aware design is to minimize power consumption while meeting performance requirements. Therefore, as power dissipation increases, the cost of power delivery to the ever-increasing number of transistors on a chip multiplies rapidly. Power conservation impacts every budget, whether technological or financial. Product acceptability, reliability, and profitability depend as much on power efficiency as they do on performance. There is a difference between low-power design and power-aware design [97]. Low-power design refers to minimizing power with or without a performance constraint. Power-aware design refers to maximizing some other performance metric, subject to a power budget.

### 1.1.3. Process Variation

The fluctuation of device characteristics caused by process variation has considerably increased in nanometer technologies. Process variations can be classified into inter- and intra-die [92]. Inter-die variation, which comes from lot-to-lot, wafer-to-wafer, and within wafer, affects every device on a single chip equally. On the other hand, intra-die variation refers to device characteristics such as device geometry change, dopant density change, threshold voltage, gate oxide thickness, and circuit timing change, which vary from device to device within the same die. Some of the variations are random and some are systematic.

Capturing and modeling the intra-die process variation becomes essential to device and interconnect extraction tools for accurate timing and power analysis. The standard design cycle

must include process variation in order to produce variation-tolerant physical designs. Just as in digital design where interconnect delays make or break a design, the move to 90 nm and lower process technologies means that the variations in process parameters have a resounding effect on the performance metrics of analog/mixed-signal, memory and radio-frequency (RF) circuits. Unlike a digital circuit, which is typically optimized only for speed and power, an analog circuit is designed to meet as many as 5 to 10 performance metrics. As a result, the impact of these process variations is seen as design yield loss, which in turn directly bites the bottom line of a company's profits. This loss calls for a proactive and a deterministic way to deal with performance and yield while in the design phase and not after the first silicon.

#### 1.1.4. Parasitics

Parasitic-aware optimization methodologies require that the parasitics be considered at the beginning of the design [96]. Where IC components are designed assuming ideal components, it is observed that parasitics have serious degrading effects at high frequencies. The only way to overcome these effects is to consider parasitics as an integral part of the circuit. Thus, parasitic-aware design and optimization are essential. If parasitics have an acute effect on the design, an early layout needs to be created so that the parasitics can be extracted and their effect estimated. Without that early layout-parasitic information, designers rely mostly on experience. If a design is understood well enough to know the sensitive nodes, dummy elements can be placed on those nodes to mimic the effect of real parasitics. This process is tedious and error-prone. Therefore, a methodology is required which can achieve the required performance while accounting for the parasitics. Hence, there is a need for a design methodology accounting for parasitics and process variation of general IC components.

#### 1.1.5. Temperature Variation

Another emerging critical issue due to technology scaling is the effect of on-die temperature variation [21]. What was previously a second-order effect that could be adequately addressed with a few corner cases and guardbands has now become a first-order effect. Temperature interacts with a number of these other issues in ways that make analysis difficult. There's a need for new, temperature-aware design methodologies in order to produce properly functioning and reliable first silicon. Both power dissipation and operating frequency worsen at high temperatures because of the increase of leakage currents and the reduction of carrier mobility. The challenge for RF design is centering of a design including process, voltage and temperature (PVT) variations. By integrating temperature-aware capabilities into today's design flows, there is no need to rewrite the golden analysis standards that have been established for the past decade. Instead, through the use of tools that incrementally retrofit today's flows with temperature-aware data, the temperature effects can be fully accounted for. Applying thermal analysis reduces pessimism or risk associated with the assumption of a uniform on-chip temperature. A temperature-aware design flow is useful for existing technologies down to 90 nm, and is required for technologies below 90 nm.

In summary, the demand for emerging application-specific, nanoscale mixed-signal SoCs which need process (threshold voltage mismatch) variation-tolerant low-power high-performance parasitic-aware mixed-signal circuitry and development of mature nano-CMOS processing technology has motivated this research.

## 1.2. Organization of This Dissertation

This dissertation is organized as follows: Chapter 2 discusses the theory behind current state-of-art emerging technologies, the power leakage and delay models used in this dissertation, and the low-power design techniques implemented. Chapter 3 summarizes the various works

related to low-power design, parasitic-aware and process-variation characterization techniques, and mixed-signal circuits implemented in this dissertation. Chapter 4 discusses the issue of low-power design in the presence of process variations and parasitics and presents the optimization methodologies used to achieve low-power, parasitic-aware and process-variation tolerant circuits. Chapter 5 presents the logical and physical design of mixed-signal circuits used as case studies in this dissertation, and their nominal characterization. Chapter 6 describes the application of the optimization methodologies discussed in chapter 4 to the circuits presented in chapter 5, thus demonstrating the effectiveness of these approaches. Finally, chapter 7 summarizes the results and concludes the dissertation with a mention of the future directions of research.

## CHAPTER 2

### THEORETICAL BACKGROUND

This chapter presents the theoretical background related to the work presented in this dissertation. Section 2.1 discusses the current emerging technologies, considering the ongoing trends of the market. This discussion includes nanoscale complementary metal oxide semiconductor (nano-CMOS) transistors, high- $\kappa$  metal gate transistors, fin field effect transistors (FET) (dual-gate FETs) and carbon nanotube transistors (CNT). Section 2.2 discusses the power leakage and delay models used for measurement. Finally, section 2.3 gives an overview of the existing low-power design techniques used in the market today and implemented in the work described in this dissertation.

#### 2.1. Emerging Technologies

Since their first demonstration in 1960 [5], planar silicon metal oxide semi-conductor field effect transistors (Si MOSFETs) have experienced a steady exponential downsizing of their critical dimensions. Over a period of 45 years, the printed gate lengths of the MOSFETs have been scaled down from 100  $\mu\text{m}$  to 35 nm; the latter refers to the gate lengths for the 65 nm technology node devices in commercial microprocessors that are currently available. Because of a steady improvement of their performances through scaling, MOSFETs have become the leading integrated circuit (IC) technology for high-performance and low-power logic applications. Over this long period of development, the technology has faced numerous challenges, which were always solved by vigorous research, ingenious design, and brilliant engineering. The exponential scaling down of the feature sizes, and hence the exponential increase of the transistor count in an IC was first observed by Gordon Moore in 1965 [88]. His observation, which later became known as Moore's law, states that the number of transistors per

IC doubles every 24 months. Moore's law has been serving as the guiding principle for the semiconductor industry for over 30 years.

According to projections by the International Technology Roadmap for Semiconductors (ITRS), by the middle of next decade, the printed gate length of the MOSFETs will be less than 10 nm [38]. Since no exponential can continue forever, sustaining Moore's law is becoming challenging for the planar bulk CMOS technology, for which the key technical issue for scaling devices below the 32 nm node is the high off-state leakage current [103]. The origin of this scaling limit for the single-gate, bulk CMOS technology can be traced back to the inherent poor electrostatic design of the planar device geometry and the poor transport properties of carriers in the Si channels. Consequently, an intense research effort, directed toward exploring new device designs and new channel materials for future logic technologies, has recently been undertaken.

Dual-gate devices and carbon nanotube transistors [110] show promise for scaling beyond the planar bulk MOSFET limit. The electrostatic integrity of the nanoscale CMOS devices improves considerably when additional gates are included, such as for dual-gate or finFET devices. Because these non-planar devices are inherently resistant to short-channel-effects, it is widely believed that one of them will form the basic device architecture for future generations of CMOS devices. In order to sustain Moore's law for over four decades, nearly all materials and design aspects of the original MOSFET have been lost, except the use of Si-silicon dioxide ( $\text{SiO}_2$ ) material system as channel material and gate insulator. Aggressive scaling of gate oxide has reduced its thickness to a present-day value of about 1 nm, and any further thinning is prohibitive because of oxide reliability issues and the exponential increase of leakage current from direct tunneling. Sustaining Moore's law, however, depends crucially on the gate insulator scaling; consequently, replacing  $\text{SiO}_2$  with high- $\kappa$  dielectric-metal gate stack is within sight [39].



Among all semiconductors, although Si has the poorest transport properties (mobilities and diffusion coefficients for electron and holes), its success as channel material is due to the excellent interface property of the Si-SiO<sub>2</sub> system. SiO<sub>2</sub> will almost certainly be replaced by high- $\kappa$  gate dielectric in the near future. Research activity in this area has experienced a boom in recent years with many new devices and material systems now proposed. The following sections briefly describe the devices explored in this dissertation.

#### 2.1.1. Nanoscale CMOS (Nano-CMOS)

It has been overwhelmingly felt that mixed-signal electronics has been the driving force behind modern technological advances in the society. It has penetrated every walk of life and has been embedded into all our activities. Whether it is the built-in feature of an alarm clock in mobile phones that people wake up to in the morning or the sensor embedded into the microwave oven that heats a breakfast; the sleek, handheld personal digital assistant device or the laptop that keeps a busy executive on the move; or the latest MP3 player that accompany many joggers, everything has that “digital” tinge in it. In short, every accessory or gadget that used in daily life is becoming smaller, cheaper, more efficient, and more feature-packed; this is what “digital” equipment has come to mean to a general user. Demands for more and more features in every device have thus skyrocketed. Consequently, in recent years, there has been a phenomenal increase in the demand for low-power and high-performance digital devices. This market of digital electronics is driven by the prowess of an immensely versatile, efficient, and economical device called the CMOS. CMOS forms the backbone of today's circuits deploying very large scale integration (VLSI).

The transistor-feature sizes have shrunk dramatically with the technology scaling. With the accompanying shrinking of feature size, a paradigm shift in the power profiles of the devices

has occurred. The leakage components of the fundamental CMOS device have changed exponentially, and each component of the total leakage has gained in relative importance. Thus, a drastic change has occurred in the leakage components of the device, both in the inactive as well as the active modes of operation. As the dimensions of the CMOS device reach nanometer ranges, dynamic power consumption remains almost unchanged; but leakage power dissipation increases significantly and becomes a large portion of the total power dissipation as the technology changes. This change has necessitated a critical analysis of the leakage components in the nanoscale CMOS VLSI devices and a concomitant need for the exploration of efficient reduction techniques of these leakage components, which continues to be dissipated even when a device is not doing any useful operation.

Scaling of CMOS implies proportional reduction of the geometrical features as well as the parametric features (device characteristics) of the CMOS transistor. The idea of scaling began with the classical Moore's law, which had a phenomenal impact as a driving force for the entire semiconductor industry. CMOS scaling has become a very well-defined practice in the semiconductor industry. The design goals for scaling have been well defined for a long time. The main three typical goals of classical technology scaling are to

- Reduce gate delay by about 30%, which results in an increase in an operating frequency of about 43%
- Double the transistor density, which results in packing ever more components in the same chip (following Moore's law)
- Reduce energy per transition by about 65% and thus save 50% of power (at a 43% increase in frequency)

Most of the goals have been maintained over all the years to a great benefit and have fueled market demand for portable devices. The scaling of CMOS has always beaten predictions and has advanced faster than predicted. The benefits of scaling have been manifold:

- Decreasing device size
- Increasing chip density and component density
- Increasing performance and speed
- Decreasing cost
- Decreasing supply voltage
- Decreasing power requirement

However, there are some obvious roadblocks that can be credited to scaling:

- Tremendous increase in power density in a chip
- Issues in reliability and robustness
- Ever-increasing mask costs and fabrication issues
- Tremendous increase in complexity
- Decreasing design flexibility
- Random dopant fluctuations
- Increasing process variations at nano levels
- Increased likelihood of soft errors

The channel length of a device represents the technology node that a particular process follows. The current industrial processes now are inching down to reach the nanometer level, where the channel length is of the order of a fraction of a micron. Industry has already put 45 nm node process into production. However, at these nanoscale levels, the channel is much shorter than the conventional channel length, and the device characteristics are very much affected by

these shorter channel lengths. A number of adverse effects peculiar to scaling which result in a significantly reduced channel length are identified as short channel effects (SCEs). These SCEs mostly pertain to the power dissipation or leakage characteristics of the nanoscaled CMOS device. There are several forms of leakage currents (figure 2.1) in a short-channel nanometer transistor [103]:

- $I_1$ : Drain to source active current (ON state)
- $I_2$ : Drain to source short-circuit current (ON state)
- $I_3$ : Subthreshold leakage (OFF state)
- $I_4$ : Gate oxide tunneling leakage (ON and OFF states)
- $I_5$ : Gate current due to hot carrier injection (ON and OFF states)
- $I_6$ : Channel punch through current (OFF state)
- $I_7$ : Gate-induced drain leakage (GIDL) (OFF state)
- $I_8$ : Reverse biased p-n junction leakage (ON and OFF states)

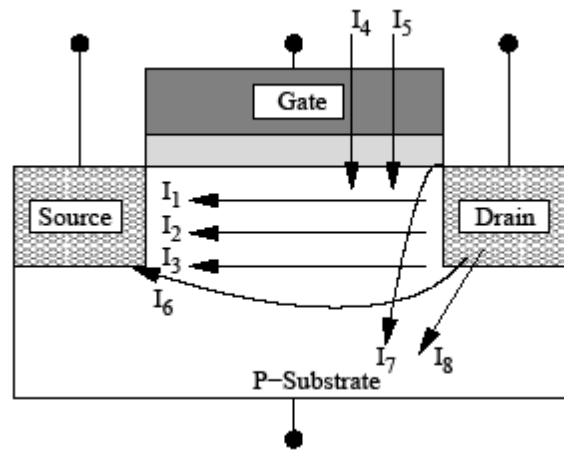


Figure 2.1. Various leakage currents in a nanoscale CMOS transistor.

Each power component has several forms and origins as they flow between different terminals and in different operating conditions of a transistor, as shown in figure 2.1. These

SCEs, among others, are gaining prominence with the phenomenon of scaling. To overcome these SCEs, the ITRS roadmap envisions that high-performance CMOS circuits will require ultra-low gate oxide thickness [5]. However, such devices will be susceptible to a more profound leakage mechanism because of tunneling through the gate oxide ( $I_{gate}$ ) [29]. Thus, there is a critical need for analysis, explanation, and characterization of the various tunneling mechanisms, targeted toward design for manufacturing (DFM) and process variation modeling.

#### 2.1.2. High- $\kappa$ /Metal Gate

Aggressive scaling of  $\text{SiO}_2$  has been going on for the past 15 years for low-power, high-performance CMOS transistor applications [38]. Recently,  $\text{SiO}_2$  with a physical thickness of 1.2 nm was implemented in the 90 nm logic technology node. In addition, research transistors with 0.8 nm (physical thickness)  $\text{SiO}_2$  have been demonstrated in the laboratory. However, continual gate oxide scaling will require high- $\kappa$  gate dielectric ( $\kappa$  being the dielectric constant) since the gate oxide leakage in  $\text{SiO}_2$  is increasing with reducing physical thickness and  $\text{SiO}_2$  will eventually run out of atoms for further scaling. The majority of the high- $\kappa$  gate dielectrics investigated are based on hafnium oxide ( $\text{HfO}_2$ ) and zirconium oxide ( $\text{ZrO}_2$ ) [39]. Metals are being evaluated as the gate electrodes for the high- $\kappa$  gate dielectrics. The use of high- $\kappa$  serves the dual purpose of scaling the device as well as reducing gate leakage. Hence, high- $\kappa$  metal gate transistors serve as a good alternative to classical CMOS transistors in nanoscale technologies. The structure of a high- $\kappa$  metal gate transistor is shown in figure 2.2.

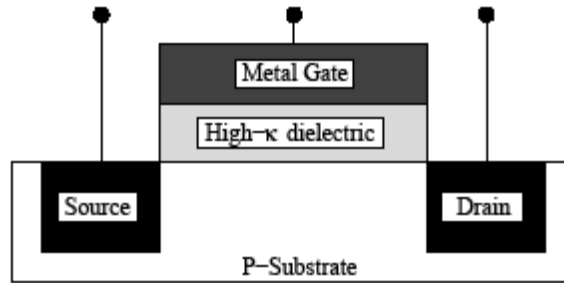


Figure 2.2. Structure of high- $\kappa$  metal gate transistor.

### 2.1.3. Fin FET/Dual-Gate FET

General MOSFET at a submicron level is suffering from several submicron issues like SCEs and threshold voltage variation. Fin FET is proposed to overcome the SCEs. The silicon-on-insulator (SOI) process is used to fabricate fin FET. This process ensures the ultrathin specifications of the device regions. In fin FET, electrical potential throughout the channel is controlled by the gate voltage. This control is possible because of the proximity of the gate control electrode to the current conduction path between the source and the drain. These characteristics of the fin FET minimize the SCE [105]. Advantages of the fin FET over its bulk-Si counterpart are as follows:

- Conventional MOSET manufacturing processes can also be used to fabricate fin FET
- Fin FET provides better area efficiency than MOSFET
- Mobility of the carriers can be improved by using the fin FET process in conjunction with the strained Si process

The silicon on insulator (SOI) process is used to manufacture fin FET. A single polysilicon layer is deposited over a fin. Thus polysilicon straddles the fin structure to form perfectly aligned gates. Here fin itself acts as a channel and it terminates on both sides of source and drain. In general MOSFET device, over the Si substrate poly-Si gate is formed. Poly-Si gate

controls the channel. Straddling of poly-Si gate over the Si fin gives efficient gate-controlled characteristics compared to MOSFET. Since gate straddles the fin the length of the channel is same as that of width of the fin. As there are two gates effectively around the fin, the width of the channel is equivalent to twice the height of the fin; i.e.,  $W = 2 \times h$ . A term called “fin pitch” is used to define the space between two fins. The height of the fin FET is equivalent to the width of the MOSFET. If  $W$  is the fin pitch, then to attain the same area efficiency required, fin height is  $W/2$ . But practical experiments have shown that fin height can be greater than  $W/2$  for a fin pitch of  $W$ ; thus, fin FET achieves more area efficiency than MOSFET.

SOI technology is used for the fabrication of fin FET. In SOI technology, an insulator,  $\text{SiO}_2$ , isolates the bulk from the substrate. An extremely shallow junction is formed because of the depth limitation put by the insulator. The dielectric isolation and elimination of the latch-up problem are the advantages of the SOI process. In the Fin FET fabrication process, silicon nitride ( $\text{Si}_3\text{N}_4$ ) and  $\text{SiO}_2$  are deposited on a thin SOI layer. Electron beam lithography is used to form a Si fin. Channel length and channel width are determined by the accuracy of the fin. Poly-Si with pentavalent impurities and the oxide layer are deposited over the Si fin. The source and drain regions are separated and insulator spacers are formed. Then the etching process is carried out on a spacer until a Si fin is reached. Gate is formed by depositing the gate layer. Silicidation is performed to decrease the high-source drain resistance which is formed because of very thin layers of source and drain. The structure of fin FET is shown in figure 2.3.

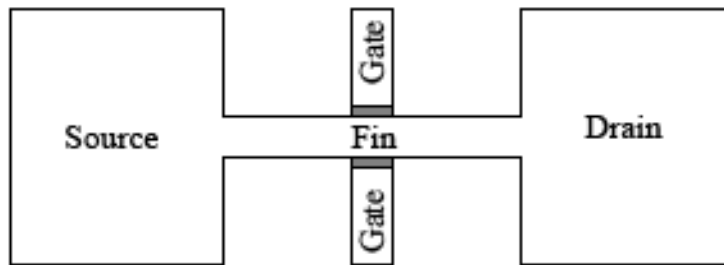


Figure 2.3. Structure of the fin FET transistor.

#### 2.1.4. Carbon Nanotube (CNT)

Research within the computing industry continues to focus on downscaling the existing CMOS architectures. However, several problems arise when CMOS transistor feature sizes drop below 45 nm; these problems prevent manufacturers from fabricating improved VLSI designs using these nanoscale transistors. On the other hand, CNT devices show either only a fraction of these unwanted characteristics or exhibit no degree at all [11]. CNTs can be fabricated in either metallic or semiconducting configurations in which the current transport is ballistic, leading to carrier mobilities that are much higher than in Si. In addition, the absence of collision scattering in the one-dimensional crystalline structure of the CNTs results in current densities well in excess that of metals. Given their wire-like structure, CNTs can be used to fabricate transistors and interconnects, the two fundamental components of modern microelectronics technology.

Among the preventative phenomena exhibited by nanoscale MOSFETs are the following:

- *High electric fields*

As feature sizes shrink to the nanometer level, MOSFETs require a nonlinear decrease in the power supply voltage as a function of channel length. The result is an increase in the magnitude of electric field across the gate oxide layer, which produces higher leakage



currents at the gate. This leakage current degrades performance and may drive the device into avalanche breakdown during which freely conducted electrons produce damaging current levels. The nanotube, however, acts as a quasi-one-dimensional path and possesses no called bulk. Therefore, power supply voltage can be reduced linearly as a function of channel (or tube) length.

- *Threshold voltage*

Although desirable, reduction of the threshold voltage proportional to the downscale of the MOSFET channel is not possible because it is necessary to control the quiescent state power consumption. This power consumption is due primarily to leakage current through the device, which is mitigated by maintaining a high threshold voltage. The large  $V_T$ , however, reduces the margins between saturation and cutoff states, and therefore the probability the device may enter a linear mode of operation.

- *Interconnect delays*

Any decrease in wire width leads to an increase in interconnect resistance, thereby increasing propagation delay. It turns out that the increase in interconnect delays is large compared to the corresponding increase in gate delay. Thus, continued downscaling will yield diminishing returns in speed, which may eventually curtail altogether.

- *Gate-oxide layer shrinking*

At 0.1  $\mu\text{m}$ , CMOS devices require an oxide thickness of at least 3 nm. Such a thin oxide layer allows quantum tunneling and hence leakage current through the gate. Decreases in the gate oxide layer exacerbate this leakage and render further downscaling impractical. Thus, inefficient doping and the onset of quantum mechanical effects hinder CMOS device operation when fabricated at nanometer scales. The hardware industry is attempting to work around these

obstacles by engineering devices that compensate for quantum effects. CNTs eliminate these concerns and provide a means of meeting future demands for smaller, faster microelectronic devices. What remains is to master the CNT FET fabrication techniques and the work required to bring these techniques to production level.

Thus, we see that CNT is a potential successor for CMOS in nanoscale technologies. The research described in this dissertation aimed to explore the design scenario when future, CNT will be used to design the circuits at nanometer levels. Figure 2.4 shows the structure of a CNT transistor.

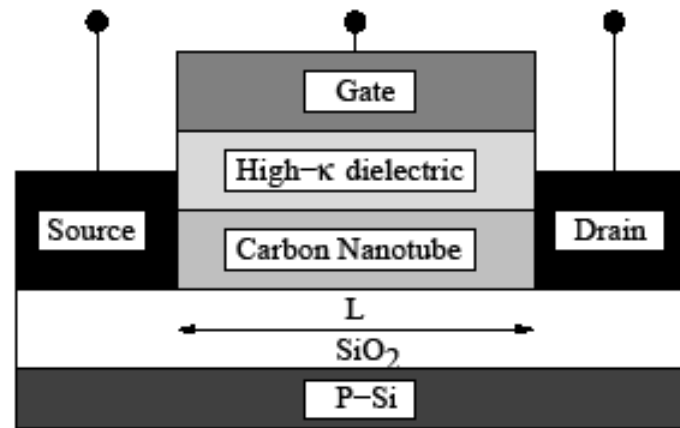


Figure 2.4. Structure of a CNT transistor.

## 2.2. Power Leakage and Delay Models

While the aggressive scaling of CMOS technology to ever smaller dimensions has enabled higher performance and integration levels, it has given rise to a plethora of new problems in the design of ICs. The reason for this rise is that the supply voltage has continually scaled down to reduce the dynamic power consumption. As the supply voltage is scaled down, the threshold voltage has to be reduced in the same proportion to maintain performance. Reduced threshold voltages and gate oxide thicknesses have caused an alarming increase in subthreshold

source-drain leakage and gate leakage power dissipation in both active and standby modes of operation. As a result, leakage power has become an increasingly important fraction of the total chip power in the current technology generation. In the past, the subthreshold leakage of transistors has been very small; but as transistors have been scaled down below the 100 nm node, leakage composes nearly 50% of the total power consumption. As threshold voltages are reduced, subthreshold leakage rises exponentially. Also at nanoscale technologies, gate-oxide leakage is comparable to subthreshold leakage. The subthreshold leakage problem has been widely researched in recent years, and several promising circuit techniques have been proposed for addressing it [43]. However, in future technology generations, gate leakage is expected to grow faster than subthreshold leakage since gate oxide thicknesses are being scaled at a much faster rate than supply or threshold voltages [5].

Furthermore, gate leakage is a problem when the transistor is in both the on and the off states, whereas subthreshold leakage dissipates power only when the transistor is off. In general, the requirements for minimizing subthreshold leakage are contradictory to those for reducing gate leakage because of their inherently different mechanisms. This contradiction makes the problem of total leakage reduction challenging and intriguing as it is necessary to suitably mitigate both of these leakage components based on their relative contributions. In the future, it is certain that most of the burden of dealing with total leakage reduction will fall to circuit techniques.

The following subsections explain the power models that are referred for the power-delay optimization of circuits used in this dissertation. Design techniques for the reduction of leakage power should not affect design performance. Hence, I also considered a delay model.

#### 2.2.1. Dynamic Power

The dynamic power consumption of a circuit is given as [99]:

$$(1) \quad P_{dynamic} = \alpha \times C_L \times V_{dd}^2 \times f$$

where the  $\alpha$  term is an activity factor that captures how many devices are active on any particular clock cycle,  $C_L$  is the total switched capacitive load,  $V_{dd}$  is the supply voltage, and  $f$  is the frequency of the clock.  $P_{dynamic}$  term is derived from the equations for energy consumed in charging and discharging a capacitor. This power dissipation depends on loading condition not the device features.

### 2.2.2. Subthreshold Leakage

The subthreshold leakage current ( $I_{sub}$ ) through a MOSFET can be modeled as follows [1, 72]:

$$(2) \quad I_{sub} = I_0 \times \left[ 1 - \exp\left(\frac{-V_{ds}}{v_{therm}}\right) \right] \times \exp\left(\frac{V_{gs} - V_T - V_{off}}{S \times v_{therm}}\right)$$

where  $I_0$  is a constant dependent upon device parameters for a given technology,  $v_{therm}$  is the thermal voltage,  $V_T$  is the threshold voltage,  $V_{off}$  is the offset voltage which determines the channel current at  $V_{gs} = 0$ ,  $S$  is the subthreshold swing factor,  $V_{gs}$  is gate-to-source voltage, and  $V_{ds}$  is the drain-to-source voltage. Hence, if  $T_{ox}$  is increased, the length ( $L_{eff}$ ) is increased and/or the width ( $W_{eff}$ ) of the transistors is reduced, there will be a reduction in the subthreshold current.

### 2.2.3. Gate-Oxide Leakage

Gate-oxide leakage in a MOSFET due to direct tunneling can be modeled as follows [42, 109]:

$$(3) \quad J_{DT} = A \times \left( \frac{V_{ox}}{T_{ox}} \right)^2 \times \exp \left[ \frac{-B \left[ 1 - \left[ 1 - \frac{V_{ox}}{\phi_{ox}} \right]^{\frac{3}{2}} \right]}{\frac{V_{ox}}{T_{ox}}} \right]$$

where  $J_{DT}$  is the direct tunneling current density,  $V_{ox}$  is the potential drop across the thin oxide, and  $\phi_{ox}$  is the barrier height for the tunneling particle (hole or electron).  $A$  and  $B$  are physical parameters. From this expression, one can see that gate leakage is exponentially dependent on variations in  $T_{ox}$ . Hence, if  $T_{ox}$  is increased, there will be a reduction in the gate oxide leakage current.

#### 2.2.4. Total Power Dissipation

The total power of a circuit ( $P_{circuit}$ ) can then be calculated as

$$(4) \quad P_{circuit} = P_{dynamic} + P_{subthreshold} + P_{gate-oxide}$$

where  $P_{dynamic}$ ,  $P_{subthreshold}$  and  $P_{gate-oxide}$  can be calculated from equations 1, 2 and 3, respectively.

Thus, we conclude that  $T_{ox}$ ,  $V_T$ , and the geometry of a transistor play a crucial role in determining the power dissipation of a circuit.

#### 2.2.5. Delay Model

The delay of a device is approximately given as [109]:

$$(5) \quad Delay = k \times \left[ \frac{C_L \times V_{dd}}{\mu \times \left( \frac{\epsilon_{ox}}{T_{ox}} \right) \times \left( \frac{W_{eff}}{L_{eff}} \right) \times (V_{dd} - V_T) \alpha} \right]$$

where  $k$  = technology constant,  $\mu$  is the electron surface mobility and  $\alpha$  is the velocity saturation index, which varies from 1.4 to 2 for nanometer CMOS. The delay of circuits is generally calculated from the 50% level of the input swing to 50% level of the output swing.

### 2.3. Low-Power Design Techniques

As seen in the section 2.1, power dissipation has become the most significant issue for consumers as well as designers for the nanoscale CMOS regime. As the demand for more and more portable battery-operated devices increases, the issue of low-power VLSI design becomes more critical. The reasons that why power becomes an issue can be summarized as follows:

- With scaling, new and ever-more obtrusive forms of power leakage become prevalent
- Static power consumption becomes as significant as dynamic power, implying that the device is dissipating half the power without doing any useful work
- High-power dissipation increases the packaging and cooling costs, which are not economical even at higher technology nodes
- Battery technology, like many other technologies, is not expected to keep pace with the scaling
- Wasting precious power resources affects the environment
- Scaling has resulted in manifold complexity in today's CMOS circuits; this issue, along with diverse and profound power leakage makes reliability and robustness of the device a prime concern.

The various low-power techniques can be classified into two categories:

#### (1) *Structural Techniques*

- Voltage islands
- Multi-threshold ( $V_T$ ) devices
- Minimized capacitance by custom design
- Power-efficient circuits
- Parallelism in micro-architecture

## *(2) Traditional Techniques*

- Clock gating
- Power gating
- Variable frequency
- Variable voltage supply
- Variable device threshold ( $V_T$ )

The above techniques are also aimed at reducing dynamic power and leakage power:

### *(1) Dynamic Power Reduction*

- Clock gating
- Power-efficient circuits
- Variable frequency
- Variable voltage supply

### *(2) Leakage Power Reduction*

- Minimized usage of low  $V_T$  cells
- Power gating
- Back-biasing
- Reduced dynamic power
- Reduced oxide thickness ( $T_{ox}$ )
- Use of fin FETs

In this dissertation, I have used the dual-threshold, dual-oxide, and dual-supply techniques for power reduction. These techniques are described in detail in the following paragraphs.

### 2.3.1. Dual Threshold (Dual $V_T$ )

Foundries typically provide two  $V_T$  process options: high and low  $V_T$ . Having only two options forces the designer to optimize either for performance or power. Designers often use different  $V_T$  transistors for different logic blocks and logic gates within a device. That is, designers can use a low  $V_T$ , high-leakage transistors for the critical path where performance is a requirement, and high  $V_T$  transistors in parts of the chip where performance is not critical. Since the leakage current is exponentially dependent on the threshold voltage, increasing the threshold voltage would decrease the leakage current substantially. However, the high-threshold-voltage devices have larger switching delays. The various leakage-current mechanisms and some leakage reduction techniques for CMOS circuits have been discussed in [63] and [103]. The techniques for reducing leakage power involve static and dynamic approaches. The dynamic approach,

The dual  $V_T$  (DVTCMOS) design technique, which is a static approach, has been widely used in the custom VLSI designs for reducing leakage power. The DVTCMOS implementation reduces both the active and the standby leakages. Further, there is no performance degradation in a DVTCMOS implementation for custom VLSI designs. This technique uses two kinds of transistors in the same circuit. Some transistors have a high threshold voltage, and other transistors have a low threshold voltage. The high-threshold-voltage transistors have less subthreshold leakage-power dissipation but also have a larger delay as compared to the low-threshold-voltage transistors.

### 2.3.2. Dual Oxide (Dual $T_{ox}$ )

Leakage current is a primary concern for low-power, high-performance digital CMOS circuits for portable applications, and industry trends show that leakage will be the dominant component of power in future technologies. New leakage mechanisms, such as tunneling across



thin gate oxides, which lead to gate oxide leakage current ( $I_{gate}$ ), are coming into play from the 90 nm node onwards. According to the ITRS, a high-performance CMOS device will require gate oxide thicknesses of 0.7 to 1.2 nm, thus leading to gate leakage due to carrier tunneling through the ultra thin layer of gate oxide [5]. The probability of electron tunneling is a strong function of the barrier height (i.e., the voltage drop across gate oxide) and the barrier thickness, which is simply  $T_{ox}$ . A small change in  $T_{ox}$  can have a tremendous impact on  $I_{gate}$ .

The other component of leakage, subthreshold leakage ( $I_{sub}$ ), forms a reducing fraction of the total leakage as  $T_{ox}$  is reduced, so that  $I_{gate}$  becomes the dominant leakage mechanism at nanoscale. The dual oxide technique explores the use of dual  $T_{ox}$  values for minimizing leakage minimization and maintaining performance at the same time. A higher oxide thickness ( $T_{ox-H}$ ) leads to increased delay. The dual  $T_{ox}$  technique involves higher oxide thickness ( $T_{ox-H}$ ) assignment to transistors in the non-critical path and lower oxide thickness ( $T_{ox-L}$ ) assignment to transistors in the critical path. Thus, by using this technique, one can suppress gate oxide leakage while maintaining the speed of the circuit.

### 2.3.3. Dual Supply (Dual $V_{dd}$ )

Although a dual  $V_T$  design helps engineers minimize leakage of their designs, another technique, dual supply design, helps designers control dynamic power. Similar to dual threshold design, dual supply design enables designers to give the critical paths and blocks in their designs access to maximum voltage for the process and specification, but the designers then reduce the voltage for less power-hungry blocks. For example, a processor block may require a clock speed of 500 MHz, but a universal serial bus (USB) core may require only 30 MHz to comply with the USB protocol and thus require less voltage to run. So, if designers give the USB core only the power it needs, they can drastically reduce the overall power that the design consumes. To

implement the method, designers traditionally put level shifters between blocks that are running at different voltages. If there is a 0.9 V region on an IC design that is sending a signal to a 1.2 V region, it is necessary to put a level shifter between the two regions so that it is possible to boost it to the swing in voltage and control timing.

Although a fairly simple concept, its implementation is more complex. First, designers must get used to dealing with multiple voltages on a die. There are also some fairly significant challenges on the tools front. Most commercial synthesis and physical-design tools can insert level shifters and can perform multivoltage, but creating a register transfer level (RTL) is a problem. Hardware description languages (HDLs) do not yet have a mechanism for describing power connectivity. This lack is one area that electronic design automation (EDA) vendors are addressing by trying to implement a low-power standard.

Another emerging method that started in custom design but is making its way into application specific integrated circuit (ASIC) design is the use of parallelism with voltage scaling. Parallelism is done to get the performance up, and then voltage is scaled down to reduce the power and energy. If one looks at dynamic power, voltage is clearly where the biggest gains will be. Given a timing constraint of 2 ns, for example, one first overachieves the timing objective. In particular, parallelism is added to get the critical path down to 1.2 ns. Then, the voltage is scaled down to relax back to the 2 ns cycle time achievement is needed. The decrease in voltage more than compensates for the increase in area.

## CHAPTER 3

### RELATED PRIOR RESEARCH

In this chapter, I present a survey of the current literature related to the research presented in this dissertation. Section 3.1 and section 3.2 deal with literature on low-power design techniques such as dual supply voltage ( $V_{dd}$ ), dual threshold voltage ( $V_T$ ), and dual oxide thickness ( $T_{ox}$ ). Section 3.3 and section 3.4 discuss the current research on process variation and parasitic-aware research. This discussion is followed by current literature related to the mixed-signal circuits discussed in section 3.5.

#### 3.1. Dual Supply and Dual Threshold

The research using the dual  $V_{dd}$  technique is quite mature, and several approaches have been proposed in the literature over the past several years [18, 86, 59]. Certain types of circuitry called level converters are used for this purpose. The transistors on critical paths are operated on a higher supply voltage ( $V_{ddh}$ ), whereas transistors on the non-critical paths are operated on a lower supply voltage ( $V_{ddl}$ ) [70, 57]. Dual  $V_{dd}$  and dual  $V_T$  designs are becoming increasingly popular because of the rising leakage current levels of ultra-small metal oxide semiconductor field effect transistor (MOSFETs) [34, 115]. Decreasing the supply voltage is an effective way of reducing power. However, the delay increase that is due to the reduction in supply voltage causes reduction in the throughput of the circuit. In order to maintain circuit speed, it is necessary to reduce  $V_T$ . This reduction, however, leads to an exponential increase in leakage current. Setting some of the transistors to high  $V_T$  and low  $V_{dd}$  allows maintaining overall performance while reducing leakage current [113, 69, 114]. Multiple threshold CMOS has been used by Pant et al. [95] for subthreshold current reduction. Khouri and Jha [64] proposed a dual  $V_T$  technique for subthreshold leakage analysis and reduction during behavioral synthesis, targeting the least used

modules as the candidates for leakage optimization. Gopalakrishnan and Katkoori in [51, 52] also use the multi-threshold CMOS approach for reduction of subthreshold current during high-level synthesis and propose binding algorithms for power, delay, and area trade-off. They used a clique partitioning approach in [52] and a knapsack-based binding algorithm in [51]. In [35], Liu et al. applied probabilistic analysis to  $V_T$  variation. Dual  $V_T$  design methodology was analyzed in the presence of large variations in threshold voltage. In [7], a dual  $V_T$  and dual  $T_{ox}$  technique was applied to static random access memory (SRAM) in order to reduce leakage. In [71], a dual  $V_T$  field program gate array (FPGA) architecture has been proposed in which the logic elements are used for dual  $V_T$  assignment. In [33], Wei et al. tried to reduce the leakage power by using high  $V_T$  transistors in the non-critical paths and low  $V_T$  transistors in the critical paths.

### 3.2. Dual Oxide

In [90], Mukherjee et al. have proposed a gate oxide leakage minimization approach using dual  $T_{ox}$  and dual  $K$ . In [84], Mohanty et al. presented analytical models and a data-path scheduling algorithm for reduction of tunneling current. The heuristic assigns higher thickness resources to more leaky nodes (multipliers) but does not address the area overhead. In [75], Lee et al. developed a method for analyzing gate oxide leakage current in logic gates and suggested utilizing pin reordering to reduce gate leakage. In [29], Sultania et al. developed an algorithm to optimize the total leakage power by assigning dual  $T_{ox}$  values to transistors in a given circuit. In [112], Sirisantana and Roy used multiple channel lengths and multiple gate oxide thickness for reduction of leakage. In [91], Mukhopadhyay et al. have carried out extensive modeling and estimation of total leakage current of complementary metal oxide semiconductor (CMOS) devices considering the effect of parameter variation. In [46], the authors proposed application of dual  $T_{ox}$  technique at circuit level to power-hungry transistors of a given circuit.

### 3.3. Process Variation

As the device technology scales down to nanometer region, intra-die variations such as gate oxide thickness ( $T_{ox}$ ) and threshold voltage ( $V_T$ ) variations have become as important as inter-die variation when analyzing circuit performance and predicting the yield of a chip [17, 13, 14, 117]. With rising concerns of intra-die variation, some of these investigations which modeled process variations and performed timing analysis have been proposed [28, 94, 36]. Supply voltage ( $V_{dd}$ ) variations also need to be considered during performance estimation.

Several research works address process variation in nano-CMOS circuits. In [66], a current-controlled oscillator was subjected to process variations. In [83], the authors showed the effect of simultaneous variation of supply and process parameters on power consumption of data-path components. In [82], the authors developed process variation aware component libraries. This work focused on behavioral (high-level) synthesis. An increase in the number of variation sources has led to even more corner cases that need to be simulated for each design. In [93], the authors have estimated that the  $3\text{-}\sigma/\mu$  variation for 65 nm process technology is as high as 30% for transistor channel length and transistor threshold voltage. Future processes could have even larger amounts of variation.

### 3.4. Parasitics

Because of the high sensitivity of radiofrequency (RF) integrated circuit (IC) design to layout parasitics, a lot of research has been done in the parasitic-aware synthesis area to overcome degradations that prevent optimal performance [96, 12] because of device and package parasitics. Simulated annealing is proposed for synthesizing RF CMOS circuits in [22, 53, 68, 77, 20]. Optimization techniques such as particle swarm optimization are proposed for parasitic-aware design in [23]. In [25], an inductor-capacitor (LC)-based, voltage-controlled oscillator

(VCO) has been subjected to a parasitic-aware synthesis. A parasitic- and process-aware design flow has been proposed in [48]. In [67], the center frequency has been optimized using a design of experiments approach. A simulation-based circuit synthesis example is presented in [130].

### 3.5. Literature Related to Mixed-Signal Circuits

The current literature on mixed-signal circuits is discussed in this section. Four mixed-signal circuits widely used for various applications in the electronics industry today are discussed:

- Analog-to-digital converters
- Voltage-controlled oscillators
- Level converters
- Active pixel sensors

#### 3.5.1. Analog-to-digital Converters

Analog-to-digital converter (ADC) design is a bottleneck in system-on-a-chip (SoC) design. There is a need for more sophisticated circuitry in terms of speed, area, noise immunity and adaptability to the digital process. Recent ADC literature deals with issues of comparator offset cancellation [26], using capacitive interpolation to eliminate power-hungry resistive ladders [30] or simplifying the comparator design [32]. In [108], an average termination circuit was proposed to reduce power consumption. The problem of metastability at high sampling speeds was addressed in [119]. The SoC integration problem faced by ADCs has not been given sufficient attention. In [127], the authors proposed a solution using the threshold inverting technique. In [111], Song et al. proposed an ADC operating at 1 V but the technology is not nano-CMOS. Low-voltage ADC designs generally need to use voltage-boosting techniques [6]

or low-threshold processes [41]. The authors in [45] proposed an ADC design at 45 nm, but it is not supported with the physical design.

Table 3.1 compares the proposed ADC of this dissertation with other ADCs described in the current literature. For fair comparison, only 6-bit, flash-type architecture ADCs have been chosen. The table shows that the proposed ADC is suitable for nanoscale SoCs; has superior integral nonlinearity (INL) and differential nonlinearity (DNL) (expressed in least significant bit [LSB]) performance; and is a low-voltage, low-power, high-speed design.

Table 3.1. Comparative Perspective of Existing 6-bit Flash ADCs

Works	Technology(nm)	DNL(LSB)	INL(LSB)	V <sub>dd</sub> (V)	Power(mW)	Rate(GS/s)
Geelen [44]	350	< 0.7	< 0.7	3.3	300	1.1
Uyttenhove[119]	350	--	--	3.3	--	1
Donovan [26]	250	--	--	2.2	150	0.4
Tseng [32]	250	< 0.1	< 0.4	2.5	35	0.3
Yoo [60]	250	--	--	2.5	66.87	1
Scholtens [108]	180	--	0.42	1.95	328	1.6
Sandner [30]	130	< 0.4	<0.6	1.5	160	0.6
My research	90	0.459	0.344	1.2	3.875	1
	45	0.7	0.46	0.7	8.8μ	0.1

### 3.5.2. Voltage-controlled Oscillators

Analog or mixed-signal designs require accurate frequency or time reference signals. Phase-locked loops (PLLs) are used to provide such stable references [16] and one of the important components of a PLL is the voltage-controlled oscillator (VCO) [9]. The VCO

produces the necessary frequency in the PLL used to synchronize with the reference signal and increases or decreases its frequency of operation, depending on the increase or decrease in the control voltage supplied to it [10]. Most commonly, LC oscillators and ring-type oscillators are used for this purpose. In today's generation of nanoscale technology, LC oscillators cannot be used because the inductors are quite large and hence cannot be scaled down to the minimal dimensions of technology. Ring oscillators, which are realized by using transistors, are more suitable for technology scaling, because they have an on-chip area saving advantage [58].

Various VCO architectures using the cross-coupled technique on n-type metal oxide semiconductor (NMOS) and p-type (PMOS) transistors are given in [27], and their advantages and disadvantages are discussed. Tuning of the VCO at a desired frequency is required for fast acquisition. The acquisition time increases in proportion to the initial frequency difference and the inverse of loop bandwidth [56]. An extended frequency range CMOS monolithic VCO design has been presented in [124], where a wide range of frequency can be achieved without any preregistered settings by using analog feedback control. A number of PLL and VCO designs are presented in [100]. The authors in [74] studied high-performance designs using CMOS processes. Low-power VCOs are presented in [73, 101, 89, 79]. Jitter and phase noise were studied in [80] and [54]. A tabular comparison of my research with the existing literature (table 3.2) reveals the design proposed in this dissertation to be a high-performance VCO at nanoscale technology.

Table 3.2. VCO Performance Comparison

Works	Technology (nm)	Performance (GHz)
Tiebout [89]	250	1.8
Dehghani [101]	250	2.5
Long [79]	180	2.4
Kwok [73]	180	1.4
My research	90	2



### 3.5.3. Level Converters

A comparative perspective of selected related research works on level converters is presented in table 3.3. In a multiple supply voltage (MSV) system, it is essential to consider the overhead caused by the level converters [102]. MSV implements pipeline flip-flops along with level converters at the end of low  $V_{dd}$  clusters [102] to overcome this overhead. The flip-flops, combined with level converters, perform the operation of latching and level conversion at the same time. Such flip-flops are called level converting flip-flops. In [57], key properties and design metrics of a level converter for dual  $V_{dd}$  systems are examined. Traditional level-converter circuits, like cross-coupled level converters (CCLC), single-supply diode voltage Limited buffer level converters (SSLC), pass transistor half-latches (PHL), and precharged circuits, have been studied. Several new level-converting flip-flop circuits are also proposed. These new designs are compared to the above-mentioned traditional level converting circuits in terms of level converter performance and robustness as well as system-level performance and robustness. The proposed level-converting flip-flops exhibit improved energy-delay product values, reduced system-level power, and better immunity to supply noise without significant layout area penalties.

In [128, 129, 70], and [104], the authors studied a conventional level-converter circuit known as dual cascode voltage switch (DCVS). The DCVS circuit is a small circuit consisting of a PMOS pair connected back to back, which acts as a differential pair. Each of the above-referenced papers proposes new level converter designs considering DCVS as a baseline design. In [104], a new level-converter circuit based on the keeper transistor concept was proposed. The keeper transistor serves as a level restorer in the pass transistor logic [15]. The authors also compared the performance of the proposed circuit and the traditional DCVS by calculating the delay, power, and energy-delay product.

Novel asynchronous level-converters were proposed in [70]. The simulation results showed that the proposed designs consume 8% to 50% less energy at equivalent or better speeds compared to the other designs at 0.13  $\mu\text{m}$  CMOS technology. A new level-converter design based on DCVS was presented in [129]. The authors also compared the speed and power consumption of their level converter design and DCVS. In [128], a novel circuit called symmetrical dual cascode switch (SDCVS) was proposed. The authors addressed the contention problem of DCVS and provided a solution for it, stating that the contention problem gave rise to increased delay time and power consumption.

Two additional NMOS transistors were added to the DCVS design to eliminate the contention problem. Two new logic level-converter designs were presented in [65]. The two designs are dynamic logic level-converter (DLC) and dynamic logic level-converter for duty ratio converting. These two designs were applied to a 72-Mb double-data-rate (DDR) SRAM, which allowed the chip to operate at a low voltage of 1.2 V when the supply voltages were around 1.5 V or 1.8 V. The DLC design consisted of a self-resetting dynamic CMOS logic, which made it much faster in operation.

In [62], a distinct level down converting circuit was proposed. This circuit consisted of a differential input pair circuit acting as the level converting circuit. This level-converter provided stable operation for low-voltage and high-speed use [62]. The circuits used thin gate-oxide MOSFETS, which enabled a faster level conversion. The differential input pair of this level converter offered a high immunity against power supply bouncing. In [104], only the issue of short-circuit power dissipation was handled. The SDCVS achieved 50% power reduction and 60% speed increase. However, this reduced short-circuit power dissipation only. The design I propose in my dissertation achieves 83% power savings compared to the original baseline

design. For fair comparison of power consumption, I used my baseline design because the other designs presented were different in technology as well as functionality. In addition, the proposed design achieved 60% delay compared to that reported in existing works [57].

Table 3.3. Comparative Perspective of Level-converters

Works	Technology (nm)	Power ( $\mu$ W)	Delay	Conversion	Design Approach
Ishihara [57]	130	--	127ps	Level-up/ down	Level converting flip flops
Yu [128]	350	220.57	--	Level-up	SDCVS
Sadeghi [104]	100	10	1ns	Level-up	Pass transistor and Keeper transistor
My research	90	16.68	80.4ps	Level-up/ down and block	All conversion types and programmability

#### 3.5.4. Active Pixel Sensors

The scaling of CMOS technologies has accelerated in recent years and will arguably continue toward the 10 nm node regime [5]. Advanced circuit design exploration must start before future technologies are fully developed in order to solve design challenges posed by nanoscale CMOS technology. Particular examples of these emerging challenges include leakage current, process variations, and transistor reliability. In [61], the authors examined mismatch in photo-detectors at 2  $\mu$ m and 1.2  $\mu$ m CMOS processes. In [40], the authors presented results for pixel mismatch. In [31, 123], low-voltage APS designs were proposed. The authors in [122] presented recent advances in image sensors with device scaling considerations. In [106], the authors analyzed the effect of technology scaling on readout time. A multiple-resolution APS was presented in [8].

Table 3.4 provides a broad overview of the existing works on APS array. The APS I propose in this dissertation has been designed with the smallest CMOS technology, has

the lowest power dissipation, and operates at the lowest supply voltage. Thus, my proposed APS is more suitable for target nanoscale SoC applications.

Table 3.4. Comparative Perspective of Existing APS Designs

Works	Technology (nm)	$V_{dd}$ (V)	$P_{APS}$ (W)	$V_{swing}$ (V)	DR (dB)
Xu [123]	250	1	520n (pixel)	0.55	71
Weng [121]	250	1.8	--	0.5	--
Cho [19]	350	1.5	550 $\mu$ (array)	--	--
My research	32	0.9	16.3 $\mu$ (array)	0.428	59.47

## CHAPTER 4

### PROPOSED LOW-POWER DESIGN AND OPTIMIZATION METHODOLOGIES

This chapter constitutes the main original contributions of this dissertation. The issue of process variation and how it is becoming a major obstacle for nanoscale design is discussed first. Next is an explanation of optimization methodologies for power, parasitic-aware and process-variation-aware designs at nanoscale.

#### 4.1. Issue of Process Variation

Semiconductor designers are facing numerous challenges as they migrate their existing designs or start new designs in 90 nm, 65 nm and finer process geometries. Two of the biggest challenges are the increasing power specifications because of leakage power and potential yield loss caused by increasing process variations.

Designing for yield is an afterthought in today's design flows, whether it is digital, analog/radiofrequency (RF), or mixed-signal. The lack of design for yield tools has forced the digital world to accept overly pessimistic guardbands as the norm. Just as in digital design where interconnect delays make or break a design, the move to 90 nm and lower process technologies means that the variations in process parameters have a resounding effect on the performance metrics of analog/mixed-signal, memory and RF circuits.

A digital circuit is typically optimized only for speed and power, whereas an analog circuit is designed to meet as many as 5 to 10 performance metrics. As a result, the impact of these process variations is seen as design yield loss. A proactive and a deterministic way is needed to deal with performance and yield while in the design phase, and not after first silicon. Design yield, also known as parametric yield, is a design's sensitivity to process variations. In general, designers verify the operation of their circuits at the center point of the process, which is

also called the nominal point. In addition, they verify the operation of their circuits at the typical four worst-case “corner” points.

The nominal point is not necessarily “the best operating point for that process,” but is easiest for fabrication to control. However, the reality is that with the variations that process parameters exhibit and the nonlinear nature of analog/RF circuits, the design must operate across the entire range of process and operating conditions, not just the nominal and the four worst-case points. Current tools analyze and optimize a design only for the nominal point without sweeping across the full range of process and operational parameters. A significant part of the loss in yield of a design can be attributed to parametric yield, and it is typically on the order of 20%.

Simulation and nominal optimization tools analyze a design only for a fixed process point (typically the nominal or, supposedly, the worst-case point). They fall short of optimizing true parametric yield based on process variations. Yield optimization with built-in sensitivity analysis and full knowledge of the distribution of process variations is critical to understanding the factors that contribute to parametric yield and to optimizing the design to achieve the maximum yield. The impact of the variations in the process parameters and operating conditions of the performance factors of a design is much more for nanometer than the sub-micron technologies. Hence, the nominal operating point, which is the center of the distribution of the parameters for a given process, may not be the best operating point for design yield.

What is really needed is an automated way to maximize design yield such that the design operates as specified across the entire process and operating environment. When an analog/mixed-signal or memory design is optimized for multiple performance parameters, the worst-case condition may be different for each performance parameter such as gain, bandwidth, and jitter [54]. Trying to simultaneously optimize a design for each such performance parameter can

be a nightmare and is typically beyond what an individual can assimilate. Furthermore, net yield is determined by the design simultaneously meeting all those requirements.

It is common to address design yield problems after a design is manufactured. Engineers will track a low-yielding wafer to see what process variations cause the yield loss. Then, they will run simulations to see where the design should be tweaked to improve yield. This "redesign by autopsy" approach to addressing design yield issues is very costly compared to handling design yield at the front end of the design process using design for yield (DFY) techniques. Use of DFY techniques in the front end design process will accelerate the design flow and get the final product to market faster and with higher yield.

The following sections describe methodologies used in this dissertation for attacking this problem of yield caused by process variations and achieving low-power designs at the same time. These methodologies have been tested on specific analog/mixed-signal circuits (discussed in chapter 5) in order to verify their effectiveness.

#### 4.2. Single-Iteration Automatic Approach

The primary purpose of this approach is to address the issues of parasitic degradation and process variation in integrated circuits (ICs). To achieve parasitic closure, multiple iterations between the front-end circuit design and back-end layout will be required, according to the standard IC design flow in figure 4.1 [120]. In this figure, I have indicated the manual and automatic processes separately. I assume that the manual process requires X number of iterations. The primary purpose of the proposed design flow, called parasitic-aware design flow, is to reduce the number of manual iterations to 1 by performing the X number of iterations on a parasitic parameterized netlist instead of the layout. The parasitic parameterized netlist refers to the netlist derived from the initial physical design and then parameterized. This netlist gives the

designer a fair idea of the parasitics present in the designed circuit. The final optimal physical design is carried out after optimization and constitutes 1 iteration.

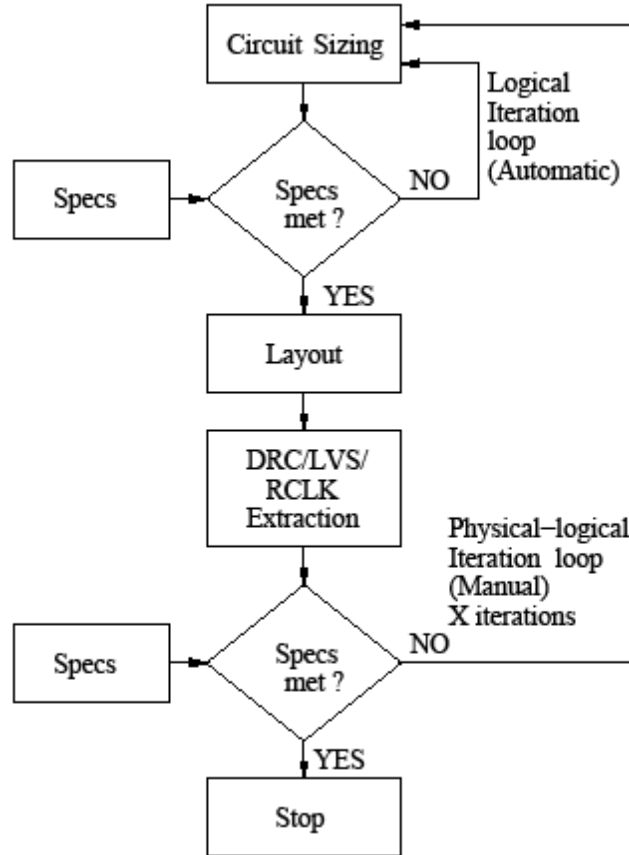


Figure 4.1. Standard IC design flow.

Hence, I reduced the X number of manual iterations required for parasitic closure to 1 manual iteration. The proposed design flow is shown in figure 4.2. The optimized physical design was then tested, and the results are presented in figure 6.4. The discrepancy in the oscillation frequency of the logical and physical design of the voltage controlled oscillator (VCO) has been reduced to 1% in a single physical design iteration. More details are given in section 6.2.1. To have a process variation robust design, I also introduced a process variation analysis step in the parasitic-aware design flow to formulate a new design flow called parasitic-



and process-variation-aware design flow. In this cycle, the parasitic parameterized netlist was subjected to worst-case process variations.

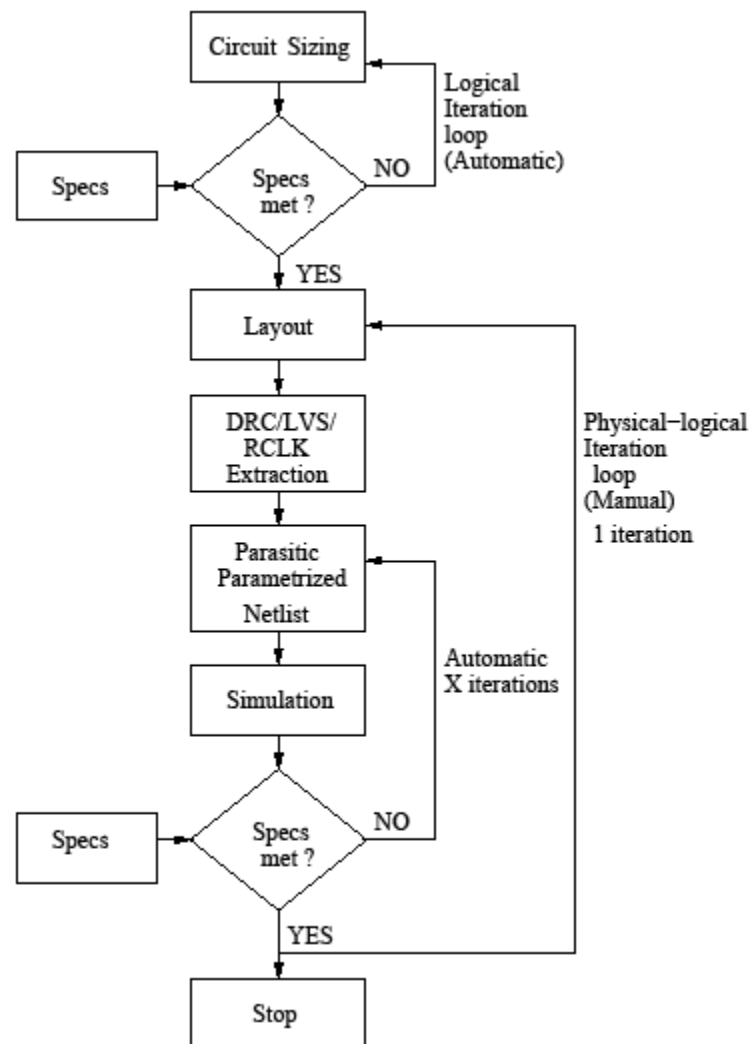


Figure 4.2. Proposed parasitic-aware IC design flow.

The final physical design was carried out with the optimized parameters obtained from the netlist optimized for a worst case process variation environment constituting 1 iteration. A nano-complementary metal oxide semiconductor (CMOS) VCO has been subjected to this methodology; the results are presented in chapter 6. This procedure (shown in figure 4.3) ensures that the resulting final physical design is not only resistant to parasitic effects but is also tolerant

to process variations. These are novel methodologies for physical design of nano-CMOS RF components to meet the required design specifications. In both procedures, a 1-iteration approach (see algorithm 1) is followed, in which the layout has to be done only twice, once before the optimization and once after the optimization. In this communication, the fully extracted physical design consisting of resistors (R), capacitors (C), inductors (L) and mutual inductors (K) is optimized to meet the target specification.

### Algorithm 1

#### Algorithm Used for Optimization in the Single-iteration Automatic Approach

- 1: Input: parasitic parameterized netlist, objective set  $F$ , stopping criterion  $S$ , design variable set  $D$ , lower design constraint  $C_{lower}$ , upper design constraint  $C_{upper}$ .
- 2: Output: optimized objective set  $F_{optimized}$ , optimal design variable set  $D_{optimal}$  for  $S = \pm \beta$ .  
{where  $2\% \leq \beta \leq 5\%$ }
- 3: Run initial simulation in order to obtain feasible values of design variables for the given specifications.
- 4: while ( $C_{lower} < D < C_{upper}$ ) do {This loop outputs optimal design variable set  $D_{optimal}$ }
- 5: Using conjugate gradient method, generate  $D' = D \pm \delta D$ .
- 6: Compute objective set  $F$ .
- 7: if ( $S = \pm \beta$ ) then
- 8: return  $D_{optimal} = D'$ .
- 9: end if
- 10: end while
- 11: Using design variable set  $D_{optimal}$ , construct final physical design and simulate.
- 12: Record objective set  $F_{optimized}$ .

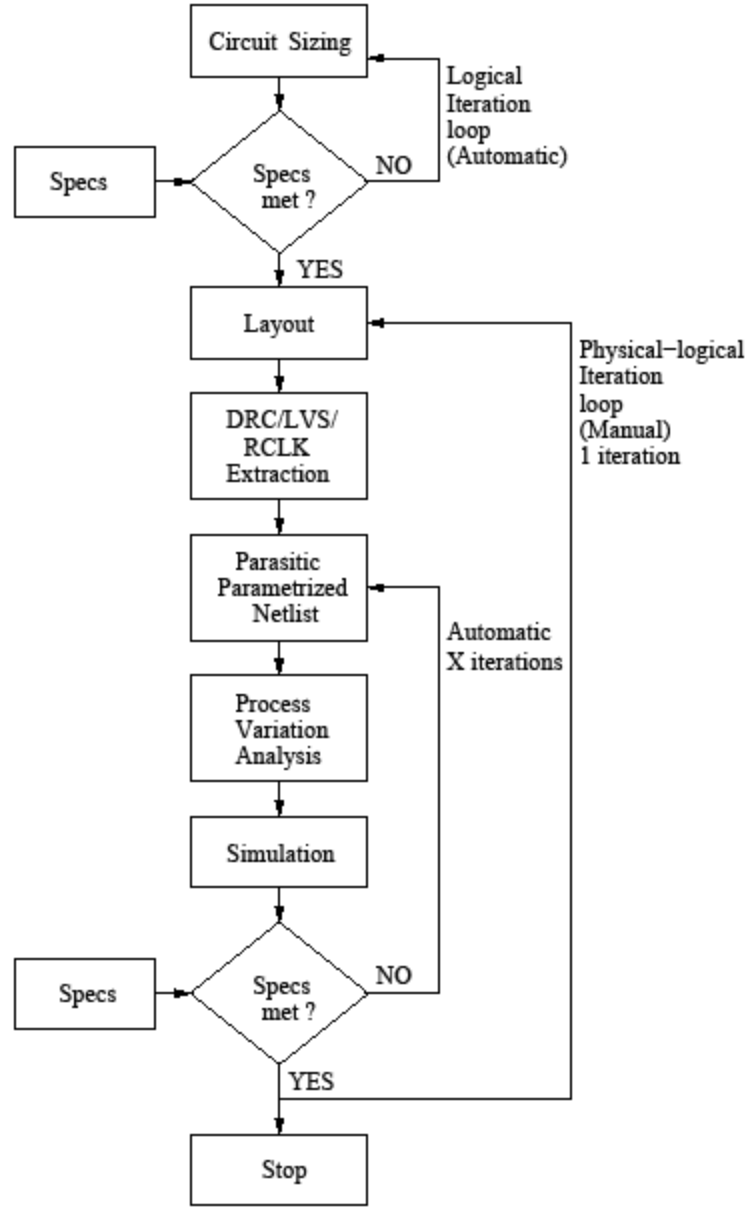


Figure 4.3 Parasitic- and process-variation-aware IC design flow.

Algorithm 1 presents the optimization used in the single-iteration approach. The inputs to the algorithm consist of the parasitic parameterized netlist, the objective set  $F$  with its stopping criterion  $S$  (which is the specification required for successful design closure), and the design variable set  $D$  with its lower constraint  $C_{lower}$  and upper design constraint  $C_{upper}$ . The outputs of the algorithm are the optimized objective set  $F_{optimized}$  within the specifications and the

corresponding optimal values of the design variable set  $D_{optimal}$ . First, a simulation is run using the initial values of  $D$ , and the value of  $F$  is calculated to determine whether the initial values are feasible for the given  $F_{optimized}$  (which are the specifications for the design as shown in figure 4.3). In the next iteration, the design variable set ( $D$ ) values are changed by using *conjugate gradient method*, to achieve the required  $F_{optimized}$ . The circuit is simulated again by using this new design variable set. This process continues until  $F$  meets the stopping criterion  $S$ .

#### 4.3. Hybrid Monte Carlo and Design of Experiments (DOE) Approach

The general convention used to determine a given circuit's yield is Monte-Carlo analysis: A large number of parameter sets is generated, using a normal distribution with the process standard deviations (presumed to be known); and the number of samples within specifications is determined. A DOE is used to determine the influence of variation of fabrication parameters on measurable quantities. The advantage is that only a very limited amount of experiments needs to be performed from which a maximum amount of information must be gained. In general, a fit of the data is performed with the measured data points. This fit can then be used to find optimal working points or to determine the expected yield of a process. Thus, while a Monte Carlo approach gives a designer an idea about the circuit's yield, a DOE approach allows the designer to reduce the number of required simulations dramatically while providing a near-optimal design. A novel algorithm for optimization of any given circuit is discussed in Algorithm 2. The proposed algorithm takes advantages of both the strengths of Monte Carlo analysis and DOE.

#### Algorithm 2

##### Proposed Monte Carlo/DOE-based Algorithm for Variability-Aware Optimization

- 1: Input: Baseline circuit, Objective set  $F$ , design variable set  $D$ .
- 2: Output: Optimized circuit,  $F_{optimized}$ ,  $D_{optimal}$ .

- 3: for (each corner of design variable set  $D$ ) do
- 4: Run Monte Carlo simulation for  $N$  runs.
- 5: Record Monte Carlo Data for  $F$ .
- 6: Normalize the Monte Carlo data for  $F$ .
- 7: Record  $\mu_F, \sigma_F$ .
- 8: end for
- 9: Using DOE, obtain prediction equations for  $\hat{\mu}_F, \hat{\sigma}_F$ .
- 10: Form objective function:  $f_F = \hat{\mu}_F \pm 3 \times \hat{\sigma}_F$ .
- 11: while All corners of design variable set  $D$  not explored do
- 12: Compute  $f_F$ .
- 13: if ( $f_F = \text{acceptable}$ ) then
- 14: return  $D_{\text{optimal}} = D$ .
- 15: end if
- 16: end while
- 17: Replace  $D = D_{\text{optimal}}$  in baseline circuit. Circuit obtained is optimized. Simulate optimized circuit.
- 18: Compute  $F = F_{\text{optimized}}$  from optimized circuit.

The presented optimization algorithm is very suitable for power-aware design of circuits while being subjected to process variation. The inputs to the algorithm are the baseline circuit, the objective set  $F$ , which may be power and delay for a given circuit; and the design variable set  $D$ , which consists of quantities under the designer's control (for example, the widths of transistors and supply voltage). The output of the algorithm is a circuit, which gives the

optimized values of  $F$  ( $F_{optimized}$ ), and the values of the design variable set, which give this optimized circuit ( $D_{optimal}$ ).

The first stage of the algorithm involves Monte Carlo data collection. In this stage, for each corner of the design variable set  $D$ ,  $N$  Monte Carlo runs consider process variation or mismatch or both, depending on the designer's requirement. The data for  $F$  is recorded and normalized, from which the mean ( $\mu_F$ ) and standard deviation ( $\sigma_F$ ) are calculated. Thus,  $\mu_F$  and  $\sigma_F$  are obtained for each corner of the design variable set  $D$  in the Monte Carlo data collection stage.

The next stage is the DOE. Using DOE, I obtained prediction equations for  $\mu_F$  and  $\sigma_F$ , called  $\hat{\mu}_F$  and  $\hat{\sigma}_F$ , which show the dependence of  $F$  on the design variable set  $D$ . This was followed by formation of the objective function  $f_F$ . If  $F$  is the power of the circuit under consideration, optimization would refer to power minimization. Hence, the objective function:

$$(6) \quad f_F = \hat{\mu}_F + 3 \times \hat{\sigma}_F$$

where  $f_F$  has to be minimum. Once the objective function was formed (equation 6), I computed  $f_F$  for all the design corners of  $D$ , and the acceptable value was chosen. For example, if power is considered, then the minimum value will be acceptable. The design corner, which gave this acceptable value, is called  $D_{optimal}$ . Using this  $D_{optimal}$ , the circuit was simulated; and the corresponding value of  $F$ , i.e.,  $F_{optimized}$ , was obtained. Hence an optimized circuit was obtained. This approach has been used to optimize an  $8 \times 8$  APS array (presented in chapter 6). Figure 4.4 shows the theory behind the formation of the objective functions. The idea is that  $\mu_{baseline}$  of the figure of merit to be optimized needs to be shifted left or right, depending on whether it needs to be minimized ( $\mu_{minimized}$ ) or maximized ( $\mu_{maximized}$ ). The  $3 \times \sigma_{baseline}$  of the figure of merit (which is

a measure of the spread) also needs to be minimized to  $3 \times \sigma_{\text{minimized}}$ . A  $3 \times \sigma$  limit has been considered, so that 99.5% of all the figure-of-merit values will fall within the  $3 \times \sigma$  limit.

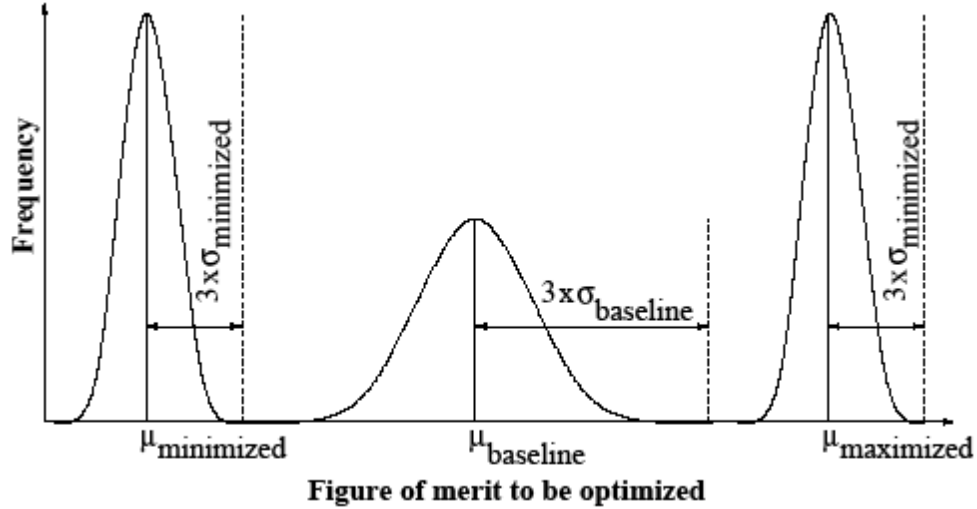


Figure 4.4. Aim of the hybrid Monte Carlo and DOE-based optimization.

#### 4.4. Corner-based Methodology

For robust designs, the influence of process variations has to be considered during circuit simulation. I propose a corner-based method that covers the process spread with a minimum number of simulation runs. This methodology may be applied to process (say, threshold voltage  $V_t$ ) as well as design parameters ( $V_{dd}$ ) while testing a circuit's robustness against process variations. Consider two parameters in a given circuit:

- $V_{tn}$ : NMOS transistor threshold voltage.
- $V_{tp}$ : PMOS transistor threshold voltage.

During CMOS fabrication, threshold voltage implantation for p-type metal oxide semiconductors (PMOS) and n-type metal oxide semiconductors (NMOS) are separate steps; hence these two parameters are considered independent of each other. Thus for simulating intra-die variations or mismatch of, say,  $\pm 5\%$ , between these two parameters, there are four process corners:

- Corner 1:  $V_{tn} -5\%$ ,  $V_{tp} -5\%$
- Corner 2:  $V_{tn} -5\%$ ,  $V_{tp} +5\%$
- Corner 3:  $V_{tn} +5\%$ ,  $V_{tp} -5\%$
- Corner 4:  $V_{tn} +5\%$ ,  $V_{tp} +5\%$

Using these four process corners, I simulated the design and measured the figure of merit under consideration. A satisfactory value of the figure of merit obtained gave an indication of whether the design was process-variation-tolerant or not. A 90 nm ADC was subjected to such a technique. The results are presented in chapter 6. This method might not be as accurate as traditional Monte-Carlo simulations, which are very time-consuming, but it is very useful in getting a quick estimate of the impact of process variation on a circuit's behavior. Figure 4.5 depicts this method.

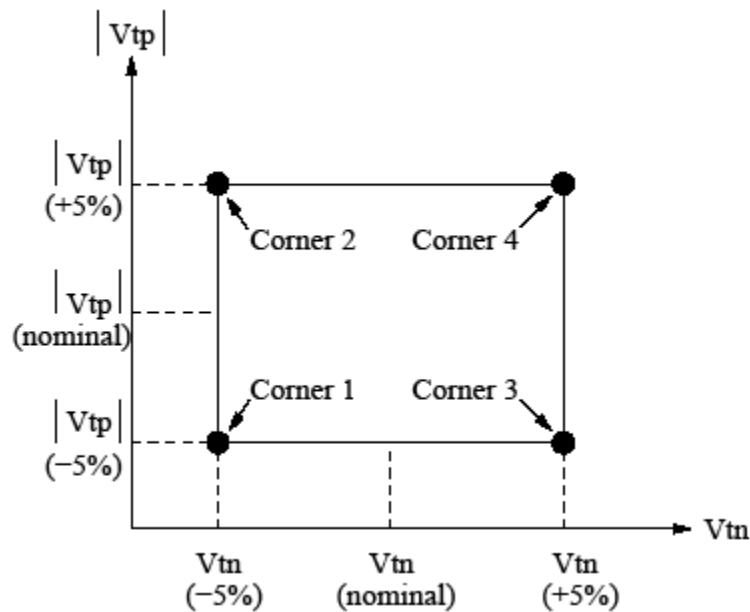


Figure 4.5. The corner-based methodology used for process variation.



## CHAPTER 5

### CASE STUDIES USING SAMPLE DIGITAL, ANALOG AND MIXED-SIGNAL CIRCUITS

In this chapter, I present the logical and physical designs of specific mixed-signal circuits, which have been used as case studies for this dissertation. These circuits are used by the industry for a variety of applications such as radiofrequency (RF), wireless, and cell phones. The post-layout functional simulation results of each of these circuits are also presented. The design of the following circuits is presented:

- 90 nm/45 nm analog-to-digital converter (ADC)
- 90 nm voltage-controlled oscillator (VCO)
- 90 nm universal voltage level converter (ULC)
- 32 nm active pixel sensor (APS)

#### 5.1. Analog-to-digital Converter (ADC)

Figure 5.1 shows the high-level representation of the 6-bit ADC [126], followed by a detailed block diagram of a flash ADC 5.2. To achieve a high sampling rate, a flash architecture is chosen. The input to the ADC is analog voltage, and the output is in the form of digital codes. An  $n$ -bit ADC requires  $2^n - 1$  comparators which are contained in the comparator bank. The comparator bank outputs a thermometer code. The position of the meniscus (the 1-0 transition) represents the analog input and is determined by the thermometer decode circuit, which consists of “1 of  $n$ ” code generators. The “1 of  $n$ ” code generators generate a “1 of  $n$ ” code which is converted to binary code using the NOR read-only memory (ROM). Hence, the output of the ADC is in the form of 6-bit binary code.

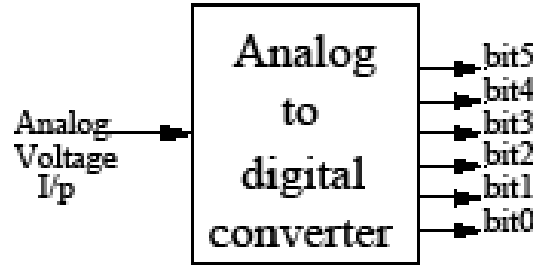


Figure 5.1. High-level representation of the ADC.

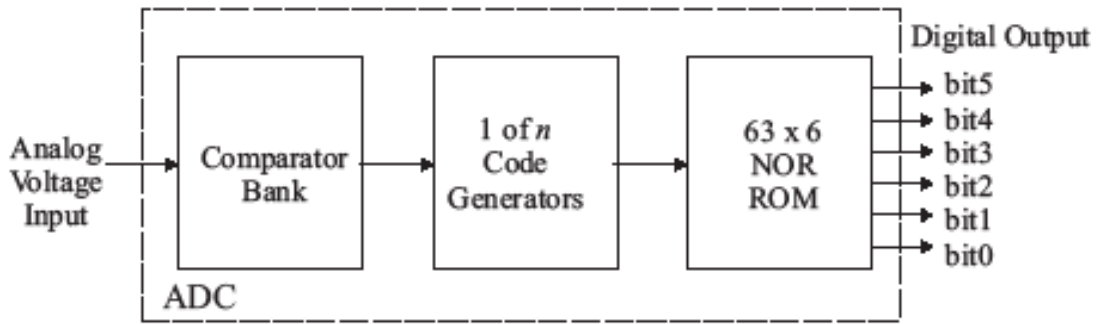


Figure 5.2. Detailed block diagram of the flash ADC.

#### 5.1.1.1. Comparator Design

The comparators in the proposed flash ADC are designed by using the threshold inverting (TI) technique [60, 76]. The TI comparator has the advantage of high speed and simplicity [76] and eliminates the need for inherently complex high-gain differential input voltage comparators and additional resistor ladder circuit [116]. The TI comparator sets its switching threshold voltage  $V_{switching}$  internally as the built-in reference voltage, based on its transistor sizes. The comparators in a conventional flash ADC are identical in size. In the TI-based ADC, all comparators have unique sizes. An  $n$ -bit ADC requires  $2^n - 1$  different comparators, each comparator having a different  $V_{switching}$  value. Hence, a total of 63 comparators for a 6-bit ADC, each comparator having a different size of transistors, is required. The switching voltage is generally calculated by using the following expression [99]:

$$(7) \quad V_{switching} = \left( \frac{\sqrt{\frac{\mu_{pmos} \times W_{pmos}}{\mu_{nmos} \times W_{nmos}}} \times (V_{dd} - |V_{tpmos}|) + V_{tnmos}}{1 + \sqrt{\frac{\mu_{pmos} \times W_{pmos}}{\mu_{nmos} \times W_{nmos}}}} \right)$$

where  $W_{pmos}$  = p-type metal oxide semiconductor (PMOS) width,  $W_{nmos}$  = n-type metal oxide semiconductor (NMOS) width,  $V_{dd}$  = supply voltage,  $V_{tnmos}$  = NMOS threshold voltage,  $V_{tpmos}$  = PMOS threshold voltage,  $\mu_{nmos}$  = electron mobility, and  $\mu_{pmos}$  = hole mobility, assuming that the PMOS length ( $L_{pmos}$ ) = NMOS length ( $L_{nmos}$ ). However, short-channel devices do not follow the square-law model used in deriving equation 7. A more suitable expression to determine the  $V_{switching}$  for short-channel devices is given by [10]:

$$(8) \quad V_{switching} = V_{dd} \times \left( \frac{R_{nmos}}{R_{nmos} + R_{pmos}} \right)$$

where  $R_{nmos}$  and  $R_{pmos}$  are the effective switching resistances for short-channel NMOS and PMOS transistors, respectively. Since the switching resistance of a transistor depends on the width (W) of the transistor, we have varied the width of the PMOS ( $W_{pmos}$ ) transistor in the TI comparator in order to achieve the 63 different switching voltages. Another reason for varying the width is that the channel length (L) of the transistor more effectively controls the performance (frequency  $\propto 1/L^2$ ). Hence,  $L$  is kept constant throughout the design and only  $W$  is varied. In the design process, a good input voltage is determined with the following equation:

$$(9) \quad \text{Input voltage range} = V_{dd} = (V_{tnmos} + |V_{tpmos}|)$$

I chose the input voltage range to vary from 493 mV ( $V_{start}$ ) to 557 mV ( $V_{end}$ ). The least-significant bit (LSB) value  $V_{LSB}$  is calculated as:

$$(10) \quad V_{LSB} = \left( \frac{\text{input voltage range}}{2^n} \right) = \left( \frac{V_{end} - V_{start}}{2^n} \right)$$

The  $V_{LSB}$  value is calculated to be 1 mV for the design process. The  $V_{LSB}$  signifies the minimum step that the ADC can distinguish. The sizes of NMOS transistors in the comparator were kept constant at 240 nm/120 nm ( $W_{nmos}/L_{nmos}$ ). For determining the sizes of PMOS transistors, we used a DC parametric sweep using an analog simulator, where the input DC voltage was varied from 0 to 1.2 V in steps of 1 mV. During this simulation,  $L_{pmos}$  was kept at 120 nm while  $W_{pmos}$  was varied from 240 nm ( $W_{pmos} = W_{nmos}$ ) to 448 nm (in steps of 1 nm) in order to obtain 63 linear quantization voltage levels. The TI comparator consists of four cascaded inverters, as shown in figure 5.3. Inverters 1 and 2 form the baseline comparator, while inverter 3 and 4 provide increased gain and sharper switching.

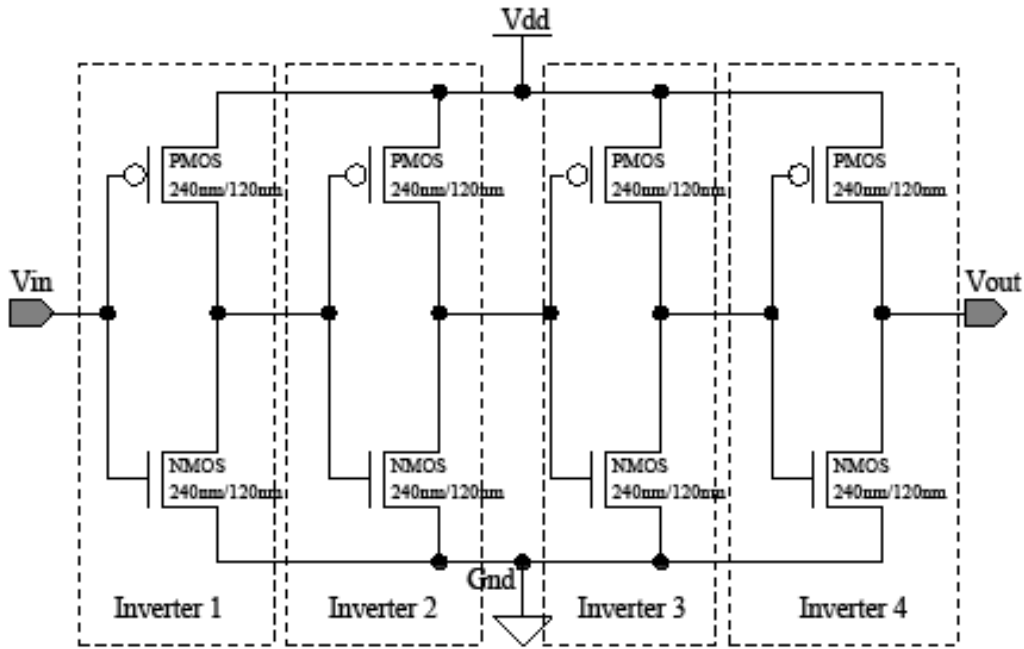


Figure 5.3. Threshold inverter (TI) comparator. (In this figure,  $W_{pmos}/L_{pmos} = W_{nmos}/L_{nmos}$ , which is the starting point for quantization.)

#### 5.1.2. 1 of $n$ Code Generator Design

The output of the comparator bank is a thermometer code. This thermometer code is converted to a “1 of  $n$ ” code using “1 of  $n$ ” code generators. A single slice of “1 of  $n$ ” code

generator consists of AND gates as combinations of an inverter followed by a NAND gate. The output from each of the AND gates is fed to the input of the NOR ROM. One of the two inputs to the AND gate is fed from the TI comparator output [24]. The other input to the AND gate is the inverted output from the next-level comparator as shown in figure 5.4.

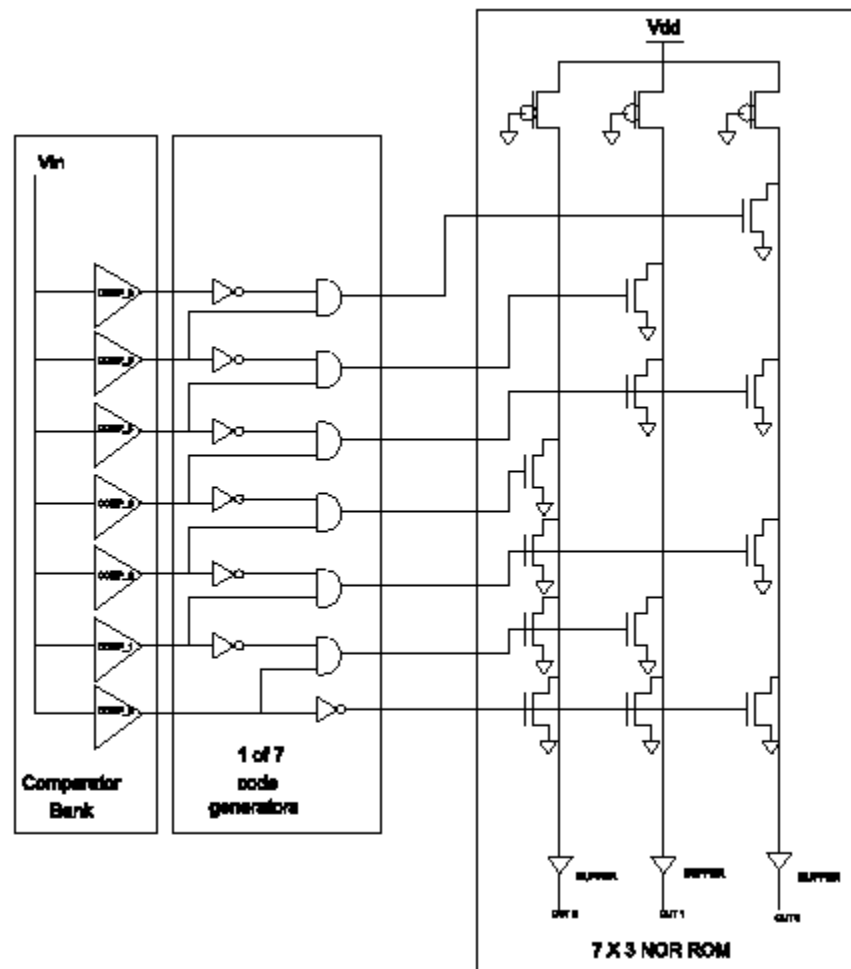


Figure 5.4. Complete circuit diagram for a 3-bit flash ADC shown for brevity. (A similar 6-bit structure has been implemented in this paper.)

### 5.1.3. NOR ROM Design

The input to the NOR ROM is a “1 of  $n$ ” code. The NOR ROM converts this “1 of  $n$ ” code to a binary code. Basically, the NOR ROM maps the  $n$ -bit address input onto arbitrary values of  $m$ -bit data output consisting of a grid of word lines (the address input) and bit lines (the

data output), selectively joined together with transistor switches. It can represent an arbitrary look-up table with a regular physical layout. As there are 63-word lines and 6-bit lines, I have designed a  $63 \times 6$  NOR ROM. The NOR ROM consists of PMOS pull-up and NMOS pull-down devices. The PMOS and NMOS sizes have been taken as 135 nm/180 nm and 180 nm/180 nm, respectively. The design decision of  $W_{pmos} < W_{nmos}$  has been taken to obtain a good voltage swing at the output so that the pull-up device (PMOS) is narrow enough for the pull-down devices (NMOS) to pull the output down safely [99]. Finally, buffers are applied at the outputs to obtain symmetrical waveforms with equalized rise and fall times. The buffer consists of two cascaded inverters having NMOS sizes of 240 nm/120 nm and PMOS sizes of 480 nm/120 nm.

#### 5.1.4. Physical Design and Characterization of ADC

The physical design of the ADC has been carried out with a generic 90 nm salicide “1.2V/2.5V 1 Poly 9 Metal” process design kit. A digital CMOS process has been used for the physical design, demonstrating the system-on-a-chip (SoC) readiness of the ADC. The three major blocks of the flash ADC (the comparator bank, the “1 of  $n$ ” code generator and the NOR ROM) have been laid out column-wise in figure 5.5. The post-layout simulation results are presented in subsequent sections. Power and ground routing consist of wide vertical bars, as can be seen from the layout, giving minimal electromigration risk and current-resistance (IR) drop. Generous use of contacts to the power and ground buses also ensures the small IR drop.

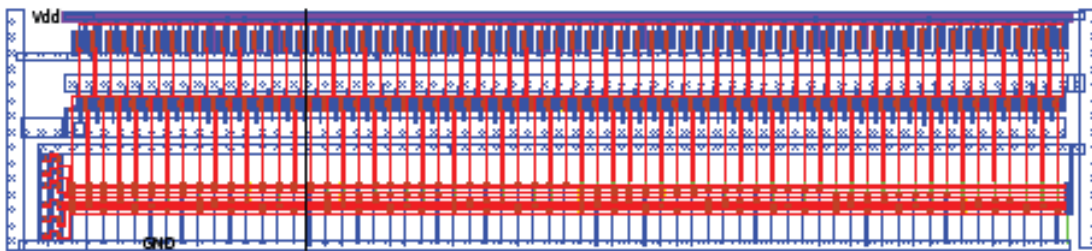


Figure 5.5. Complete layout of the 90 nm ADC.

#### 5.1.4.1. Post-Layout Functional Simulation

Figure 5.6 shows the functional simulation of the ADC obtained from the post-layout simulation. The ADC is subjected to a transient analysis, where a linearly varying ramp covering the full-scale range of the ADC is given as input. Output digital codes from 0 to 63 are obtained correctly, with no missing codes. A maximum sampling speed of 1 GS/s can be observed in figure 5.6. The least significant bit (out 0) toggles the fastest, as expected. Successive bits toggle at half the frequency of the previous one. All 64 codes of the ADC are covered as the input ramp traverses the full-scale range.

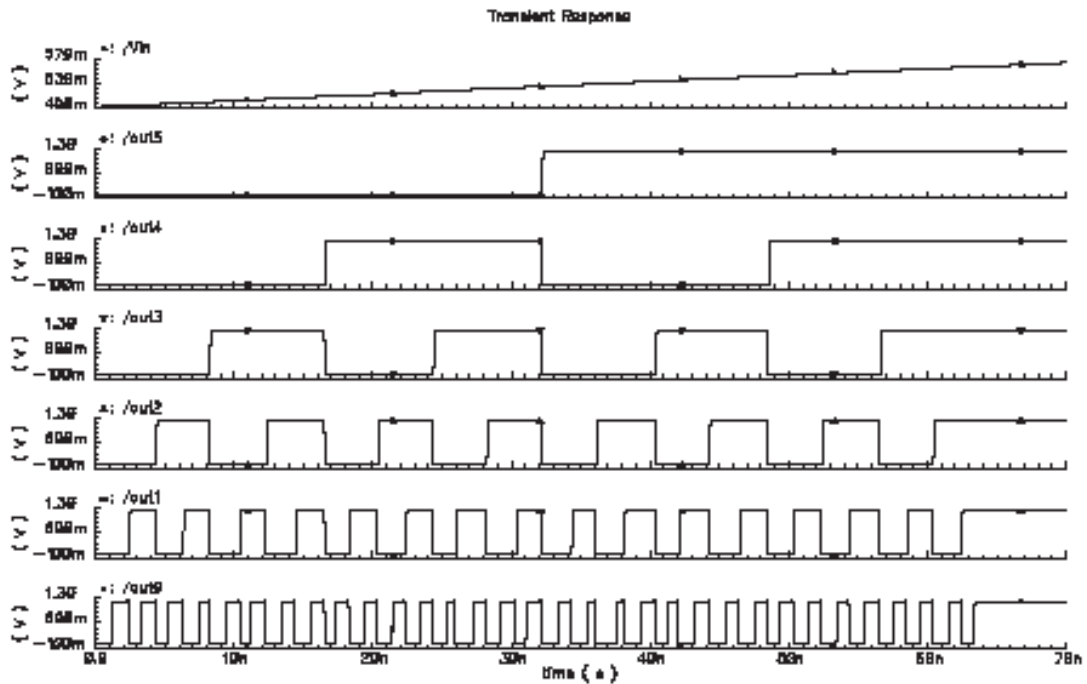


Figure 5.6. Functional simulation of the 6-bit ADC operating at 1 GS/s.

The ADC has been characterized for static and dynamic performance. The INL and DNL tests have been performed with nominal supply and threshold voltages to confirm satisfactory results before process and supply variation are introduced. The signal-to-noise and distortion ratio (SNDR) has been measured for dynamic performance. In addition, power consumption of the designed circuit has been analyzed.

#### 5.1.4.2. Static Characterization

The histogram test is commonly used for linear characterization of the ADC [2]. The proposed 6-bit ADC's integral nonlinearity (INL) and differential nonlinearity (DNL) have been measured using the histogram method. A mixed-signal simulation environment is set up, where INL and DNL calculating blocks are Verilog-A modules. The Verilog-A block generates a voltage “vout,” which is sequentially set to 4096 equally spaced voltages between  $V_{start}$  and  $V_{end}$ , which is the input voltage range for ADC conversion (section 5.1.1). At each different value of vout, a clock pulse is generated causing the ADC to convert this vout value. The resultant code of each conversion is stored. When all the conversions have been performed, the INL and DNL are calculated from the recorded data as follows:

$$(11) \quad \text{INL}[i] = \text{width}[i] + \text{INL}[I - 1] - 1$$

$$(12) \quad \text{DNL}[i] = \text{width}[i] - 1$$

$$(13) \quad \text{width}[i] = \frac{1.0 \times \text{bucket}[i]}{\text{hits} \times (\text{NUM}_{CODES} - 2)}$$

where bucket holds the number of code hits for each code, and width holds the code width calculations. The total hits between codes 1 and 62 are denoted as hits.  $\text{NUM}_{CODES}$  is the number of codes (64 for a 6-bit ADC). The maximum INL obtained is 0.344 LSB and the maximum DNL is 0.459 LSB. Figures 5.7 and 5.8 show the INL and DNL plots, respectively. Low distortion requires an ADC with a low INL. A  $\text{DNL} < 1$  LSB also ensures a monotonic transfer function for the ADC.



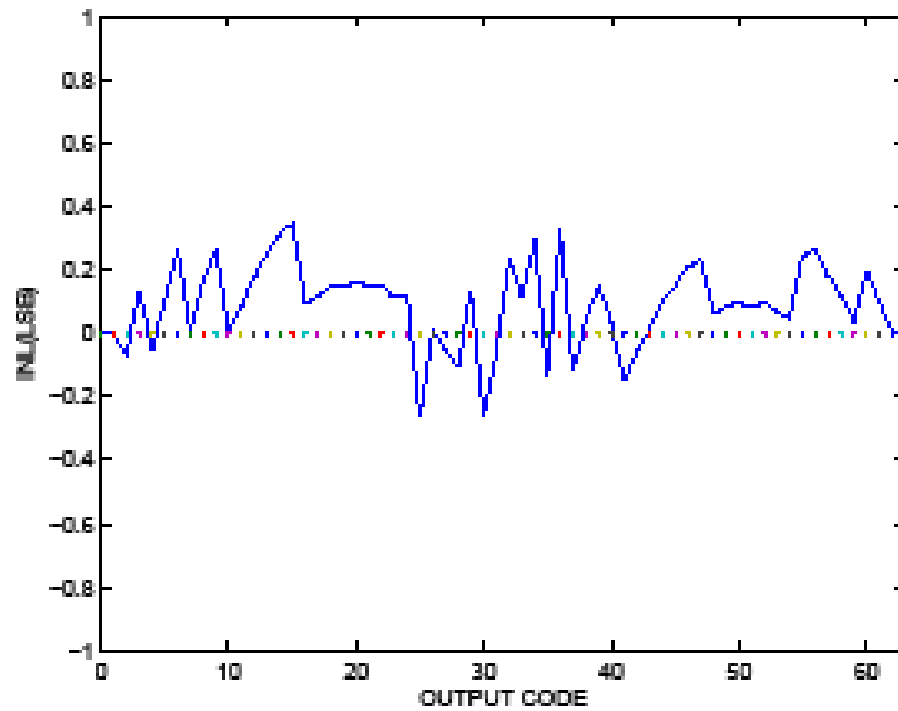


Figure 5.7. INL plot of the ADC.

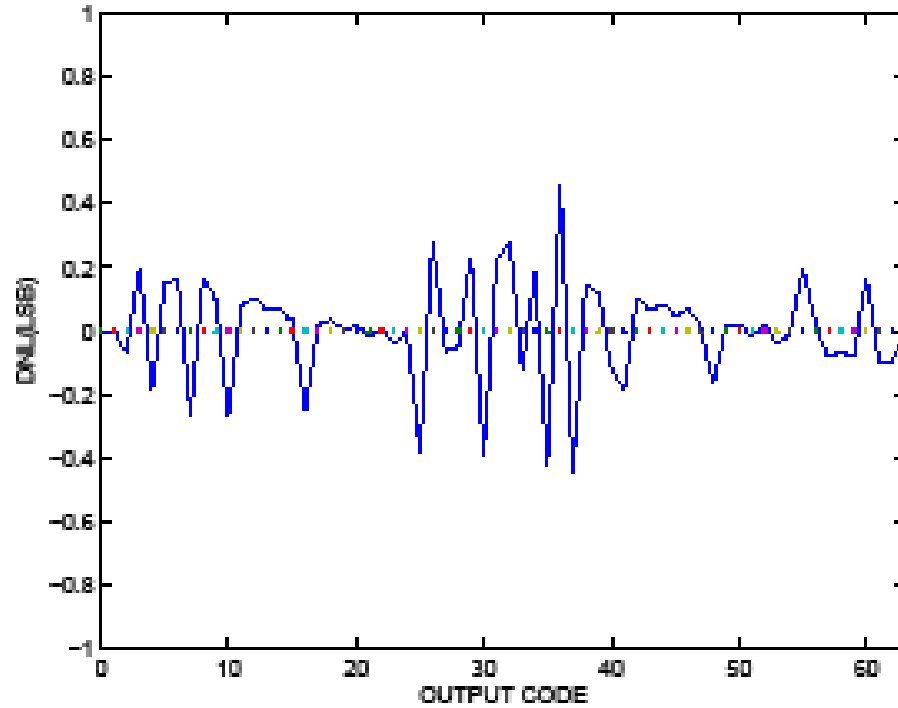


Figure 5.8. DNL plot of the ADC.

#### 5.1.4.3. Dynamic Characterization

SNDR is a good indicator of the overall dynamic performance of the ADC because it includes all the components which make up noise and distortion. The SNDR of an ADC is given by the following equation [3]:

$$(14) \quad \text{SNDR} = 20 \times \log_{10} \left( \frac{A_{\text{RMS}, \text{signal}}}{A_{\text{RMS}, \text{noise+harmonics}}} \right)$$

The fast fourier transformation (FFT) test was used to measure the SNDR. A 1 MHz sinusoidal input was fed to the ADC, and the FFT of the output was obtained. The SNDR was calculated from this FFT plot (shown in figure 5.9). The SNDR was found to be 31.7 dB.

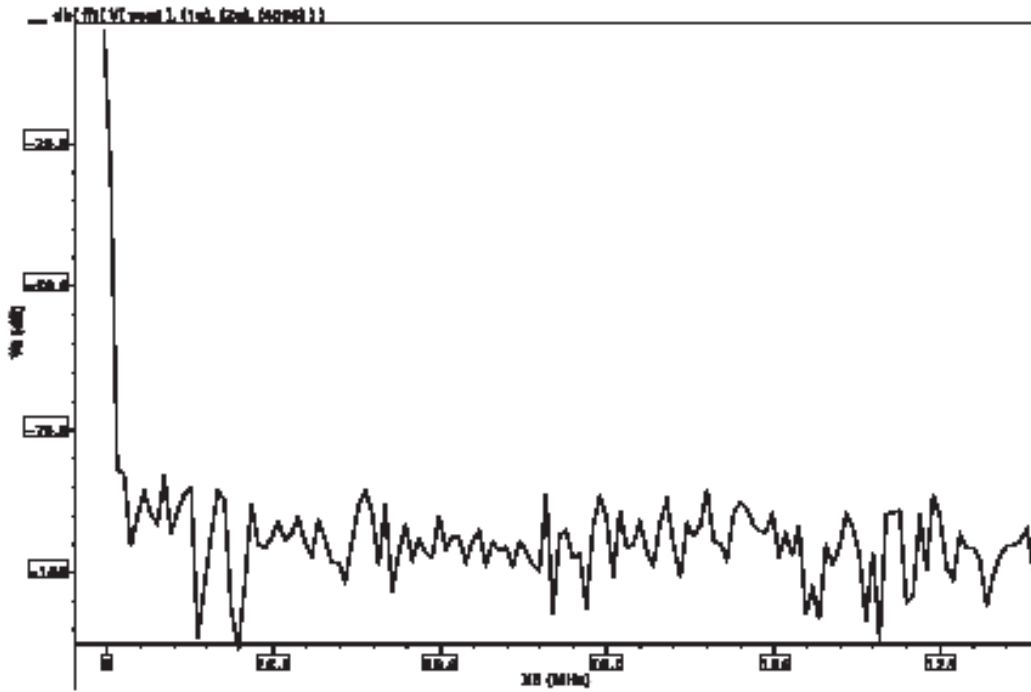


Figure 5.9. FFT plot of the ADC at a sinusoidal input frequency  $f_{in}$  of 1 MHz for SNDR calculation.

#### 5.1.4.4. Power Analysis

Power analysis of the ADC was performed with a capacitive load of 100 fF, which is a reasonable load for a 90 nm CMOS technology [87]. The ADC consumes a peak power of 5.794

milliwatts (mW) and an average power of 3.875 mW, which satisfies the lower bound on power consumption [118]. The component-wise power consumption is shown in Table 5.1.

Table 5.1. Componentwise Power Consumption of ADC

Component	Average Power (mW)
Comparator bank	3.68125 (95%)
1 of $n$ code generator	0.03875 (1%)
NOR ROM	0.155 (4%)
Total	3.875

It can be seen that the comparator bank consumes maximum power. A power-saving scheme can be used to turn off the unused TI comparators. The instantaneous power plot of the ADC, shown in figure 5.10, has a parabolic nature with peak power at the middle of the conversion process because most of the comparators are turned on at the middle voltage, (input voltage range)/2. The summary of the measured performance of the ADC is shown in table 5.2.

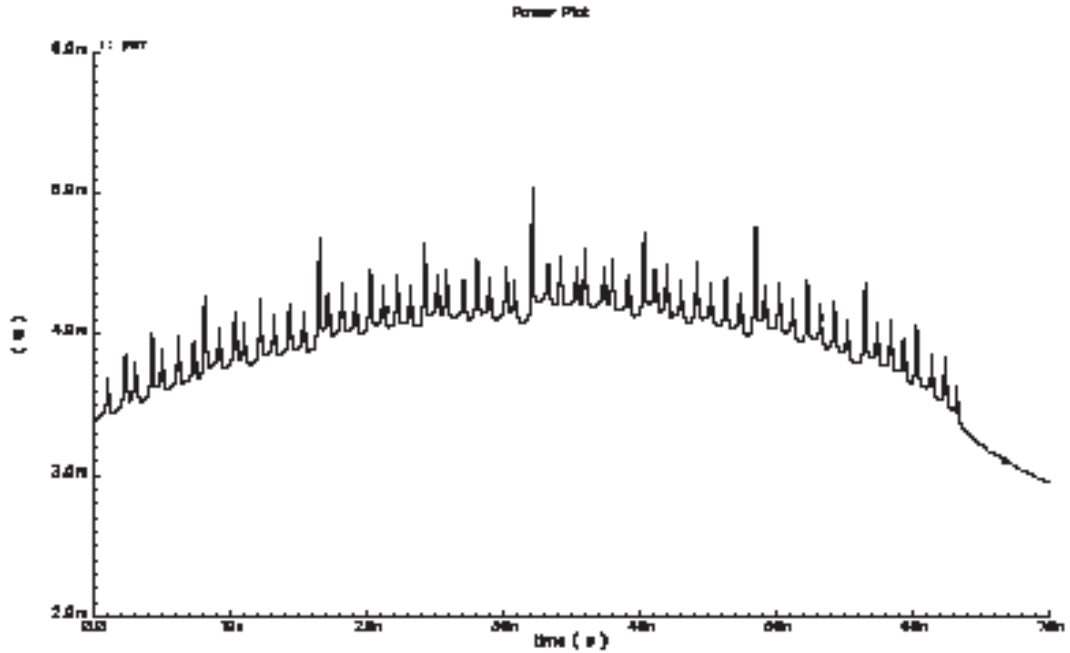


Figure 5.10. Instantaneous power plot of ADC with a load capacitance of 100 fF.

Table 5.2 ADC Performance with Nominal Supply and Threshold Voltages

Parameter	Value
Technology	90 nm CMOS 1P 9M
Resolution	6 bit
Supply voltage ( $V_{dd}$ )	1.2 V
Sampling rate	1 GS/s
INL	0.344 LSB
DNL	0.459 LSB
SNDR	31.7 dB @ $f_{in} = 1$ MHz
Peak power	5.794 mW@ 1.2V
Average power	3.875 mW@ 1.2V

#### 5.1.5. Transistor-Level Design and Characterization of the ADC at 45 nm Technology

The proposed ADC has also been built and characterized at 45 nm technology [45]. The block diagram of the ADC remains the same as described earlier in section 5.1.1. But the device sizes and the supply voltage change according to the technology used. The simulation and characterization details of ADC at 45 nm technology are discussed in this section. Simulated with the 45 nm predictive technology model, the results demonstrate  $INL < 0.5$  LSB,  $DNL < 0.8$  LSB and an SNDR of 31.9 dB. The TI technique is used with  $W_{pmos}/W_{nmos} < 1$  for many transistors in order to keep the power consumption as low as possible. It is also observed that the ADC consumes 45.42  $\mu$ W of peak power and 8.8  $\mu$ W of average power while it operates on a power supply voltage of 0.7 V. Because the process design kit for 45 nm technology is unavailable, the physical design has not been presented. The transistor level design at 45 nm is the same as at 90 nm technology. However, the transistor sizes are different. The differences are highlighted in the following subsections.

##### 5.1.5.1. Comparator Design

The methodology followed for choosing the comparator sizes was the same as for 90 nm technology. However, a suitable power supply of 0.7 V for 45 nm design [5] has been chosen. The channel length of transistors has been reduced accordingly. Using equation 9, the input voltage range was chosen to vary from 296.3 mV ( $V_{start}$ ) to 328.3 mV ( $V_{end}$ ). The  $V_{LSB}$  value is calculated to be 500  $\mu$ V (equation 10). Here,  $W_{nmos} = L_{nmos} = 90$  nm/90 nm and  $L_{pmos} = 90$  nm was kept constant throughout the design, while  $W_{pmos}$  was varied from 51 nm to 163 nm, to get 64 quantization levels, 500  $\mu$ V apart. The results are presented in table 5.3.

Table 5.3. Comparator Transistor Sizes for Input Voltage Range at 45 nm Technology

$V_{\text{switching}}$	$W_{\text{pmos}}/L_{\text{pmos}}$	$W_{\text{nmos}}/L_{\text{nmos}}$
296.3 mV ( $V_{\text{start}}$ )	51 nm/90nm	90 nm/90nm
327.8 mV ( $V_{\text{end}}$ )	163 nm/90 nm	90 nm/90 nm

#### 5.1.5.2. NOR ROM Design

The basic structure of NOR ROM remains the same as the 90 nm design. However, at 45 nm,  $W_{\text{pmos}}/L_{\text{pmos}} = 75 \text{ nm}/90 \text{ nm}$  and  $W_{\text{nmos}}/L_{\text{nmos}} = 90 \text{ nm}/90 \text{ nm}$  have been used.

#### 5.1.5.3. Functional Simulation

An instantaneous plot of the functional simulation of the ADC is shown in figure 5.11. Output codes from 0 to 63 are obtained with no missing codes. In this design, a maximum sampling speed of 100 MS/s has been obtained. This speed is sufficient as far as video applications are concerned [37].

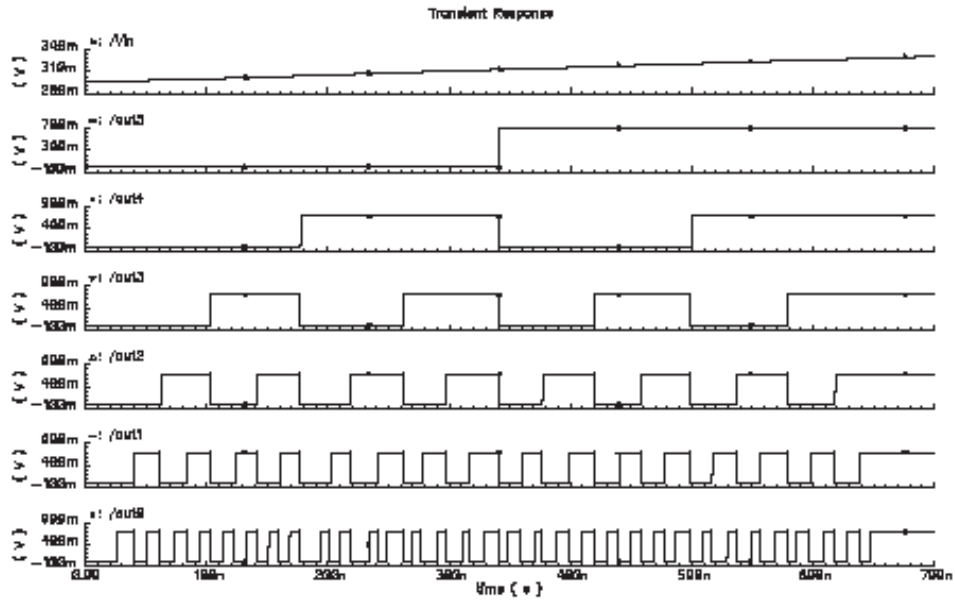


Figure 5.11. Functional simulation of the ADC at 45 nm mode.

#### 5.1.5.4. Characterization

The ADC has been characterized for INL, DNL, and SNDR. The peak and average power consumption have also been evaluated. The histogram method was used to calculate INL and DNL. The INL and DNL plots of the ADC are shown in figures 5.12 and 5.13, respectively. The ADC is observed to have maximum INL = 0.46 LSB and maximum DNL = 0.7 LSB. The FFT test was used to measure the SNDR. The SNDR plot of the ADC is shown in figure 5.14. The ADC is observed to have an SNDR = 31.9 dB for a 1 MHz sinusoidal input.

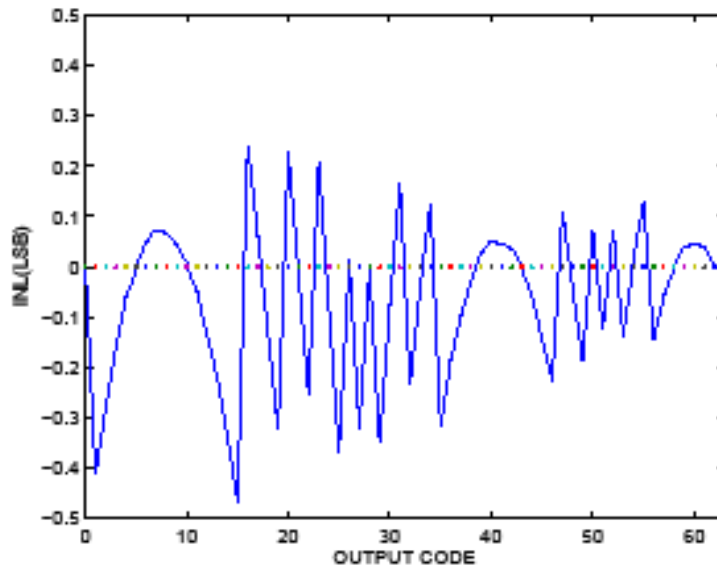


Figure 5.12. INL plot of the ADC at 45 nm node.

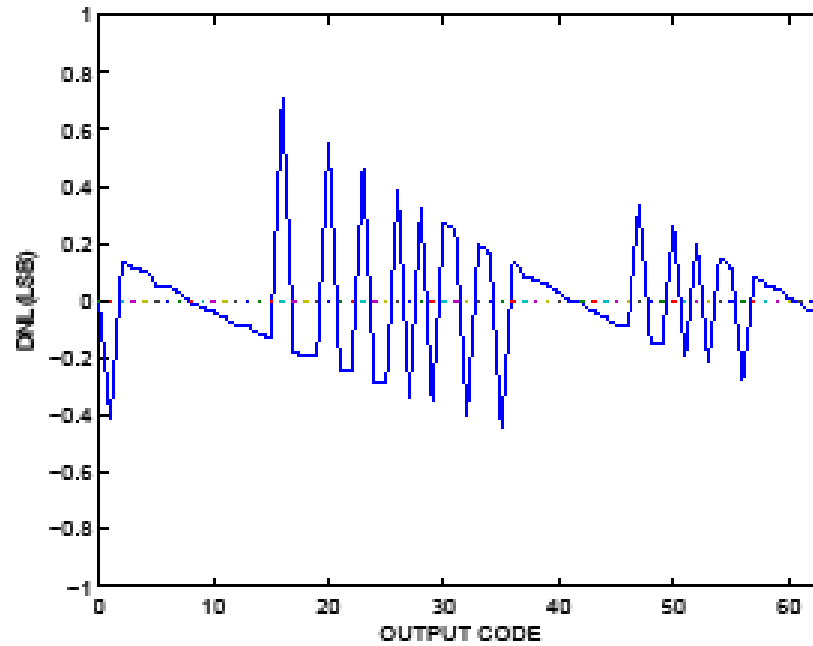


Figure 5.13. DNL plot of the ADC at 45 nm node.

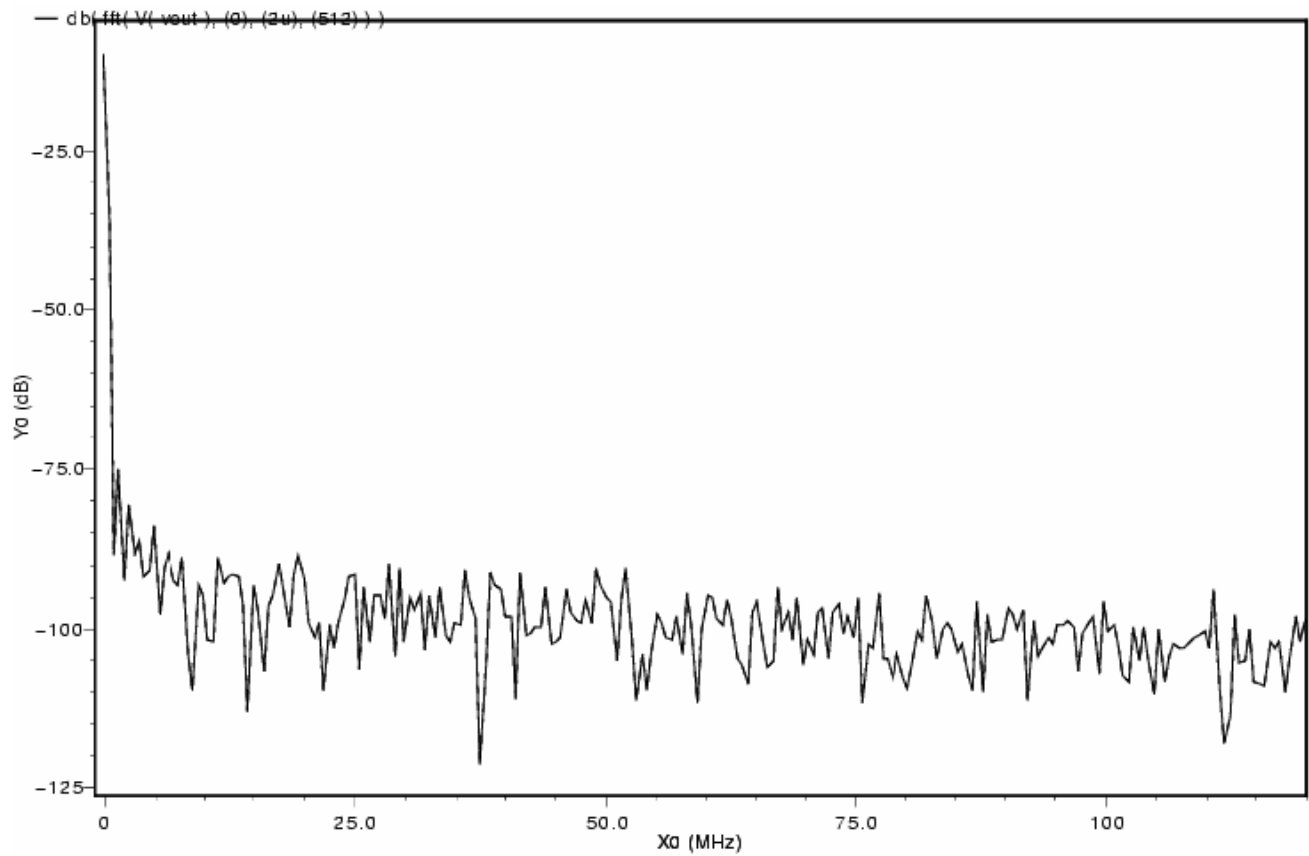


Figure 5.14. SNDR plot of ADC at 45 nm node.



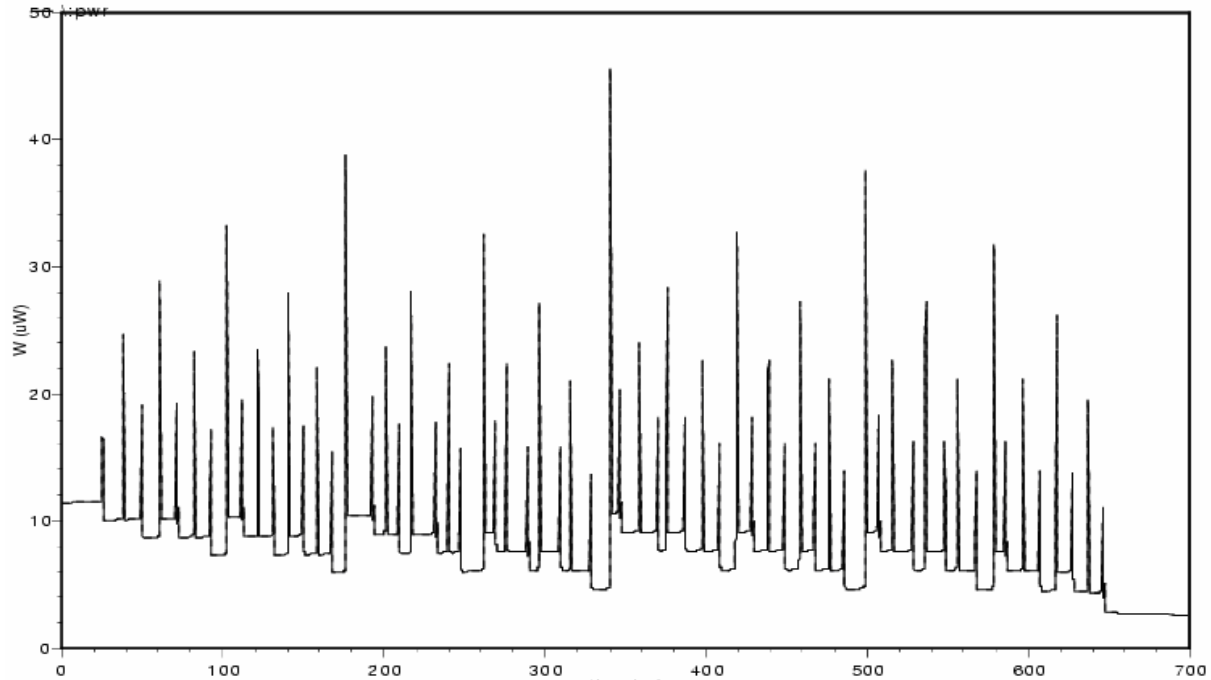


Figure 5.15. Instantaneous power plot of the ADC at 45 nm node.

The ADC was observed to consume peak power = 45.42  $\mu\text{W}$ , and average power = 8.8  $\mu\text{W}$ . The instantaneous power plot of the 45 nm ADC at no-load condition is shown in figure 5.15. The complete performance summary of the 45 ADC has been tabulated in table 5.4.

Table 5.4. ADC Performance at 45 nm Technology

Parameter	Value
Technology	45 nm PTM
Resolution	6 bit
Supply voltage ( $V_{dd}$ )	0.7 V
Sampling rate	100 MS/s
INL	0.46 LSB
DNL	0.7 LSB

(table continues)

Table 5.4 (*continued.*)

Parameter	Value
SNDR	31.9 dB @ $f_{in} = 1$ MHz
Peak Power	45.42 $\mu$ W@ 0.7V
Average Power	8.8 $\mu$ W@ 0.7V
Input Voltage Range	296.3 mV to 328.3 mV
$V_{LSB}$	500 $\mu$ V

## 5.2. Voltage-controlled Oscillator (VCO)

I have considered the current starved type of VCO, as other designs require large resistors and capacitors consuming a large silicon area. The design, as shown in figure 5.16, consists of two input stage transistors with high impedance, an odd numbered chain of inverters and two current source transistors per inverter. The current starved transistors limit the current flow to the inverter; i.e., they are starved for current. For determination of the oscillation frequency, we calculate the total capacitance ( $C_{TOT}$ ) on the drain of the inverter.

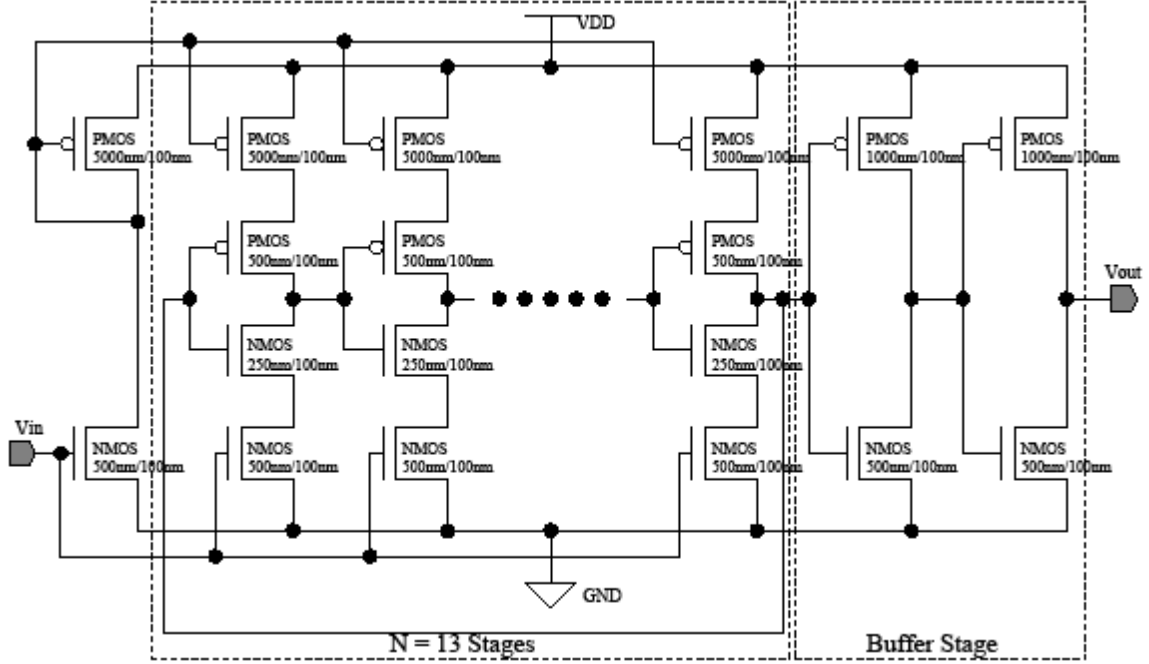


Figure 5.16. Nominal-case logical design of the VCO.

The  $C_{TOT}$  is given as the sum of the input ( $C_{in}$ ) and output ( $C_{out}$ ) capacitances of the inverter [10]:

$$\begin{aligned}
 C_{TOT} &= C_{out} + C_{in} \\
 &= C_{oxide} \times (W_p L_p + W_n L_n) \\
 &\quad + \frac{3}{2} \times C_{oxide} \times (W_p L_p + W_n L_n) \\
 &= \frac{5}{2} \times C_{oxide} \times (W_p L_p + W_n L_n)
 \end{aligned}
 \tag{15}$$

where  $C_{oxide}$  is the gate oxide capacitance per unit area,  $W_n$  and  $W_p$  are the widths, and  $L_n$  and  $L_p$  are the lengths of the inverter NMOS and PMOS transistors, respectively. The gate oxide capacitance per area  $C_{oxide}$  is calculated as

$$C_{oxide} = \frac{\epsilon_{r_{ox}} \times \epsilon_0}{T_{ox}}
 \tag{16}$$

where  $\epsilon_{r_{ox}}$  is the relative dielectric constant of  $\text{SiO}_2$ ,  $\epsilon_0$  is vacuum dielectric constant, and  $T_{ox}$  is the gate oxide thickness.

The total time required to charge and discharge the capacitance of an inverter stage is then given by:

$$(17) \quad T = C_{TOT} \times \left( \frac{V_{dd}}{I_D} \right)$$

The operating frequency of the VCO,  $f_0$ , can be determined by using this simple capacitance charging estimate (equation 17) [10], where  $V_{dd}$  is the supply voltage,  $I_D$  is the current flowing through the inverter, and  $N$  is the odd number of inverters in the VCO circuit. Hence, the oscillation frequency is determined by the number of inverters, size of the transistors in the circuit, and the current flowing through the inverter ( $I_D$ ), which is determined by the input voltage to the VCO.

The oscillation frequency is the functional specification for the design. The target oscillation frequency is kept at a minimum of 2 GHz for this design. To meet high-frequency requirements and an area optimal design, the number of stages ( $N$ ) is fixed to 13. Minimum-sized transistors have been used to design the inverters. The length is kept constant for all devices. Hence,  $L_n = L_p = 100$  nm,  $W_n = 250$  nm and  $W_p = 2 \times W_n = 500$  nm. Choosing minimum-width transistors also ensures an area optimal design. The  $C_{TOT}$  is calculated using these values. The  $I_D$  requirement is calculated by using equation 18 for the desired  $f_0$ .

$$(18) \quad f_0 = \frac{1}{N \times T} = \frac{I_D}{N \times C_{TOT} \times V_{dd}}$$

The current starved NMOS and PMOS devices are sized to provide the required current  $I_D$ . Thus, I obtained  $L_{ncs} = L_{pcs} = 100$  nm, and  $W_{ncs} = 500$  nm and  $W_{pcs} = 10 \times W_{ncs} = 5$   $\mu$ m, where  $W_{ncs}$  and  $W_{pcs}$  are the widths and  $L_{ncs}$  and  $L_{pcs}$  are the lengths of the current-starved NMOS and PMOS transistors, respectively. The minimum sizes of transistors needed for successful operation are obtained by using equations 15 and 18. However, it is extremely

difficult to find the optimum design by minimizing the phase noise and maximizing the tuning range simultaneously. To maximize the tuning range, it is necessary to minimize the parasitic capacitances and hence reduce the size of transistors. If the size becomes too small, however, flicker noise can dominate, which in turn would increase phase noise. The parasitic inductors (considered in this design) also exhibit nonlinear dependence on frequency, which makes the complexity of the problem worse.

### 5.3. Universal Voltage Level Converter (ULC)

The high-level representation of the ULC is shown in figure 5.17.

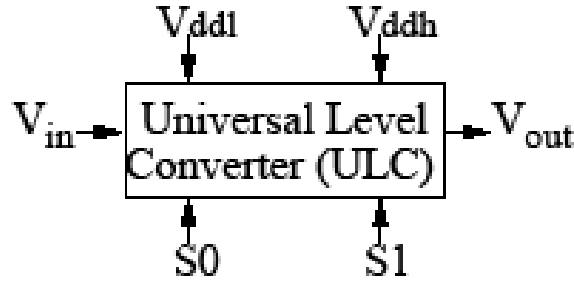


Figure 5.17. High level representation of the ULC.

It has an input voltage signal called  $V_{in}$ ; two control signals, S1 and S0; two supply voltages  $V_{ddl}$  ( $V_{dd}$ -low) and  $V_{ddh}$  ( $V_{dd}$ -high); and an output voltage signal,  $V_{out}$ . The state of control signals determines the functionality to be implemented and depending on that, the input voltage  $V_{in}$  is transformed to the output voltage  $V_{out}$ . Figure 5.18 gives a more detailed picture. To achieve programmability we have used multiplexers. First, the baseline design is discussed. The designs of the level-up and level-down converters are discussed separately. The area optimal design is then presented, followed by the power-delay optimal design.

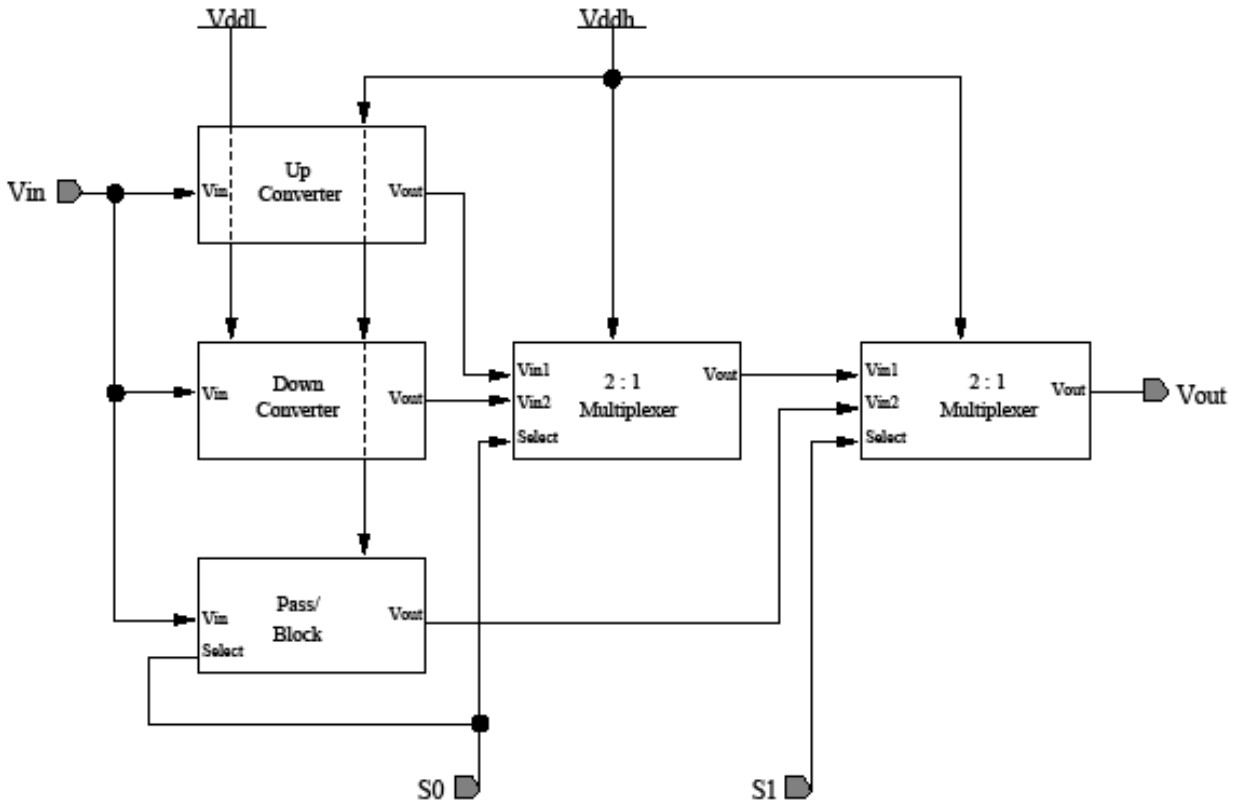


Figure 5.18. Schematic logical block diagram of the baseline (unoptimized) ULC.

### 5.3.1. Design of ULC

The baseline design of the proposed ULC is capable of performing four functions defined in table 5.5 blocking, passing, step-up conversion, and step-down conversion [81].

Table 5.5. Truth Table for Functionality of Baseline ULC Design

Select Signal		
S1	S0	Type of Operation
0	0	Block signal
0	1	Pass signal
1	0	Step-down
1	1	Step-up

The circuit has been designed with built-in programmability, and the number of transistors required to implement the circuit has been optimized. For circuit optimization, instead of using one 4:1 multiplexer or three 2:1 multiplexers, functionality is achieved by using two 2:1 multiplexers, thus saving on area overhead and resulting in lower power consumption, because of reduced transistor count.

#### 5.3.1.1. Level-up Conversion Circuit

The level-up converter is responsible for conversion of a signal at lower voltage ( $V_{ddl}$ ) level to a higher voltage ( $V_{ddh}$ ). I used a cross coupled level converting circuit (CCLC) (figure 19) to achieve the up conversion functionality.

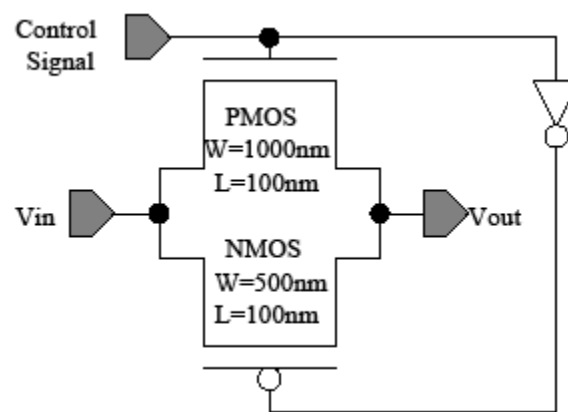


Figure 5.19. Circuit used for pass/block.

The CCLC circuit is an asynchronous level converter, which can be inserted anywhere in the circuit wherever level conversion is necessary. Because of this flexibility, CCLC is one of the designs most commonly used to suppress the direct current (DC) [57]. In this circuit, there are two cross-coupled PMOS transistors to form the circuit load. They act as a differential pair [57]. Thus, when the output at one side is pulled low, the opposite PMOS transistor will be turned on. The output on that side will be pulled high. Below the PMOS load, there are two NMOS transistors that are controlled by the input signal  $V_{in}$ . The NMOS transistors operate with a

reduced overdrive  $V_{ddl} - V_T$ , compared to the PMOS devices. They must be larger to be able to overpower the positive feedback [99]. The functional simulation result of the level-up converter is shown in figure 5.20.

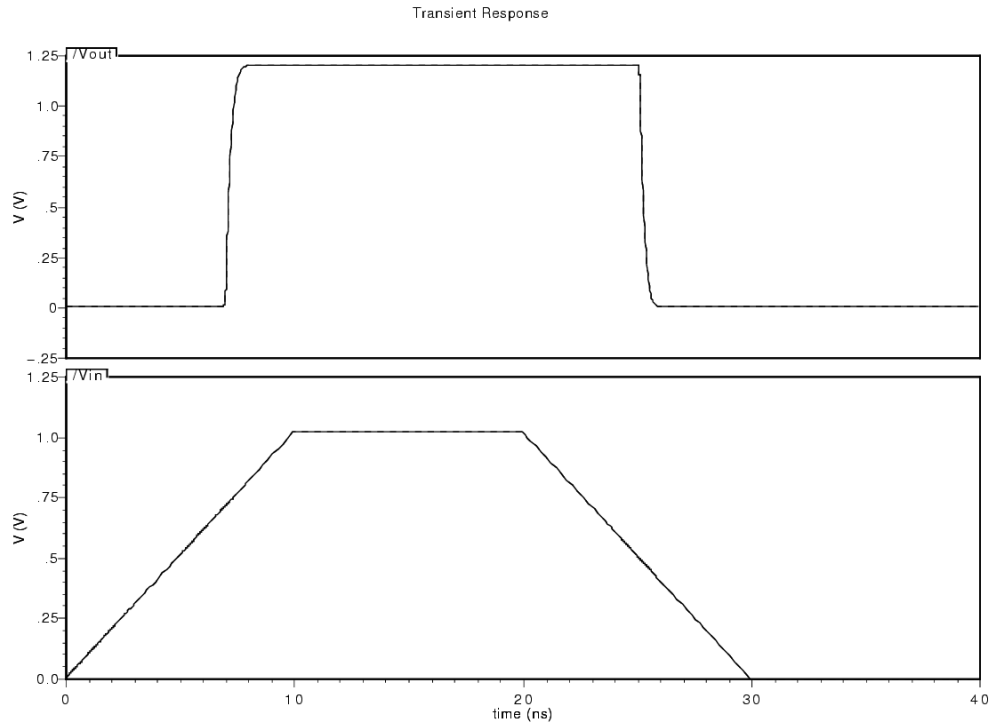


Figure 5.20. Functional simulation result of up-converter circuit.

#### 5.3.1.2. Level-down Converter

The level-down converter is responsible for converting the high voltage ( $V_{ddh}$ ) input signal to a lower voltage level ( $V_{ddl}$ ). A differential pair level converter which acts as a level-down converter circuit, is used for achieving the functionality of level-down conversion. Such a type of level converter finds applications in high-speed digital signal processing (DSP) chips [62] and low-voltage devices. It has high noise immunity against supply voltage bouncing [107]. The high noise immunity for a level converter circuit is very helpful because noise in the circuit is not considered when scaling down  $V_{dd}$  for low-power design [62]. This has impact on the



output quality of overall system. The circuit diagram for the differential input level-down converter is shown in figure 5.21.

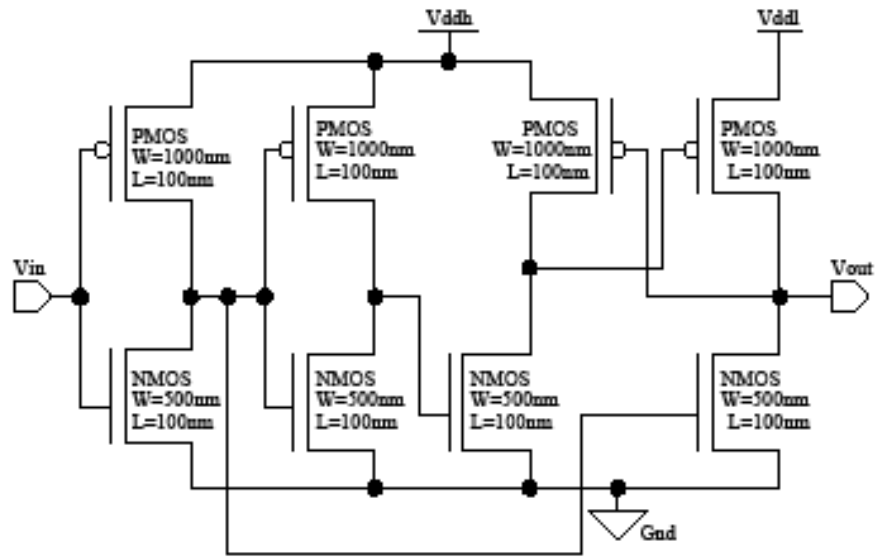


Figure 5.21. Down-converter circuit.

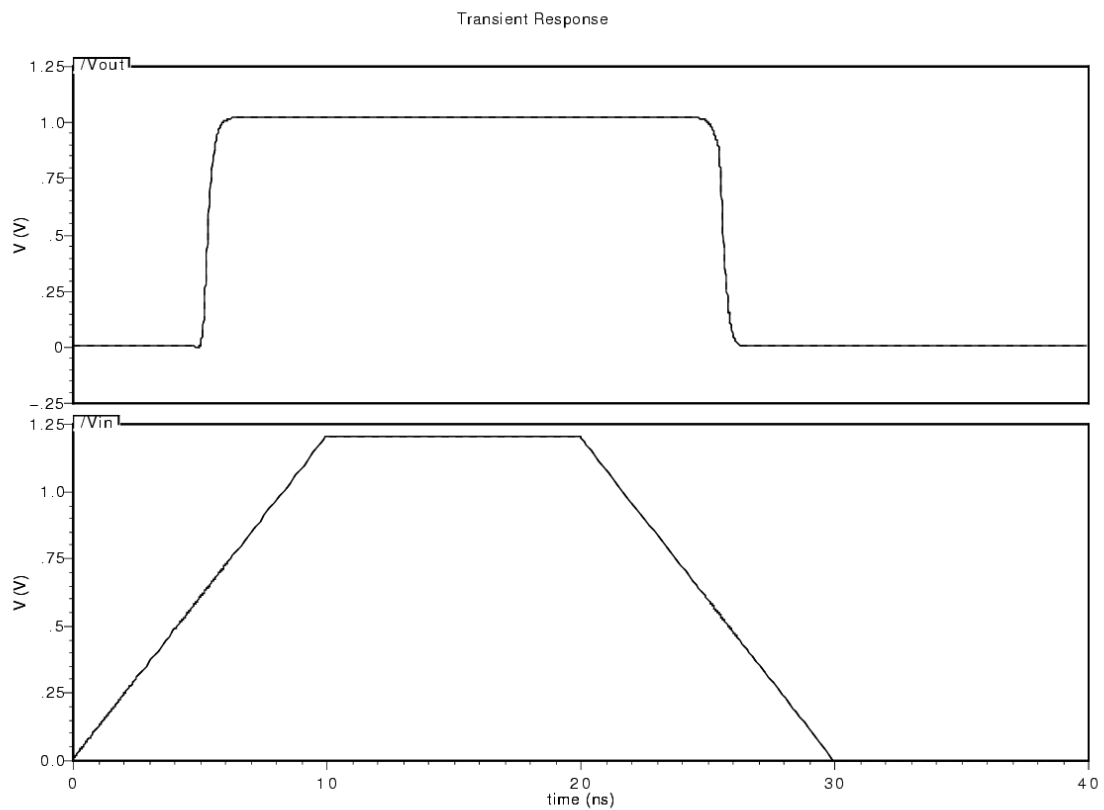


Figure 5.22. Functional simulation of down-converter circuit.

The circuit runs at a dual voltage that consists of  $V_{ddh}$  and  $V_{ddl}$ . The circuit consists of a cross-coupled PMOS pair, similar to the level-up converter circuit. The lower voltage signal,  $V_{ddl}$ , is applied at an inverter operating at  $V_{ddh}$ . The higher level of the signal is converted to a lower level at the output side. The functional simulation result of the level-down converter is shown in figure 5.22.

### 5.3.1.3. Pass/Block Circuit

This is another stage of circuit optimization. To minimize the transistor count of the circuit, I used the same circuit for passing and blocking with a control signal used for determining the functionality. The circuit diagram for the pass/block circuit is shown in figure 5.23. The pass/block circuit uses a transmission gate and an inverter to achieve the functionality of passing and blocking.

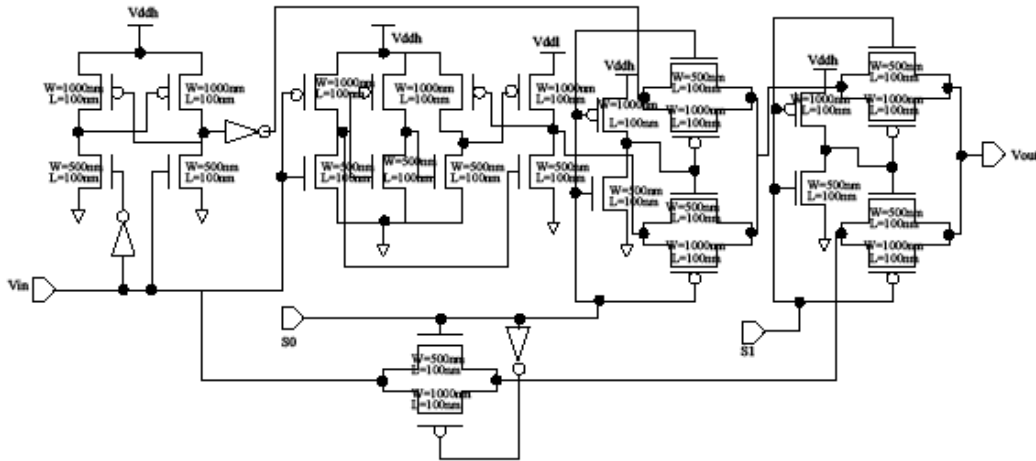


Figure 5.23. Transistor-level realization of the baseline design of the ULC with 32 transistors.

When the control signal = 0, it behaves as a pass circuit. When the control signal = 1, it behaves as a block circuit, as shown in figure 5.24.

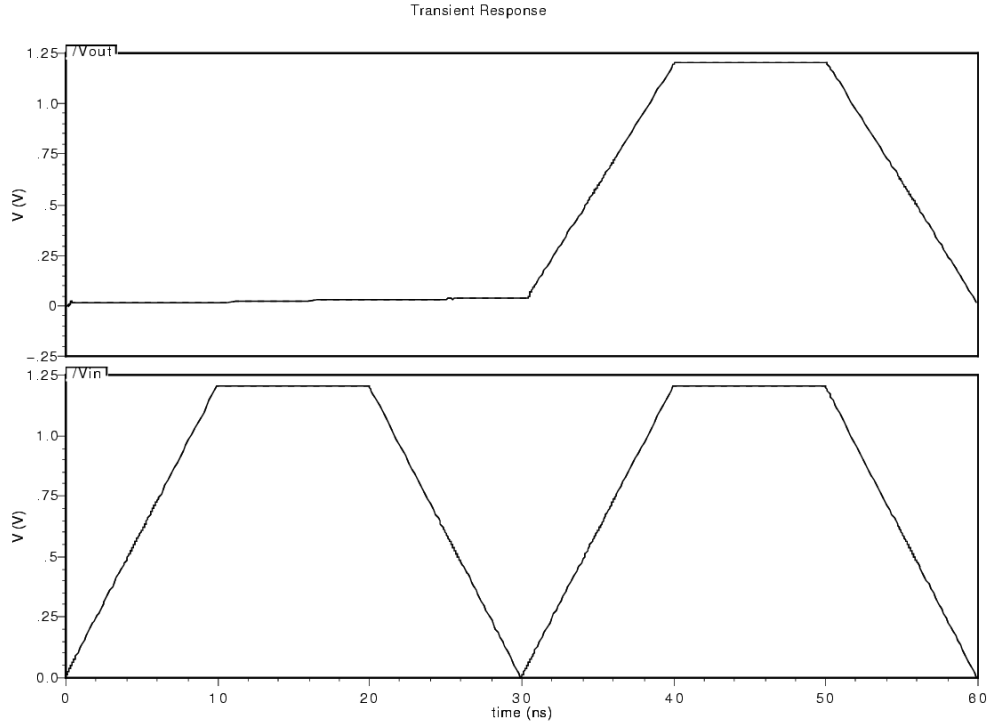


Figure 5.24. Functional simulation for pass/block circuit at  $V_{ddl} = 1.02$  V,  $V_{ddh} = 1.2$  V and load = 45 fF. (When the control signal = 0, the pass/block circuit behaves as a pass circuit; when the control signal = 1, it behaves as a block circuit. The bottom curve is input, and the top curve is output.)

The blocking functionality completely stops any kind of signal at the input side from appearing at the other side. This feature is very important when total isolation from the input signal is required for reduction of standby leakage power. Transmission gates are specifically used to build the pass/block circuit because of its ability to pass strong 0 or strong 1. This type of circuit is very handy when designing a data path or multiplexers.

#### 5.3.1.4. Baseline ULC Circuit

Figure 5.25 shows the transistor level circuit design of the ULC.

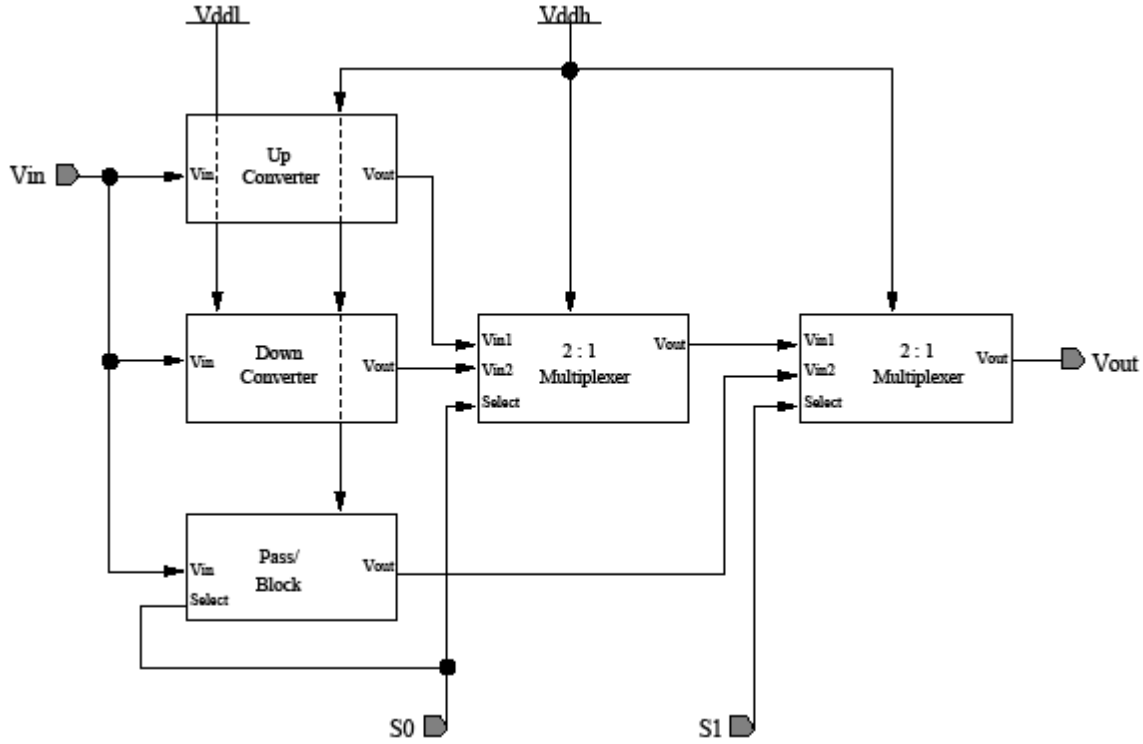


Figure 5.25. Transistor-level realization of the baseline design of the ULC with 32 transistors.

This design is achieved by stitching the individual subcircuits performing step-up conversion, step-down conversion, passing, and blocking. To achieve programmability, multiplexers are used. For circuit optimization, instead of using a 4:1 multiplexer, I achieved the functionality by using three 2:1 multiplexers. The average power consumption of the baseline design is 97.83  $\mu\text{W}$  (from simulation program with integrated circuit emphasis (SPICE) simulations).

#### 5.3.1.5. Area Optimal Design

To achieve the area optimal design of the ULC, I reduced the functionality of the ULC. Because pass function is not generally required, I removed the pass functionality. The design is shown in figure 5.26.

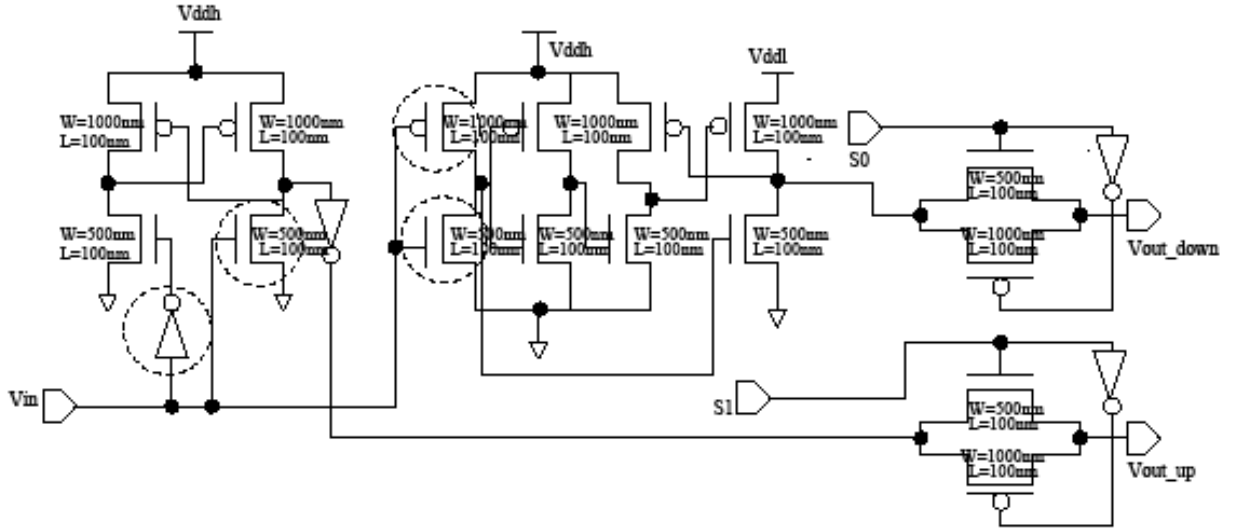


Figure 5.26. Transistor-level circuit realization of the area optimal ULC. (The power-hungry transistors, which are subjected to a dual  $T_{ox}$  technique for power minimization, are highlighted.)

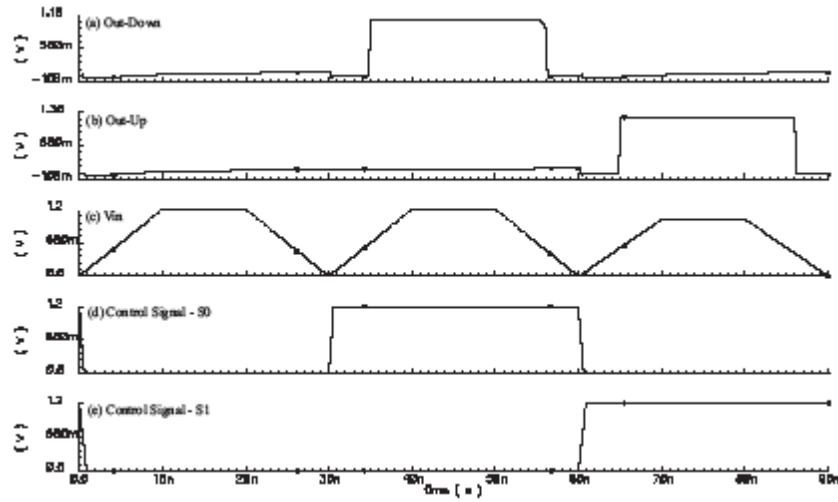


Figure 5.27. Functional simulation of the area optimal ULC. (This waveform verifies the truth table given in table 5.6. The sequence of operations is block, step-down, and step-up.)

In this design, a switch constructed using transmission gates is attached in front of the up level converter and down level converter. The output of the level converters can be controlled by the switches. I obtained an area optimal design by using two output nodes instead of one node. The number of transistors was also reduced to 24, eliminating 8 transistors from the baseline

design by using two 2:1 multiplexers instead of three 2:1 multiplexers. The functional simulation of the proposed ULC is shown in figure 5.27.

Hence, the area optimal design is capable of performing blocking, level-up conversion and level-down conversion. The above subcircuits, as well as the overall ULC circuit, are thoroughly tested for functionality. Then, they are exhaustively characterized through parametric, load, and power analysis.

#### 5.3.1.6. Physical Design for 90 nm Technology

The physical design of the ULC has been performed using a generic 90 nm salicide 1.2 V/2.5 V 1P 9M process design kit. In this layout, it was necessary to supply both  $V_{ddh}$  and  $V_{ddl}$  to the cell. The two supply rails ( $V_{ddl}$  and  $V_{ddh}$ ) travel side by side to provide the two voltages to the cell. Such a layout does not comply with the conventional application specific integrated circuits (ASIC) standard-cell power routing but is more robust [57]. The post-parasitic re-simulations matched with the schematic-level simulations. To improve the functional yield and reliability of the physical design, I followed design for manufacturability (DFM) methodologies. The use of additional vias has been made in the design wherever possible to make it more fault-tolerant [55]. The metal lines have been spread out wherever possible to control the capacitance and crosstalk between them [46].

#### 5.4. Active Pixel Sensor (APS)

An APS is an image sensor consisting of an IC containing an array of pixel sensors, each pixel containing a photodetector and an active amplifier. There are many types of active pixel sensors, including the complementary metal oxide semiconductor (CMOS) APS used most commonly in cell-phone cameras, web cameras, and some digital single-lens reflex cameras (DSLRs). Such an image sensor is produced by a CMOS process (and is hence also known as a

CMOS sensor) and has emerged as an alternative to charge-coupled device (CCD) imager sensors. The design of a three-transistor single pixel is presented as shown in figure 5.28 [50].

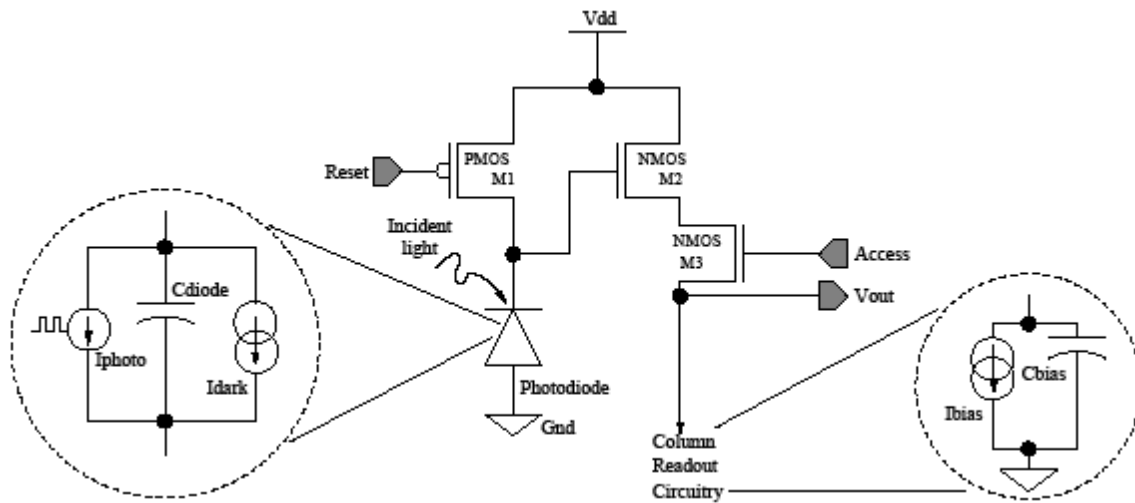


Figure 5.28. Circuit diagram of an APS.

The three transistors of the circuit are as follows: (i) M1: reset transistor, (ii) M2: source follower transistor, and (iii) M3: access transistor. A PMOS transistor (M1) has been used as the reset transistor because it results in a higher output voltage swing as compared to a conventional APS [31]. Transistor sizes are chosen carefully for enough current, source follower gain, and isolation of source follower output from the pixel output. In addition, the transistor sizes should be as small as possible for the maximum photodiode/pixel ratio ("fill factor"), when considering the physical design in silicon. Table 5.6 shows the sizes chosen for the transistors of the APS.

Table 5.6. Transistor Sizes

Transistor Name	Size (W:L for 32 nm CMOS)
M1	160 nm : 32 nm
M2	320 nm : 32 nm
M3	240 nm : 32 nm

The most important component of the APS, the photodiode, is modeled as a pulsed current source representing the photocurrent ( $I_{photo} = 100 \text{ nA to } 350 \text{ nA}$ ) in parallel with a capacitor representing the diode capacitance ( $C_{diode} = 20 \text{ fF}$ ) and a direct current (DC) current source representing the dark current ( $I_{dark} = 2 \text{ fA}$ ) [125].  $I_{bias} = 500 \text{ nA}$  and  $C_{bias} = 1 \text{ pF}$  are assigned to the biasing circuitry. The values are selected to be consistent with the 32 nm technology node. Higher bias current ( $I_{bias}$ ) ensures a smaller readout time.

A typical two-dimensional array of  $M \times N$  pixels is organized into  $M$  rows and  $N$  columns. Pixels in a given row share reset lines, so that a whole row is reset at a time. The select lines of each pixel in a row are tied together. The outputs of each pixel in any given column are tied together. Since only one row at a time is selected, no competition for the output line occurs. Further amplifier circuitry is typically on a column basis. Figure 5.29 shows the block diagram of an  $8 \times 8$  APS array implemented by using 64 single pixels of the type shown in figure 5.30.

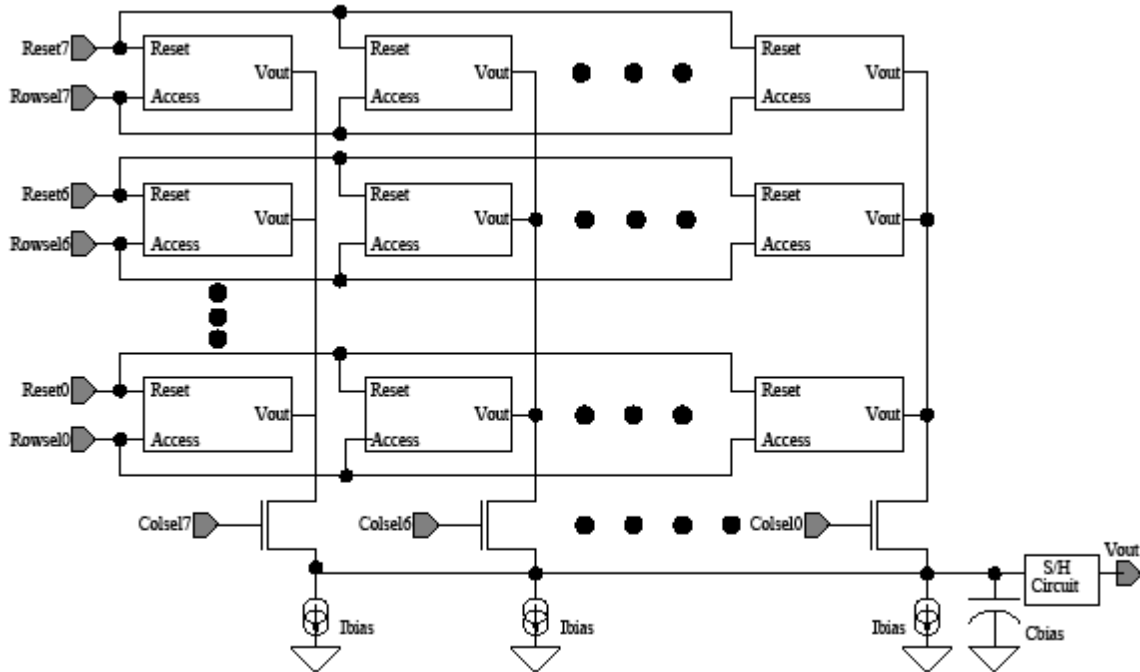


Figure 5.29. An  $8 \times 8$  APS array constructed by using a collection of APS.



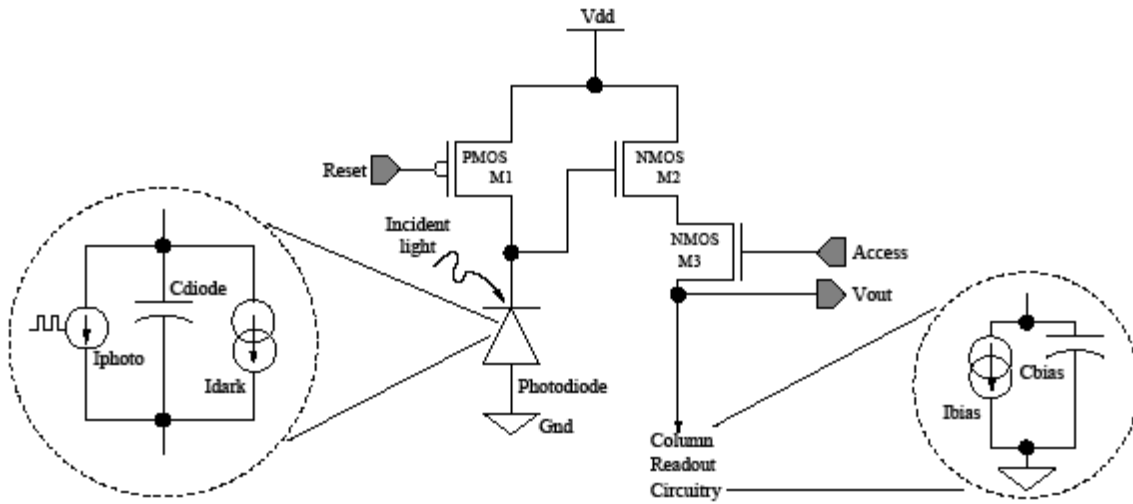


Figure 5.30. Circuit diagram of an APS.

The array is accessed pixel-wise. The functional simulation results of the array are shown in figure 5.31 for high illumination photocurrent. An output voltage swing of 428 mV can be observed. The result is obtained from transient analysis of the APS array.

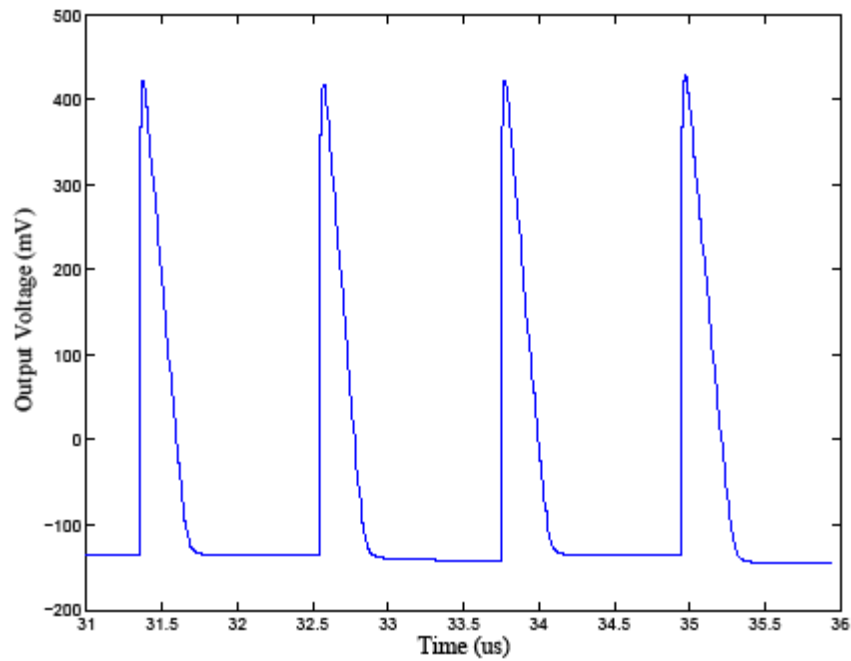


Figure 5.31. Circuit simulation of the  $8 \times 8$  APS array.

#### 5.4.1. Models for the Figures of Merit of the APS array

I now discuss the baseline characterization of the APS array. The models used for characterizing the various figures of merit are presented. The array has been characterized for the following figures of merit or attributes: (i) average power dissipation  $P_{APS}$ , (ii) capture time  $C_{time}$ , (iii) output voltage swing  $V_{swing}$ , and (iv) dynamic range DR. For measuring  $P_{APS}$ , we have used the models provided in chapter 2.

##### 5.4.1.1. Output Voltage Swing

The output voltage swing ( $V_{swing}$ ) of array is defined as the maximum swing achieved by the output voltage. It is an important figure of merit because it affects the dynamic range (DR) of the array. From figure 5.32, I measured baseline  $V_{swing}$  as 428 mV. This value is 47.6% of  $V_{dd}$ , which is in the acceptable range (chapter 3).

##### 5.4.1.2. Dynamic Range (DR)

The DR of array can be formulated as follows [125]:

$$(19) \quad DR = 20 \times \log_{10} \left[ \frac{\left( \frac{q \times Q_{\max}}{t_{\text{int}}} \right) - I_{\text{dark}}}{\left( \frac{q}{t_{\text{int}}} \right) \sqrt{\sigma_{\text{total}}^2 + \left( \frac{I_{\text{dark}} \times t_{\text{int}}}{q} \right)}} \right]$$

where

$$(20) \quad Q_{\max} = \left( \frac{C_{\text{diode}} \times V_{\text{swing}}}{q} \right)$$

where  $\sigma_{\text{total}}^2$  = variance of noise because of readout and reset (in electron<sup>2</sup>),  $t_{\text{int}}$  = integration period. The baseline DR of the APS for 32 nm CMOS technology is calculated to be 59.47 dB.

### 5.4.1.3. Capture Time

The input to each pixel in the array has been modeled in the form of a pulse shaped photocurrent  $I_{photo}$ . The capture time is defined as the delay from the 50% level of the input swing ( $I_{photo}$ ) to the 50% level of the output voltage ( $V_{out}$ ). For measurement of capture time ( $C_{time}$ ) of the array, I considered the pixel in the middle of the array because it suffers the maximum loading. Thus, it gives us the maximum  $C_{time}$  of the array. The APS array has a baseline  $C_{time}$  of 5.65  $\mu$ s for 32 nm CMOS. The APS array baseline results are in table 5.7.

Table 5.7. Baseline Characterization of APS Array

Parameter	Value
Technology	32 nm PTM
Supply voltage ( $V_{dd}$ )	0.9 V
$P_{APS}$	16.32 $\mu$ W
$C_{time}$	5.65 $\mu$ s
$V_{swing}$	428 mV
DR	59.47 dB

## CHAPTER 6

### PROCESS VARIATION ANALYSIS AND DESIGN OPTIMIZATION

In this chapter, I provide the implementation details of the optimization methodologies discussed in chapter 4. Each of the mixed-signal circuits has been subjected to an optimization approach to verify its process variation tolerance.

#### 6.1. Analog-to-digital Converter (ADC)

The 90 nm ADC discussed in chapter 5 was subjected to a corner-based methodology described in this section. First, the results for process and supply variation are presented, followed by temperature variation characterization of the ADC.

##### 6.1.1. Process and Supply Variation

Process and supply variation in an ADC is a critical issue. Whereas process variation is a static problem, the supply variation is a dynamic problem [47]. The ADC was tested for the effects of threshold voltage mismatch and supply voltage variation on the integral nonlinearity (INL) and differential nonlinearity (DNL). It is assumed that  $V_{switching}$  is not sensitive to variation in the length of the transistors ( $L_{pmos}$ ,  $L_{nmos}$ ), because the effective switching resistances of transistors are independent of their lengths (equation 8). Hence, the effect that is due to device mismatch can be modeled to some degree by the effect of threshold voltage mismatch.

The results revealed that while the INL and DNL values were within control, a shift occurred in the input voltage range. Consequently, the  $V_{LSB}$  value also changed. To overcome this shift, one may add a programmable preamplifier to the input signal of the ADC, thereby adjusting the signal offset and amplitude [32], or DSP may be performed on the ADC, which is suitable for system-on-a-chip (SoC) applications, because an on-chip processor might be present.

A corner-based process variation methodology was used for testing the ADC. The methodology is shown in figure 6.1.

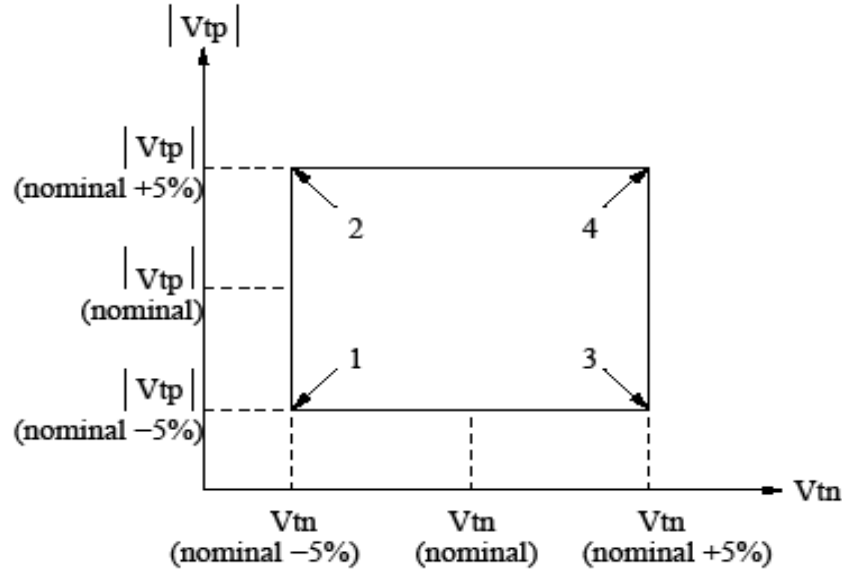


Figure 6.1. Corner methodology used for the process variation study.

The n-type metal oxide semiconductor (NMOS) threshold voltage ( $V_{tnmos}$ ) and the p-type metal oxide semiconductor (PMOS) threshold voltage ( $V_{tpmos}$ ) were varied by  $\pm 5\%$  from their nominal values specified in the process design kit (PDK), and the INL, DNL, and input voltage range values were recorded. The results are summarized in table 6.1.

Table 6.1 Process Variation Results

PMOS threshold voltage ( $V_{tp}$ ), NMOS threshold voltage ( $V_{tn}$ )	Input Voltage Range (mV)	$V_{LSB}$ (mV)	INL (LSB)	DNL (LSB)
$V_{tp}$ (nominal), $V_{tn}$ (nominal)	493-557	1	0.344	0.459
$V_{tp}$ (-5%), $V_{tn}$ (-5%) Corner 1	491-556	1.015625	0.345	0.477
$V_{tp}$ (+5%), $V_{tn}$ (-5%) Corner 2	501-566	1.015625	0.38	0.479
$V_{tp}$ (-5%), $V_{tn}$ (+5%) Corner 3	500-564	1	0.36	0.485
$V_{tp}$ (+5%), $V_{tn}$ (+5%) Corner 4	495-557	0.96875	0.333	0.46

The INL shows a variation from +0.2% to +10.5% and the DNL shows a variation from +2.2% to +5.7%. For the supply voltage variation, the nominal supply voltage (1.2 V) was varied by  $\pm 10\%$ , and the INL, DNL, and input voltage range values were recorded, as shown in table 6.2.

Table 6.2. Supply Voltage Variation Results

$V_{dd}$ (V)	Input Voltage Range (mV)	$V_{LSB}$ (mV)	INL(LSB)	DNL(LSB)
1.08V (-10%)	448-500	0.8125	0.359	0.467
1.2V (nominal)	493-557	1	0.344	0.459
1.32V (+10%)	537-614	1.203	0.339	0.481

The INL shows a variation of  $-1\%$  to  $+4\%$ , and the DNL shows a variation of  $+1.8\%$  to  $+4.8\%$ .

It can be observed that the INL and DNL values are satisfactory [INL, DNL < 0.5 least significant bit (LSB)]. Hence, the ADC is process and supply variation tolerant.

#### 6.1.2. Temperature Variation Characterization

If the temperature of a device is changed, the mobility, the channel length, and the threshold voltage of the device are affected [10]. Thus, it is essential to consider the effect of temperature variation on ADC performance. The ADC was subjected to an extensive range of temperature variation on ADC performance. The ADC was subjected to an extensive range of temperature ( $-40^{\circ}\text{C}$  to  $90^{\circ}\text{C}$ ), and the INL and DNL values were recorded. The  $27^{\circ}\text{C}$  was treated as the nominal temperature. The INL showed less sensitivity to temperature variations than the DNL. Efforts are going on to make the DNL robust to temperature variation. A shift was also observed in the input voltage range, leading to a decrease (at  $-40^{\circ}\text{C}$ ) or increase (at  $90^{\circ}\text{C}$ ) in  $V_{LSB}$  value. The results are shown in table 6.3. This shift can be compensated for by subjecting the input signal to preamplification before feeding it to the ADC.

Table 6.3. Effect of Temperature Variation

Temperature (°C)	Input Voltage Range (mV)	$V_{LSB}$ (mV)	INL (LSB)	DNL (LSB)
-40	484.5-544.5	0.9375	0.30	1
27 (nominal)	493-557	1	0.344	0.459
90	503.5-570.5	1.046875	0.67	1

## 6.2. Voltage-controlled Oscillator (VCO)

This section demonstrates how the oscillation frequency discrepancy arising because of parasitics and process variation have been overcome with minimal modification of the physical design. The parasitic-aware optimization is discussed first, followed by the parasitic- and process-variation-aware optimization.

### 6.2.1. Parasitic-aware Optimization

For the optimization, first a baseline logical design was performed with the design equations presented in chapter 5. The physical design was prepared with that baseline design. After full extraction (resistance, capacitance, inductance, self-inductance) (RCLK), a 25% degradation in the oscillation frequency was observed between the logical and the physical designs (figure 6.2):

- Target oscillation frequency  $f_0 = 2$  GHz
- Logical design oscillation frequency  $f_{0\log} = 1.95$  GHz
- Physical design oscillation frequency  $f_{0\text{phys}} = 1.56$  GHz

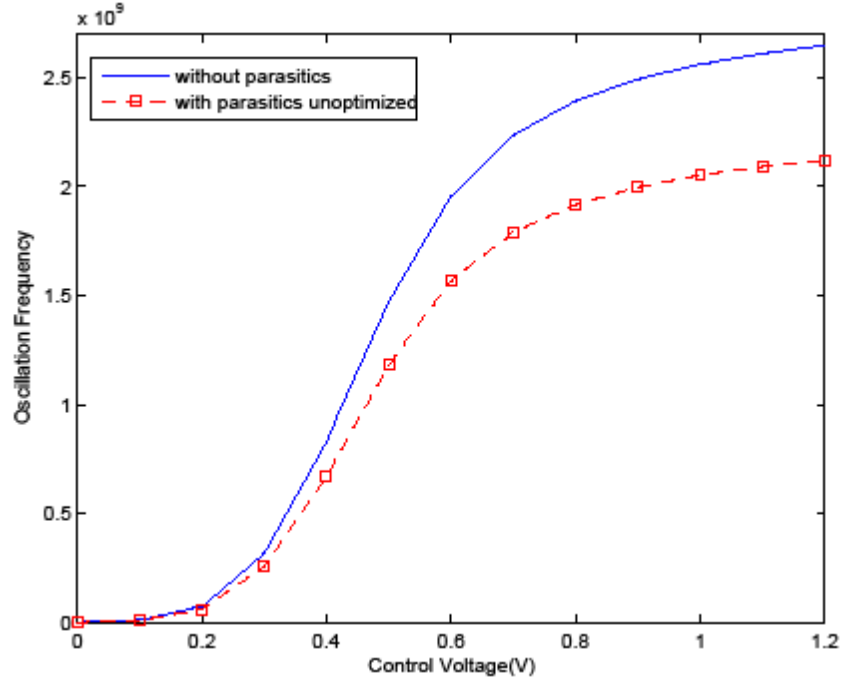


Figure 6.2. Comparison of frequency-voltage characteristics of the logical design and parasitic extracted physical design of the VCO.

The parasitic-aware netlist, generated from the first layout (including parasitics), was then subjected to an optimization loop using an analog simulator and a conjugate gradient optimization technique (algorithm 1) in which the design variables were varied in order to achieve the required performance criterion (oscillation frequency). The set of design variables used for optimization were the following:

- Widths of NMOS devices in the inverter ( $W_n$ )
- Widths of PMOS devices in the inverter ( $W_p$ )
- Widths of NMOS devices in the current-starved circuitry ( $W_{ncs}$ )
- Widths of PMOS devices in the current-starved circuitry ( $W_{pcs}$ )

Since the channel length ( $L$ ) of the transistor more effectively controls the performance (frequency  $\propto 1/L^2$ ), I kept the channel lengths constant ( $L_n = L_p = L_{ncs} = L_{pcs} = 100$  nm) and varied the channel widths. These are the constraints for the design methodology. My objective



function was a target oscillation frequency of 2 GHz. The stopping criterion was within 2% of target. The final optimal values of the design variables are given in table 6.4.

Table 6.4. Final Values of the Design Variables fro Parasitic-aware Design

Variable	Varied from	Varied to	Optimal value
$W_n$	200 nm	500 nm	220 nm
$W_p$	400 nm	1000 nm	440 nm
$W_{ncs}$	500 nm	2 $\mu$ m	945 nm
$W_{pcs}$	5 $\mu$ m	20 $\mu$ m	9.45 $\mu$ m

The physical design of the VCO was carried out with these parameter values, and the following results were obtained:

- Target oscillation frequency  $f_0 = 2$  GHz
- Logical design oscillation frequency  $f_{0\log} = 1.95$  GHz
- Parasitic aware physical design oscillation frequency  $f_{0\text{opt}} = 1.98$  GHz

I was able to obtain convergence with only one iteration in the layout. The final optimized layout for the parasitic-aware VCO is in figure 6.3. Figure 6.4 shows the frequency-voltage transfer curves for the logical and the physical design after parasitic-aware optimization. The optimized curve closely follows the logical design curve. The measured performance of the VCO is given in table 6.5.

Table 6.5. Measured Performance of the Parasitic-aware VCO

Parameter	Value
Technology	90 nm CMOS 1P 9M
Supply voltage ( $V_{dd}$ )	1.2 V
Oscillation frequency	1.98 GHz
Number of design variables	4 ( $W_n, W_p, W_{ncs}, W_{pcs}$ )
Number of objectives	1 ( $f_0 \geq 2$ GHz)

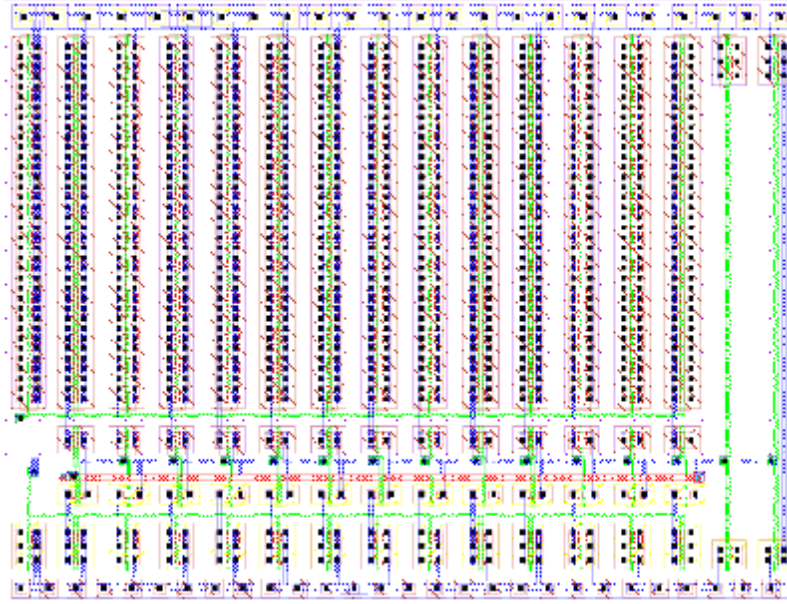


Figure 6.3. Final layout of the VCO optimized for parasitic-aware design flow.

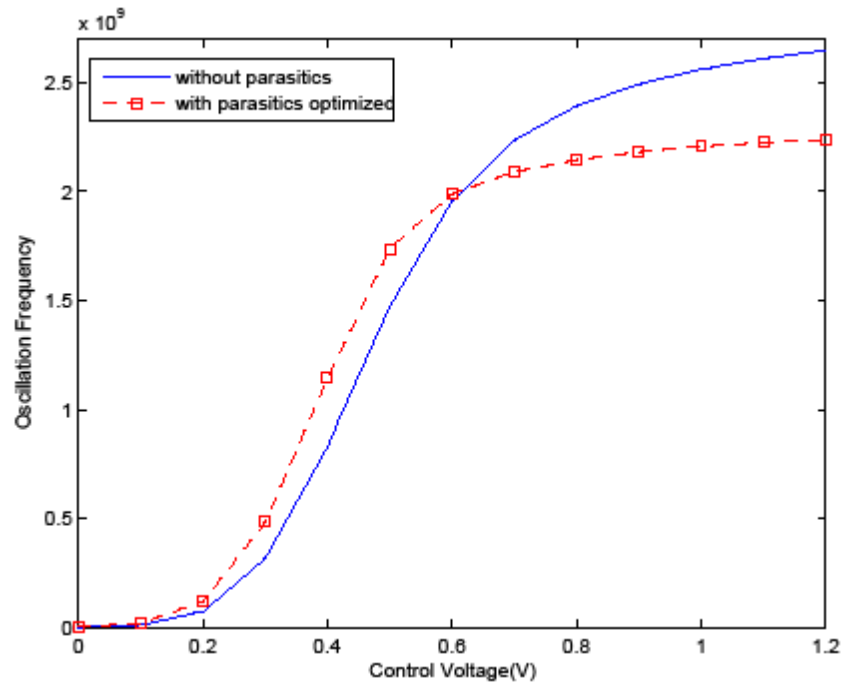


Figure 6.4. Frequency-voltage transfer characteristics of the VCO optimized for design flow accounting for parasitics.

### 6.2.2. Process Variation Study

It can be seen from equations 16 and 18 that the oscillation frequency shows strong dependence on  $V_{DD}$ , threshold voltage of the CMOS  $V_T$  ( $I_D$  depends on  $V_T$ ), and gate oxide thickness  $T_{ox}$ . Hence, any variation in these process ( $V_T$ ,  $T_{ox}$ ) parameters and supply ( $V_{dd}$ ) would lead to a degradation in the oscillation frequency. Process variations can be modeled by using technology files or analytical formulas. Technology files are process-dependent and can be created from the information provided by foundries. In this work, a technology file based on a general 90 nm process design kit was used. For the VCO, the following parameters were identified for process variation:

- Supply voltage ( $V_{dd}$ )
- Threshold voltage of NMOS transistors ( $V_{Tnmos}$ )
- Threshold voltage of PMOS transistors ( $V_{Tpmos}$ )
- Gate oxide thickness of NMOS transistors ( $T_{oxnmos}$ )
- Gate oxide thickness of PMOS transistors ( $T_{oxpmos}$ )

In this section, I present the results of statistical process variation carried out on the parasitic extracted netlist of the VCO. Statistical variations in the process parameters, each assumed to be Gaussian, were explicitly taken into account by using Monte Carlo simulations, and the effect on oscillation frequency was observed [49]. In particular, 5 different cases were recorded.

#### 6.2.2.1. Only $V_{DD}$ Variation

Statistical distribution for  $V_{DD}$  was taken as Gaussian to obtain results in a realistic scenario, with a standard deviation  $\sigma = 10\%$ . Monte Carlo simulations were run for  $N = 100$  runs. The oscillation frequency shows a Gaussian distribution in figure 6.5.

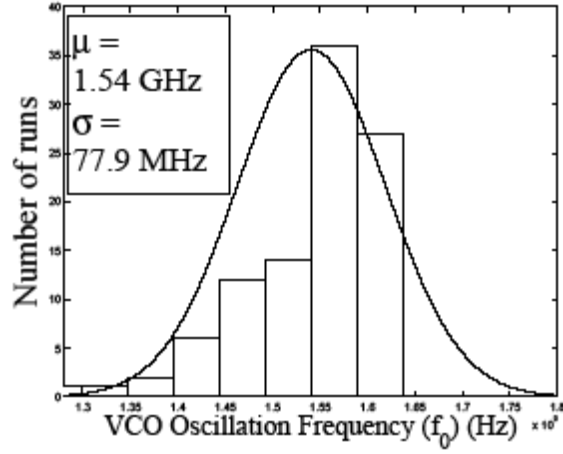


Figure 6.5. Statistical  $V_{dd}$  variation.

#### 6.2.2.2. Only $V_{Tnmos}$ Variation

$V_{Tnmos}$  had a Gaussian statistical distribution with a standard deviation  $\sigma = 10\%$ . One hundred Monte Carlo runs were performed. The oscillation frequency shows a Gaussian distribution in figure 6.6.

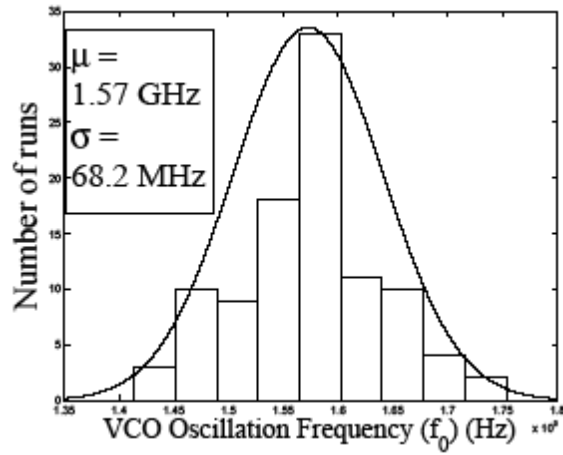


Figure 6.6. Statistical  $V_{Tnmos}$  variation.

#### 6.2.2.3. Only $V_{Tpms}$ Variation

$V_{Tnmos}$  was given a Gaussian statistical distribution with a standard deviation  $\sigma = 10\%$ . One hundred Monte Carlo simulations were performed. The oscillation frequency shows a Gaussian distribution in figure 6.7.

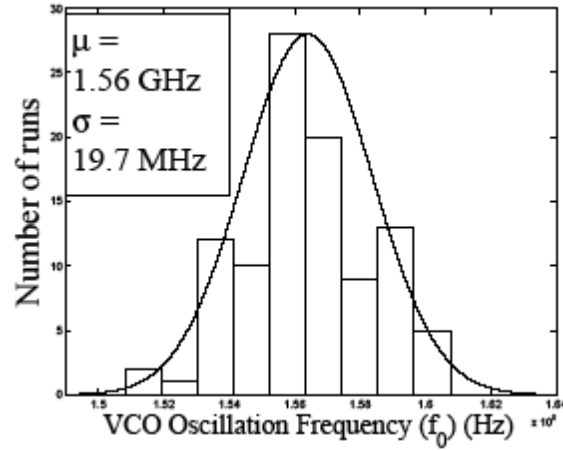


Figure 6.7. Statistical  $V_{T_{pmos}}$  variation.

#### 6.2.2.4. Simultaneous $T_{oxnmos}$ and $T_{oxpmos}$ Variation

In a typical complementary metal oxide semiconductor (CMOS) process, the gate oxide of NMOS and PMOS transistors are grown together [10]. Hence, I considered simultaneous variations of  $T_{oxnmos}$  and  $T_{oxpmos}$  with a correlation coefficient (cc) of 0.9 and a Gaussian distribution for both with  $\sigma = 10\%$ . One hundred Monte Carlo runs were considered. Figure 6.8 shows a Gaussian distribution of the oscillation frequency.

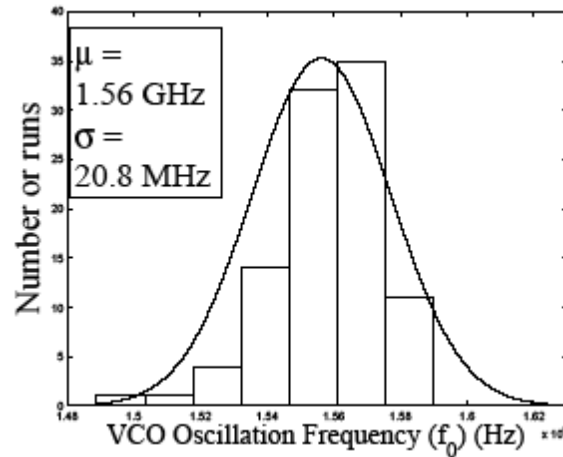


Figure 6.8. Statistical simultaneous  $T_{oxnmos} + T_{oxpmos}$  variation.

#### 6.2.2.5. Simultaneous $V_{dd}$ , $V_{Tnmos}$ , $V_{Tpmos}$ , $T_{oxnmos}$ and $T_{oxpmos}$ Variation

One thousand Monte Carlo runs were considered for simultaneous variation of all the process parameters with  $\sigma = 10\%$ . More numbers of runs give a more accurate picture. The distribution of  $f_0$  is shown in figure 6.9.

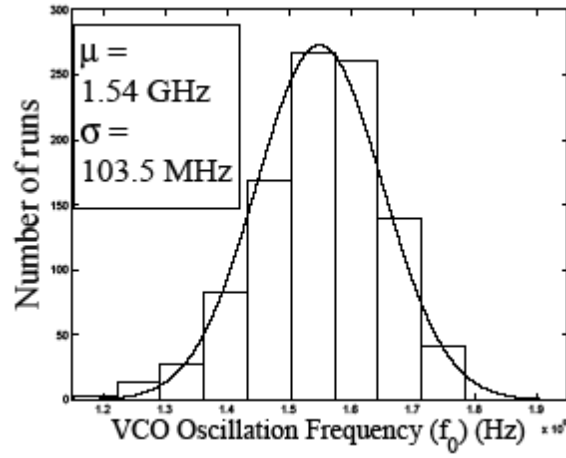


Figure 6.9.  $V_{dd} + V_{Tnmos} + V_{Tpmos} + T_{oxnmos} + T_{oxpmos}$  variation.

The value of the mean ( $\mu$ ) and the standard deviation ( $\sigma$ ) of the oscillation frequency for all 5 cases has been recorded in table 6.6. It can be seen that  $f_0$  shows greater dependence on  $V_{DD}$  and  $V_{Tnmos}$  (value of  $\sigma$  is greater) than  $V_{Tpmos}$ ,  $T_{oxnmos}$ , and  $T_{oxpmos}$ . However, in my methodology, I considered all these parameters to obtain more realistic results.

Table 6.6. Mean and Standard Deviation of Oscillation Frequency for 5 Cases

Parameter	Mean ( $\mu$ )	Std. Dev ( $\sigma$ )
Only $V_{dd}$ variation	1.54 GHz	77.9 MHz
Only $V_{Tnmos}$ variation	1.57 GHz	68.2 MHz
Only $V_{Tpmos}$ variation	1.56 GHz	19.7 MHz
$T_{oxnmos} + T_{oxpmos}$ (cc = 0.9)	1.56 GHz	20.8 MHz
$V_{dd} + V_{Tnmos} + V_{Tpmos} + T_{oxnmos} + T_{oxpmos}$	1.54 GHz	103.5 MHz

### 6.2.3. Parasitic- and Process-variation-aware Optimization

For the parasitic- and process-variation-aware design, baseline logical design presented in chapter 5 was used. The physical design was prepared by using this baseline design. A 25% discrepancy in the oscillation frequency was observed between the logical and the fully extracted (RCLK) physical design (as discussed in section 6.2.1). The parasitic parameterized netlist derived from this initial physical design was then subjected to process and supply variation where  $V_{dd}$ ,  $V_{Tnmos}$ ,  $V_{Tpms}$ ,  $T_{oxnmos}$  and  $T_{oxpmos}$  were varied by  $\pm 10\%$  from their nominal values. The worst case is identified as the one in which  $V_{dd}$  is reduced by 10%, and all the process parameters increased by 10%. In this case, a 43.5% discrepancy was observed in the oscillation frequency of the logical and the physical designs (figure 6.10). The results are summarized in table 6.7.

Table 6.7. Frequency Discrepancy and Worst-case Process Values for a Target Frequency  $\geq 2$  GHz

Parameter	Unoptimized physical design	Unoptimized physical design + process variation	Optimized physical design + process variation
Frequency	1.56 GHz	1.13 GHz	1.91 GHz
Discrepancy	25%	43.5%	4.5%
$V_{dd}$	1.2 V (nominal)	1.08 V (-10%)	1.08 V
$V_{Tnmos}$	0.1692662 V (nominal)	0.186193 V (+10%)	0.186193 V
$V_{Tpms}$	-0.1359511 V (nominal)	-0.149546 V (+10%)	-0.149546 V
$T_{oxnmos}$	2.33 nm (nominal)	2.563 nm (+10%)	2.563 nm
$T_{oxpmos}$	2.48 nm (nominal)	2.728 nm (+10%)	2.728 nm

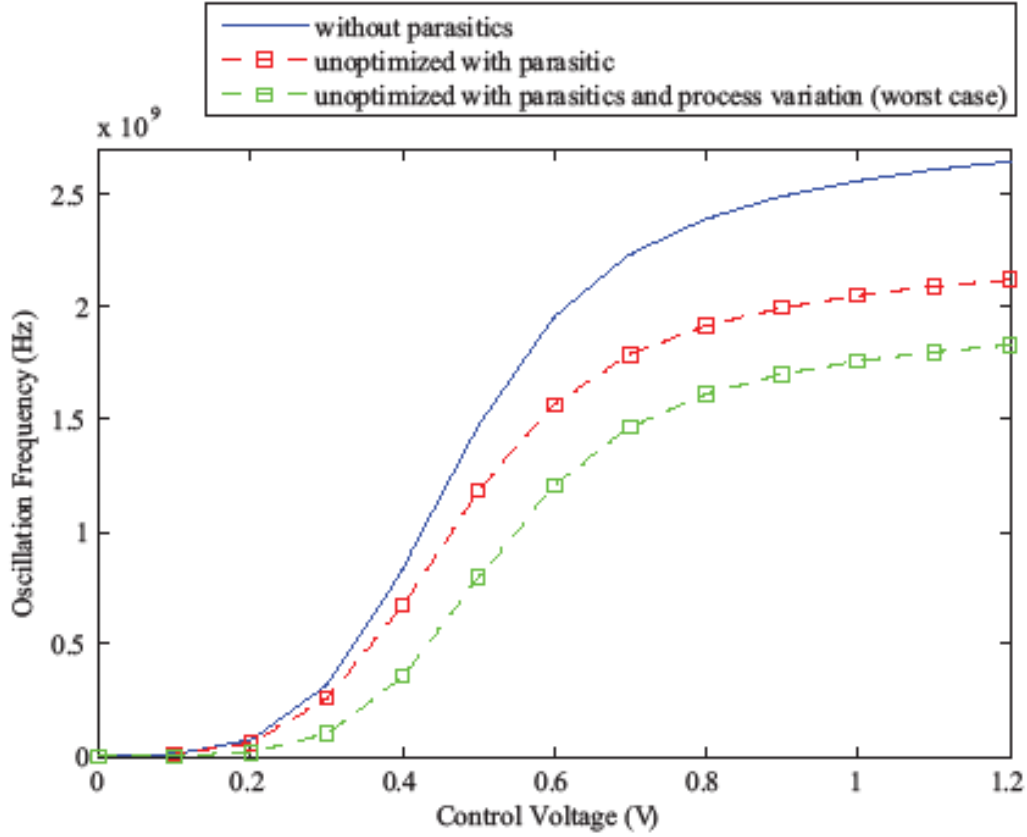


Figure 6.10. Comparison of frequency-voltage characteristics of the logical design, parasitic extracted physical design, and parasitic extracted physical design subjected to worst-case process variation.

The initial values of various attributes are as follows:

- Target oscillation frequency  $f_0 = 2$  GHz
- Logical design oscillation frequency  $f_{0,\text{logical}} = 1.95$  GHz
- Physical design oscillation frequency  $f_{0,\text{physical}} = 1.56$  GHz
- Physical design oscillation frequency in a worst case process variation environment

$$f_{0,\text{physical|process}} = 1.13 \text{ GHz}$$

Once again, the objective was to achieve a minimum target oscillation frequency of 2 GHz with a stopping criterion of 2%. The parasitic parameterized netlist generated from the first layout iteration was subjected to the optimization loop where the design variables were varied in



order to achieve the required performance criterion (oscillation frequency) in a worst-case process variation environment [48]. The design variables were the constraints for the design methodology. The sets of design variables used for optimization were as follows:

- Widths of NMOS devices in the inverter ( $W_n$ )
- Widths of PMOS devices in the inverter ( $W_p$ )
- Widths of NMOS devices in the current-starved circuitry ( $W_{ncs}$ )
- Widths of PMOS devices in the current-starved circuitry ( $W_{pcs}$ )
- Lengths of all devices ( $L_n = L_p = L_{ncs} = L_{pcs} = L$ )

The final optimal values obtained for the design variables are recorded in table 6.8.

Table 6.8. Final Optimal Values for Design Variables

Variable	Varied from	Varied to	Optimal value
$W_n$	200 nm	500 nm	415 nm
$W_p$	400 nm	1000 nm	665 nm
$W_{ncs}$	1 $\mu$ m	5 $\mu$ m	4 $\mu$ m
$W_{pcs}$	5 $\mu$ m	20 $\mu$ m	19 $\mu$ m
$L$	100 nm	110 nm	100 nm

The physical design of the VCO was then carried out using these parameter values, and the following results were obtained:

- Target oscillation frequency  $f_0 = 2$  GHz
- Logical design oscillation frequency  $f_{0,\text{logical}} = 1.95$  GHz
- Parasitic- and process-variation-aware physical design oscillation frequency in a worst-case process variation environment  $f_{0,\text{physical}|\text{process}} = 1.91$  GHz

- Parasitic- and process-variation-aware physical design oscillation frequency in a nominal case process environment  $f_{0,\text{physical}|\text{nominal}|\text{process}} = 2.54 \text{ GHz}$

Hence, I obtained a final optimized layout, with 1.91 GHz oscillation frequency under worst case process variation and 2.54 GHz oscillation frequency in nominal-case process conditions. This parasitic-aware, process-variation-tolerant layout of the VCO is shown in figure 6.11.

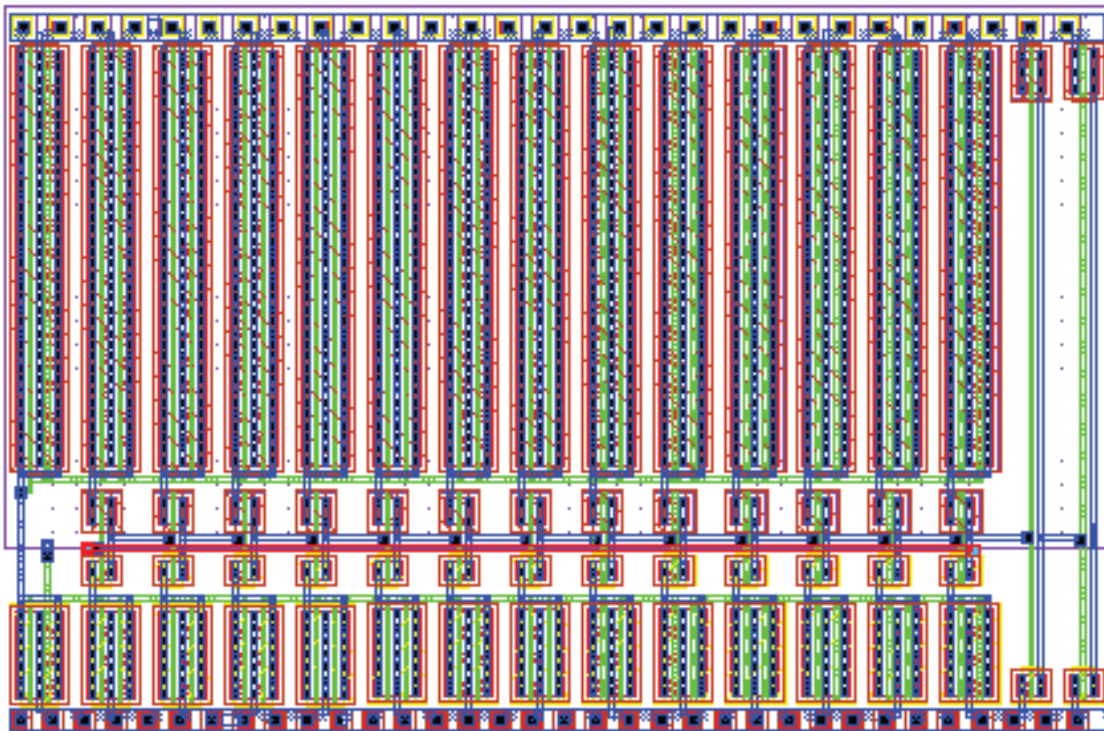


Figure 6.11. Final VCO layout optimized for parasitic- and process-variation-aware design flow.

I was able to obtain convergence with only one iteration in layout. This technique can also be applied for optimization of other parameters, such as phase noise and jitter. [54]. Figure 6.12 shows the frequency-voltage transfer curves for the logical and the physical designs after parasitic and process-variation-aware optimization. It is evident that the optimized curve closely

follows the logical design curve. I also obtained a phase noise of  $-109.13$  dBc/Hz at an offset frequency of 10 MHz. The performance summary of the VCO is shown in table 6.9.

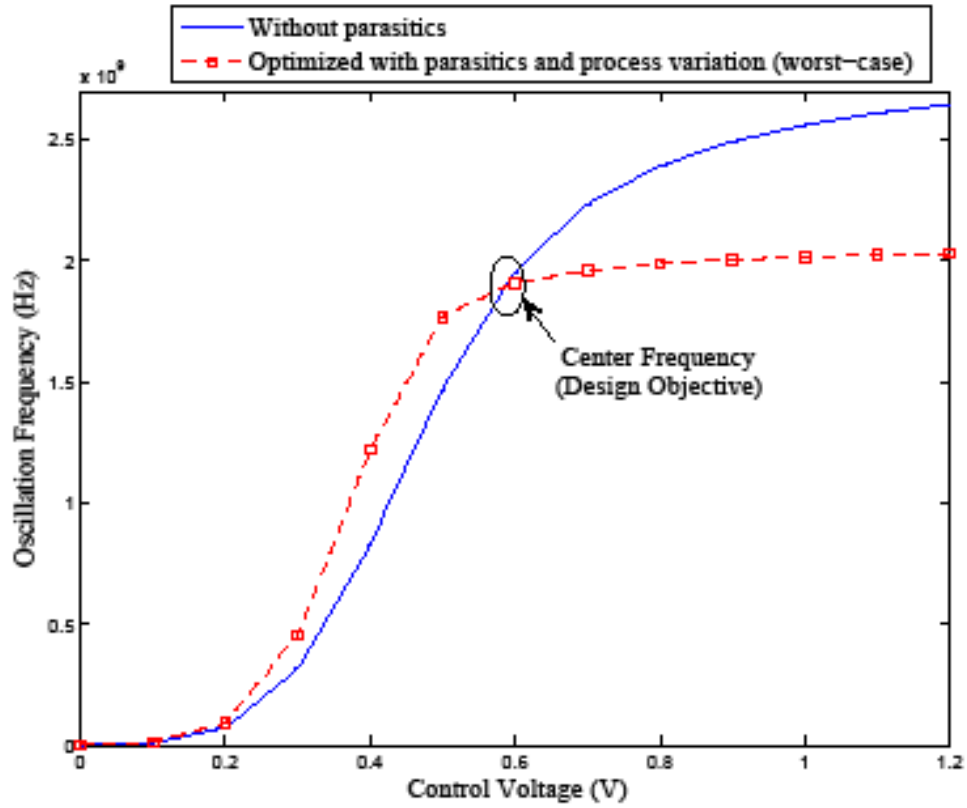


Figure 6.12. Frequency-voltage transfer characteristics of the VCO optimized for design flow accounting for parasitics and process variation.

Table 6.9. Performance Summary of the Parasitic and Process-variation-aware VCO

Parameter	Value
Technology	90 nm CMOS 1P 9M
Supply voltage ( $V_{dd}$ )	1.2 V
Oscillation frequency (nominal process)	2.54 GHz
Process and supply variation	$V_T (+10\%)$ , $T_{ox} (+10\%)$ , $V_{dd} (-10\%)$
Oscillation frequency (worst-case process)	1.91 GHz
Number of design variables	5 ( $W_n$ , $W_p$ , $W_{ncs}$ , $W_{pcs}$ , $L$ )
Number of objectives	1 ( $f_0 \geq 2$ GHz)

#### 6.2.4. Physical Design of the Optimal VCO

The physical design of the VCO was carried out using a generic 90 nm salicide 1.2 V/2.5 V 1 poly-9 metal process design kit. A full extraction of the layout was performed [including resistors (R), capacitors (C), inductors (L) and mutual inductors (K)] so that the impact of inductive coupling could be assessed and minimized on the layout. The final layouts for the parasitic-aware design flow and parasitic- and process-variation-aware design flow are shown in figures 6.3 and 6.11, respectively. For the parasitic- and process-variation-aware design, multifingered transistors are laid out to minimize the area's overhead, considering that the optimization resulted in wide transistors.

#### 6.3. Universal Voltage Level Converter (ULC)

To minimize power, I first identified the power-hungry transistors (shown in figure 5.20) by measuring the power consumed by each transistor of the circuit. The power estimation included dynamic, subthreshold, and gate leakage, as presented in chapter 2. These transistors were then subjected to the power-delay optimization technique. Two types of optimization techniques were used:

- Dual  $T_{ox}$
- Dual  $V_T$

##### 6.3.1. Dual $T_{ox}$ Technique

The  $T_{ox}$  was varied between 10% and 200% of its nominal value, and the width of transistors was varied from 120 nm to 1  $\mu$ m. All transistors were assumed to have an effective length of 100 nm corresponding to the nominal value of the 90 nm process design kit used. To optimize the power and delay, I varied the following parameters:

- $T_{ox}$  of the power-hungry NMOS transistors ( $T_{oxnmos}$ )

- $T_{ox}$  of the power-hungry PMOS transistors ( $T_{oxpmos}$ )
- Width ( $W_{nmosdown}$ ) of the NMOS transistors of the down converter
- Width ( $W_{pmosdown}$ ) of the PMOS transistors of the down converter
- Width ( $W_{nmosup}$ ) of the NMOS transistors of the up converter
- Width ( $W_{pmosup}$ ) of the PMOS transistors of the up converter

The final optimal values of these parameters are given in table 6.10.

Table 6.10. Final Values of the Optimization Parameters Using the DOX-CMOS Technique

Variable	Varied from	Varied to	Optimal value
$T_{oxnmos}$	2.563 nm	4.66 nm	2.667 nm
$T_{oxpmos}$	2.728 nm	4.96 nm	3.624 nm
$W_{pmosup}$	120 nm	1 $\mu$ m	220.1 nm
$W_{nmosup}$	120 nm	1 $\mu$ m	428.3 nm
$W_{pmosdown}$	120 nm	1 $\mu$ m	298.9 nm
$W_{nmosdown}$	120 nm	1 $\mu$ m	120 nm

The optimized values of delay and power were obtained as:

- Optimized average power ( $P_{ULC}$ ) = 16.68 $\mu$ W
- Delay of up converter ( $Delay_{up}$ ) = 80.35 ps
- Delay of down converter ( $Delay_{down}$ ) = 80.43 ps
- Average delay ( $Delay_{ULC}$ ) = 80.39 ps

I achieved 83% power savings compared to the baseline design and 60% delay savings compared to the existing designs presented in the literature [57].

### 6.3.2. Dual $V_T$ Technique

The dual  $V_T$  technique [34] was used along with transistor geometry to achieve a power-delay optimized ULC. Minimizing power consumption was the target objective function, with a delay constraint. The power-hungry transistors were assigned high  $V_T$  values, which reduced the power consumption considerably but which also increased the delay (equation 4). Hence, the transistor geometry was also explored, where the widths of all the transistors in the level-up and level-down converters were considered. Hence, a simultaneous variation of the design variables (i.e.,  $V_{Tpmos}$ ,  $V_{Tnmos}$ ,  $W_{pmosup}$ ,  $W_{nmosup}$ ,  $W_{pmosdown}$ , and  $W_{nmosdown}$ ) achieved a good power-delay optimization. The final values are shown in table 6.11.

Table 6.11. Optimal Design Variable Values Using the DVTCMOS Technique

Variable	Varied from	Varied to	Optimal value
$V_{Tpmos}$	-0.476 V	-0.136 V	- 0.432 V
$V_{Tnmos}$	0.169 V	0.592 V	0.309 V
$W_{pmosup}$	120 nm	1 $\mu$ m	121.4 nm
$W_{nmosup}$	120 nm	1 $\mu$ m	519.6 nm
$W_{pmosdown}$	120 nm	1 $\mu$ m	370 nm
$W_{nmosdown}$	120 nm	1 $\mu$ m	139.3 nm

To optimize the power and delay, I varied the following parameters:

- $V_T$  of the power-hungry NMOS transistors ( $V_{Tnmos}$ )
- $V_T$  of the power-hungry PMOS transistors ( $V_{Tpmos}$ )
- Width ( $W_{nmosdown}$ ) of the NMOS transistors of the down converter
- Width ( $W_{pmosdown}$ ) of the PMOS transistors of the down converter

- Width ( $W_{nmosup}$ ) of the NMOS transistors of the up converter
- Width ( $W_{pmosup}$ ) of the PMOS transistors of the up converter

The optimized values of delay and power were obtained as:

- Optimized average power ( $P_{ULC}$ ) = 10.95  $\mu$ W
- Delay of up converter ( $Delay_{up}$ ) = 95.1 ps
- Delay of down converter ( $Delay_{down}$ ) = 95.7 ps
- Average delay ( $Delay_{ULC}$ ) = 95.4 ps

With the dual threshold, complementary metal oxide semiconductor (DVTCMOS) technique, 178% power savings occurred compared to the baseline design and 35% delay savings occurred compared to the existing designs presented in the literature [57].

### 6.3.3. Characterization

In low-power circuit designs, it is of paramount importance to consider various design constraints concerning power consumption, lower voltage level and load, and many more. My design of the universal voltage level converter (ULC) mainly focuses on low-power multivoltage circuit applications. Thus, it is essential to consider these design limitations. Keeping in mind these design constraints and ensuring that the ULC design is essentially a low-power-consuming circuit in itself, I studied and analyzed the ULC circuit under various input conditions. The circuit was characterized by performing the following three analyses:

- Parametric analysis
- Load analysis
- Power analysis

These characterizations are discussed in the following subsections.

#### 6.3.3.1. Parametric Analysis

Parametric analysis is a process in which the circuit's behavior is observed while continuously changing one of its input parameters. In this type of analysis, a transient analysis is carried out where the output voltage is observed for a varying input voltage. For testing the level-up converter,  $V_{in}$  was varied from 0.1 V to 1.02 V with an increasing step of 0.1 V. The value of control signals S1, S0 was kept at 1, 0 to achieve the level-up conversion functionality. The output signal was observed at the output terminal  $V_{out}$  of the ULC. The plot for the parametric analysis for up conversion is shown in the lower graph (b) of figure 6.13, which confirms that the circuit produces a stable output even for a voltage  $V_{in}$  as low as 0.65 V. The same steps were followed for level-down converter parametric analysis. The values for the control signals S1, S0 were kept at 0, 1. In this case,  $V_{in}$  was varied from 0.1 V to 1.2 V with an increasing step size of 0.1 V. The output plot for the down converter parametric analysis is shown in the upper graph (a) of figure 6.13. From the plot, it can be determined that the down converter circuit can produce a stable output even for  $V_{in}$  as low as 0.6 V.



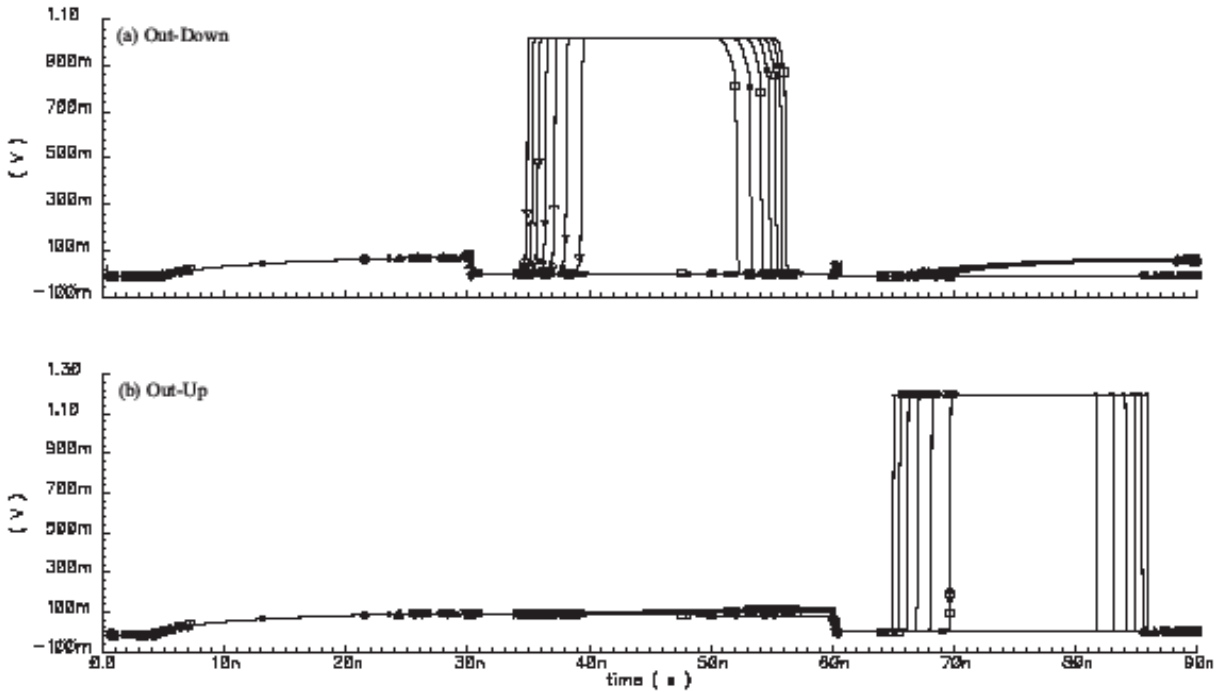


Figure 6.13. Parametric analysis with input voltage sweep.

#### 6.3.3.2. Load Analysis

Load analysis is a very important category of analysis for any electrical system design. Load analysis helps the designer understand the transient behavior of a system at different loads which mainly helps in verifying the overall system functionality. Each gate connected to the output of another gate loads the later gate. Electronic constraints limit the load on a gate and hence the number of gates connected to its output. The ULC is used as an interface between two circuits (or gates) operating at different voltage levels. The output load of the level converting circuit may change quite often. Thus, it is of great importance to ensure that the design of ULC produces the desired results even under such varying load conditions. Therefore, a load analysis on the ULC is performed when the output load capacitance of the circuit is varied and the effect of that on the output signal is observed.

During the load analysis of the ULC, the output of the circuit is studied by varying the capacitive load at the output from 10 fF to 200 fF. These values of load capacitance represent realistic loads [128] for a 90 nm CMOS technology. From this analysis, it can be concluded that the ULC produces stable output under varying load conditions. This design feature is important for voltage level converters. Figure 6.14 shows the output plot for load analysis on the complete ULC.

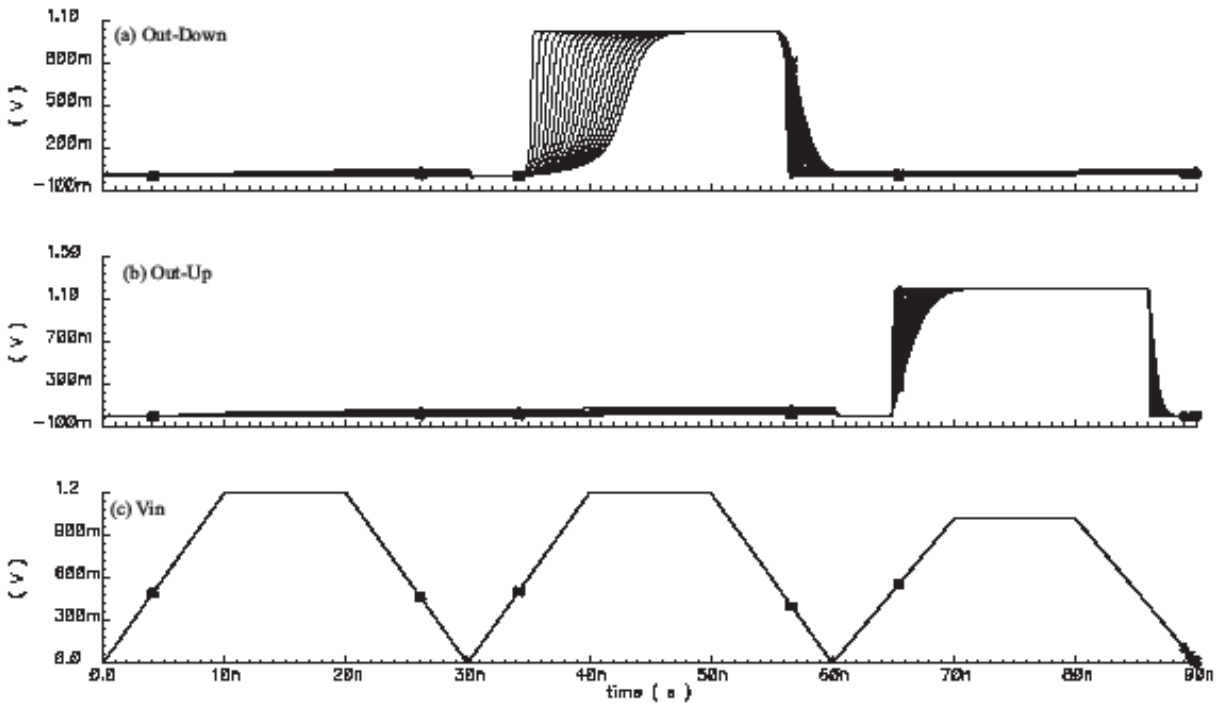


Figure 6.14. Performance of the ULC under varying output capacitive load.

#### 6.3.3.3. Power Analysis

Power analysis includes determining the total power consumed by the overall ULC circuit. During the power analysis, the total power consumed by the ULC at three different loads of 10 fF, 45 fF and 90 fF is calculated (shown in table 6.12). It is evident that there is not a significant difference in power consumption with varying loads.

Table 6.12. Power Consumption

Capacitive load (fF)	Average power consumption ( $\mu\text{W}$ )
10	17.23
45	19.89
90	23.27

Figure 6.15 shows the instantaneous power plot of the ULC at a capacitive load of 45 fF. Power measurement includes switching power, short-circuit power, standby-leakage power, and gate-oxide leakage consumed by the circuit.

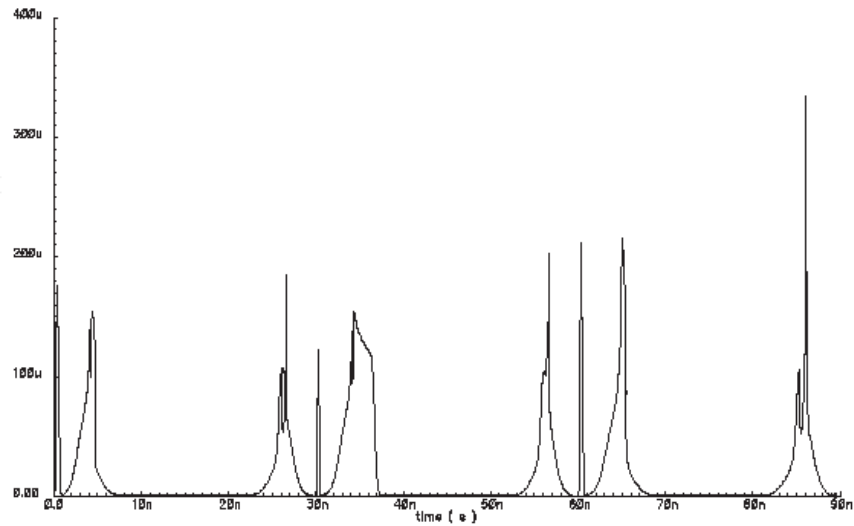


Figure 6.15. Instantaneous power plot of the ULC at a load capacitance of 45 fF. Average power consumed = 1989.  $\mu\text{W}$ .

#### 6.4. Active Pixel Sensor (APS)

The design flow presented in figure 6.16 was used for variability-aware optimization of a nanometer-scale CMOS APS array.

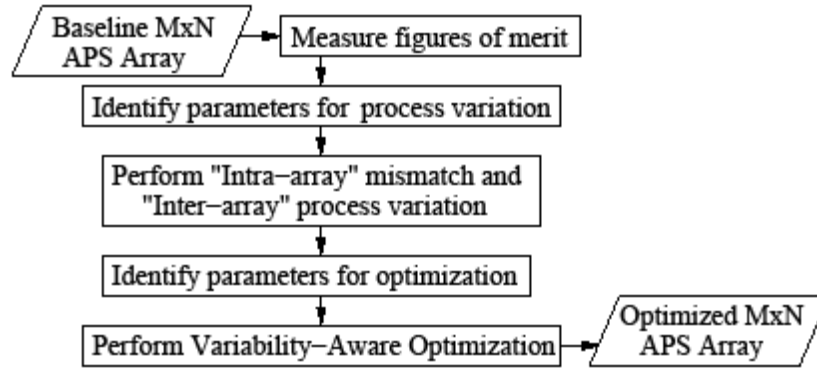


Figure 6.16. Proposed design flow for optimal design of nano-CMOS APS array.

The first step in the design flow was the design of a baseline array for a specific nano-CMOS technology node. Then, the baseline  $M \times N$  array was simulated for functional correctness. This step was followed by measuring the baseline values of the various figures of merit, such as power, leakage, voltage swing, and capture time. The target figures of merit that needed to be optimized were identified. Because nanoscale circuits suffer from high leakage, I chose to optimize average power ( $P_{\text{APS}}$ ) with minimum degradation in output voltage swing ( $V_{\text{swing}}$ ). These metrics are defined in chapter 5.

In the next step, the parameters to be used for process variation were identified. The array was then subjected to simultaneous “intra-array” mismatch and “inter-array” process variation. The intra-array mismatch can also be interpreted as pixel-to-pixel variation. This variation enables designers to consider the trade-off between matched transistor size and yield when designing their circuits.

Once the process variation results were analyzed, the design flow proceeded to the optimization. In the optimization, the parameters to be used as design variables were identified. Then I performed a design and analysis optimization based on Monte Carlo experiments. The design flow led to an optimized APS array, which is also the output of this design flow. The

details of the optimization algorithm were presented in chapter 4. Hence, the end product was a  $M \times N$  APS array optimized for nanoscale process variations.

The APS array was subjected to simultaneous intra-array mismatch and inter-array process variation, and the effects on the figures of merit were studied. The process parameters identified for mismatch and process variation were: (i) supply voltage  $V_{dd}$ , (ii) NMOS threshold voltage  $V_{Tnmos}$ , (iii) PMOS threshold voltage  $V_{Tpms}$ , (iv) NMOS gate-oxide thickness  $T_{oxnmos}$ , and (v) PMOS gate-oxide thickness  $T_{oxpms}$ . The figures of merit under consideration were  $P_{APS}$  and  $V_{swing}$ . Hence they formed the objective set  $F$  for optimization. The process parameters were subjected to intra-array mismatch and inter-array process variation simultaneously for  $R = 1000$  runs. For the intra-array mismatch, the parameters were assumed to have a Gaussian distribution and were assigned mean ( $\mu$ ) values as the baseline values specified in the predictive technology model (PTM), and a standard deviation ( $\sigma$ ) of 5%. For the inter-array process variation, the parameters were also assumed to have a Gaussian distribution and were assigned mean ( $\mu$ ) values as the baseline values specified in the PTM and a standard deviation ( $\sigma$ ) of 10%.  $P_{APS}$  shows a lognormal distribution in the upper graph (a) of figure 17. Because of significant impact of various leakage mechanisms ( $P_{sub}$ ,  $P_{gate}$ ) having an exponential relationship with the process parameters, this observation was intuitive from the governing expressions.  $V_{swing}$  showed a Gaussian (normal) distribution [figure 17(b)]. This distribution is considered the baseline case.

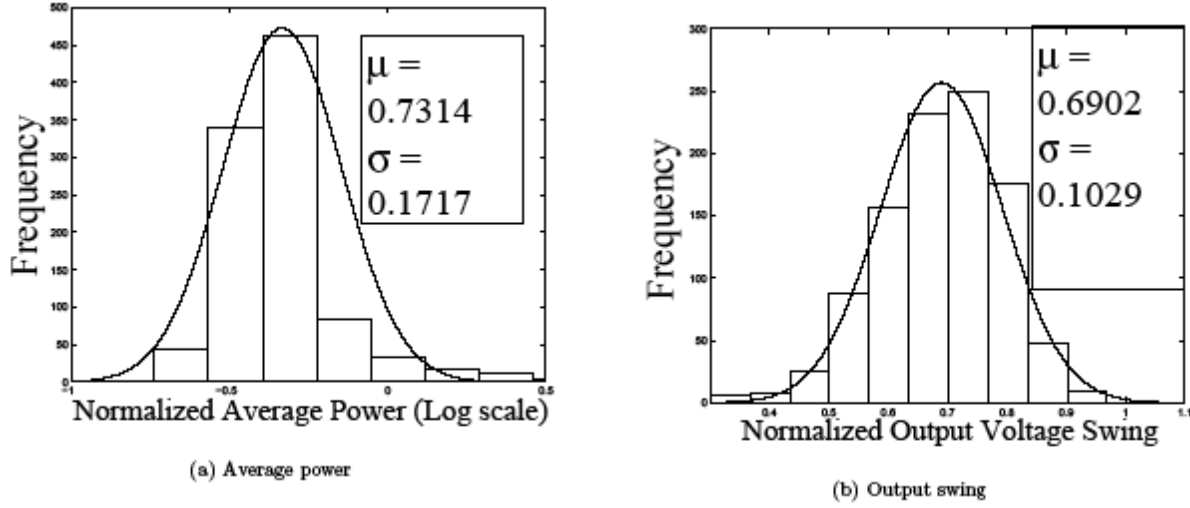


Figure 6.17. Distribution of (a) average power  $P_{APS}$  and (b) output voltage swing  $V_{swing}$  for the case  $V_{dd} = V_{dd-H}$  and  $T_{xo} = T_{ox-L}$ .

To demonstrate the array optimization,  $P_{APS}$  minimization and  $V_{swing}$  maximization were kept as the objectives. Power is always a constraint for nanoscale SoCs. Hence,  $P_{APS}$  was chosen. Also,  $V_{swing}$  directly affects the dynamic range of the APS, thus giving an important measure of performance. The proposed methodology can also be extended to other figures of merit as a multiobjective optimization. However, it is unlikely that both these objectives would be optimized by the same alternative parameter choices. For design and analysis of Monte Carlo experiments, the parameters to be used as design variables for optimization were identified as follows: (i) supply voltage  $V_{dd}$ , (ii) NMOS gate-oxide thickness  $T_{oxnmos}$ , and (iii) PMOS gate-oxide thickness  $T_{oxpmos}$ . From the power model equations presented in chapter 2, it can be seen that these parameters affect the power consumption significantly. Hence, they form the design variable set  $D$  for the optimization algorithm. I did not consider  $V_{Tnmos}$  and  $V_{Tpmos}$  as optimization parameters because they depend on a variety of parameters, such as doping concentration of source or drain diffusions and channel length [1].

I now present the algorithm for two values of design variables with H denoting high and L denoting low values. Thus,  $V_{dd-H}$ ,  $V_{dd-L}$ ,  $T_{ox-H}$ , and  $T_{ox-L}$  are the possible values of the design variables.  $V_{dd-H}$  and  $T_{ox-L}$  are baseline values as per the 32 nm CMOS technology node.  $V_{dd}$  scaling refers to reduction in  $V_{dd}$  (i.e. from  $V_{dd-H}$  to  $V_{dd-L}$ ), whereas  $T_{ox}$  scaling refers to increase in  $T_{ox}$  (i.e., from  $T_{ox-L}$  to  $T_{ox-H}$ ). As in a traditional CMOS process, the gate oxides of NMOS and PMOS transistors are grown together,  $T_{oxnmos}$ ;  $T_{oxpmos}$  are scaled together, i.e., they are assigned either a higher ( $T_{ox-H}$ ) or a lower ( $T_{ox-L}$ ) value together.

For the above scenario, we have four different combinations. However, the situation is much more involved for other discrete sets of design variables. These values are assigned to the  $\mu$  of optimization parameters for  $R = 100$  Monte Carlo runs. The array is subjected to 5% intra-array mismatch and 10% inter-array process variation for each of the four combinations. The Monte Carlo data for F are obtained and normalized. Normalization involves division of each value of the data by the maximum value of data. The  $\mu$  and  $\sigma$  values for  $P_{APS}$  and  $V_{swing}$  are listed in table 6.13 for  $V_{dd-H} = 0.9V$ ,  $V_{dd-L} = 0.7V$ ,  $T_{ox-H} = 2.0nm$ , and  $T_{ox-L} = 1.65nm$ .  $P_{APS}$  is observed to have a lognormal distribution [figure 17(a), 18(a), 19(a), and 20(a)] and  $V_{swing}$  is observed to have a Gaussian distribution [figure 17(b), 18(b), 19(b), and 20(b)] using a least-squares fit.

Table 6.13. Monte Carlo Simulation Results

$V_{dd}$ (V)	$T_{ox}$ (nm)	$\mu_{PAPS}$	$\sigma_{PAPS}$	$\mu_{Vswing}$	$\sigma_{Vswing}$
$V_{dd-L}$	$T_{ox-L}$	0.5774	0.1306	0.5058	0.1402
$V_{dd-L}$	$T_{ox-H}$	0.5517	0.0847	0.5373	0.1424
$V_{dd-H}$	$T_{ox-L}$	0.7314	0.1717	0.6902	0.1029
$V_{dd-H}$	$T_{ox-H}$	0.6839	0.0760	0.7120	0.1077

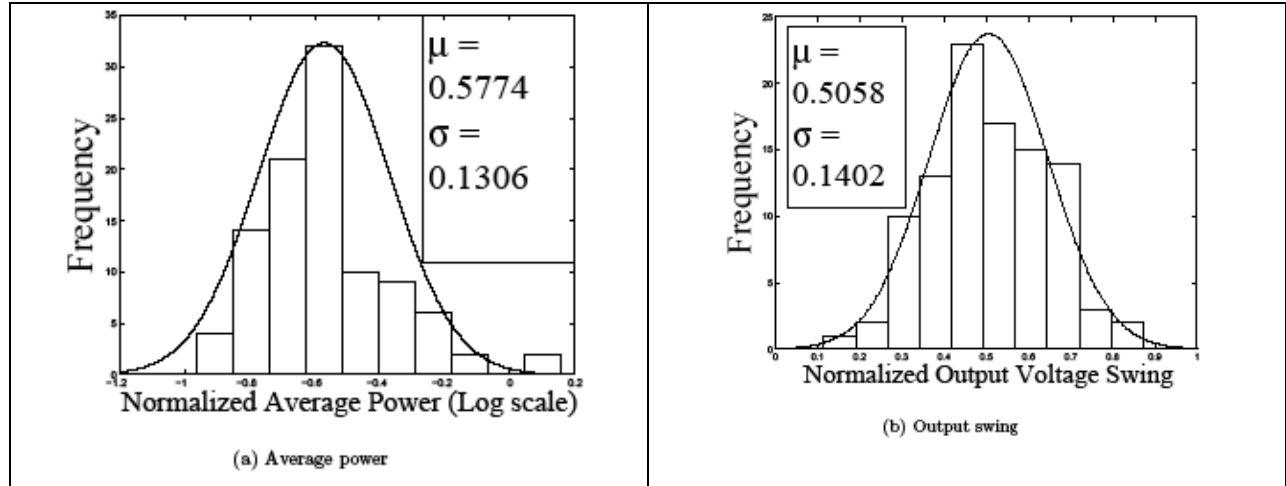


Figure 6.18. Distribution of (a) average power  $P_{APS}$  and (b) output voltage swing  $V_{swing}$  for the case  $V_{dd} = V_{dd-L}$  and  $T_{xo} = T_{ox-L}$ .

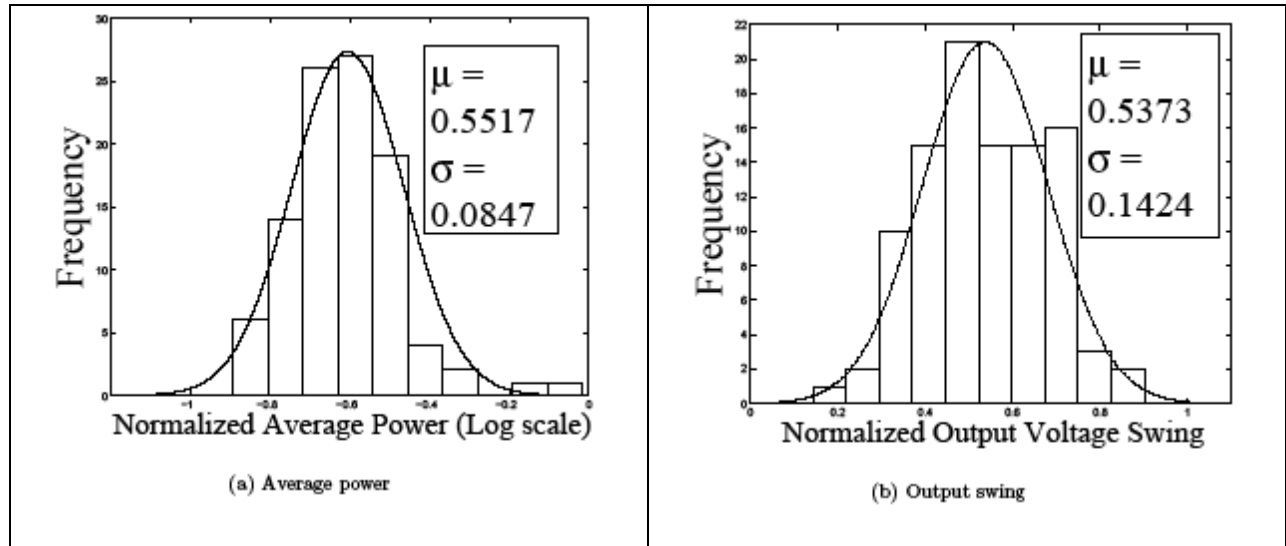


Figure 6.19. Distribution of (a) average power  $P_{APS}$  and (b) output voltage swing  $V_{swing}$  for the case  $V_{dd} = V_{dd-L}$  and  $T_{xo} = T_{ox-H}$ .



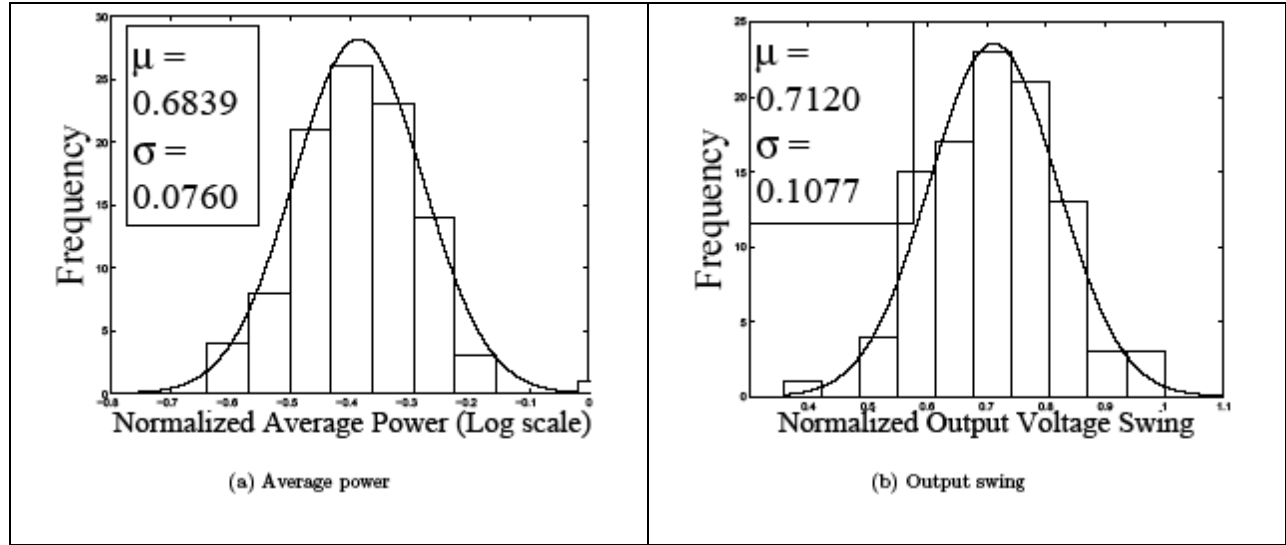


Figure 6.20. Distribution of (a) average power  $P_{APS}$  and (b) output voltage swing  $V_{swing}$  for the case  $V_{dd} = V_{dd-H}$  and  $T_{xo} = T_{ox-H}$ .

The following prediction equations were obtained by using the design of experiments method on Monte Carlo experiments:

$$(21) \quad \hat{\mu} P_{APS} = 0.6361 + 0.0716 \times V_{dd} - 0.0183 \times T_{ox}$$

$$(22) \quad \hat{\sigma} P_{APS} = 0.1157 + 0.0081 \times V_{dd} - 0.0354 \times T_{ox}$$

$$(23) \quad \hat{\mu} V_{swing} = 0.6113 + 0.0898 \times V_{dd} + 0.0133 \times T_{ox}$$

$$(24) \quad \hat{\sigma} V_{swing} = 0.1233 - 0.0180 \times V_{dd} + 0.0018 \times T_{ox}$$

The prediction equations are of the form:

$$(25) \quad \hat{Y} = \bar{Y} + \frac{\Delta V_{dd}}{2} \times V_{dd} + \frac{\Delta T_{ox}}{2} \times T_{ox}$$

where  $\hat{Y}$  is the response,  $\bar{Y}$  is the average, and  $\frac{\Delta V_{dd}}{2}$  and  $\frac{\Delta T_{ox}}{2}$  are the half effects of the design variables. A linear relationship between the design variables and the response is assumed, as this reduces the complexity considerably, with a maximum discrepancy of 1% between the observed results and the results calculated with the predictive equations. If a nonlinear relationship is

assumed, the complexity would increase exponentially. From equations 21, 22 and 24, it can be observed that  $\hat{\mu} P_{APS}$ ,  $\hat{\sigma} P_{APS}$  and  $\hat{\sigma} V_{swing}$  are to be minimized for power minimization, whereas  $\hat{\mu} V_{swing}$  needs to be maximized for  $V_{swing}$  maximization (equation 23). It can be seen that  $\hat{\mu} P_{APS}$  and  $\hat{\sigma} P_{APS}$  are perfectly correlated; i.e., optimizing the mean would also optimize the standard deviation. However,  $\hat{\mu} V_{swing}$  and  $\hat{\sigma} V_{swing}$  are not correlated. Hence, a combined effect of the mean and the standard deviation must be considered for possible generalization of the proposed methodology. This information is also available only after the prediction equations have been obtained.

The purpose of the paper is process optimization. Parametric yield is not under consideration here. I formed two objective functions,  $fP_{APS}$  and  $fV_{swing}$ , as follows:

$$(26) \quad \begin{aligned} f_{P_{APS}} &= \hat{\mu}_{P_{APS}} + 3 \times \hat{\sigma}_{P_{APS}} \\ &= 0.9832 + 0.0959 \times V_{dd} - 0.1245 \times T_{ox} \end{aligned}$$

$$(27) \quad \begin{aligned} f_{V_{swing}} &= \hat{\mu}_{V_{swing}} - 3 \times \hat{\sigma}_{V_{swing}} \\ &= 0.2414 + 0.1438 \times V_{dd} + 0.0079 \times T_{ox} \end{aligned}$$

From equations 26 and 27, it can be seen that  $fP_{APS}$  needs to be minimized and  $fV_{swing}$  needs to be maximized. The Pareto chart for  $fP_{APS}$  in figure 21(a) shows that the design variable set  $D = [V_{dd-L}, T_{ox-H}]$  leads to the minimum value of  $fP_{APS}$ . The value of  $fV_{swing}$  corresponding to this set [figure 21(b)] is also acceptable. This is confirmed by using this value of D to simulate the array, which yields an acceptable  $V_{swing}$  (46.4% of  $V_{dd}$ ). Because a nanoscale circuit is involved, power minimization is treated as primary objective. A reduction of 21% in  $P_{APS}$  with a 24% reduction penalty in  $V_{swing}$  can be achieved. The baseline and optimal values of  $P_{APS}$  and  $V_{swing}$  are shown in table 6.14. The algorithm is shown as a flowchart in figure 6.22.

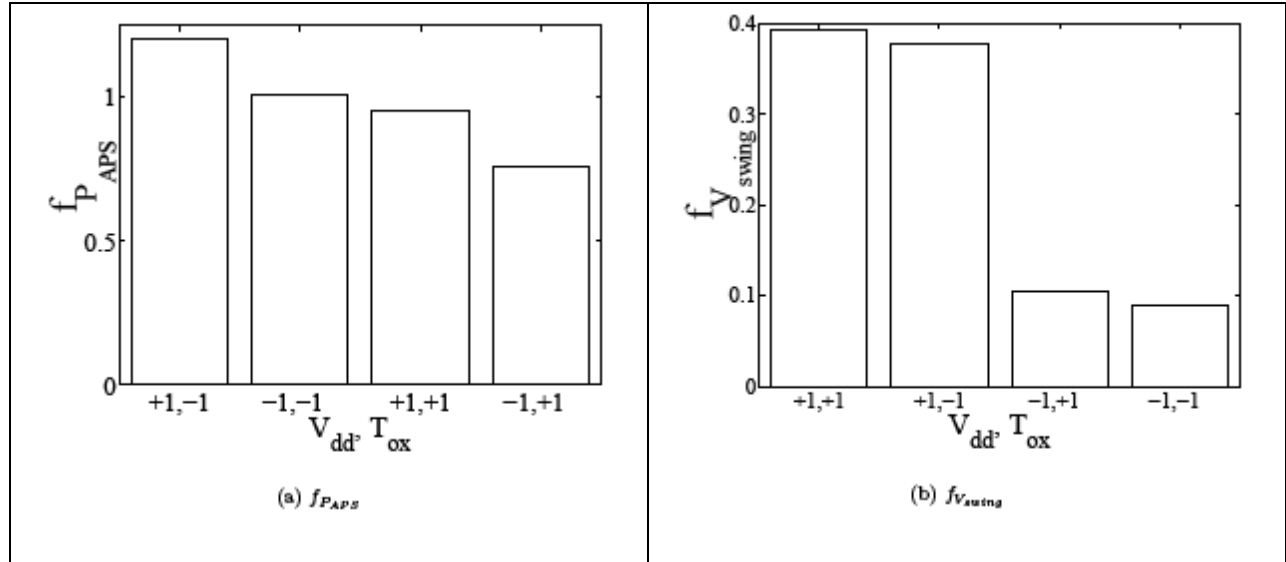


Figure 6.21. Pareto plots for (a)  $f_{P_{APS}}$  and (b)  $f_{V_{swing}}$ .

Table 6.14. Baseline and Optimal Values of the Figures of Merit

Value	$P_{APS}$ ( $\mu$ W)	$V_{swing}$ (mV)
Baseline	16.32	428
Optimal	12.91	325

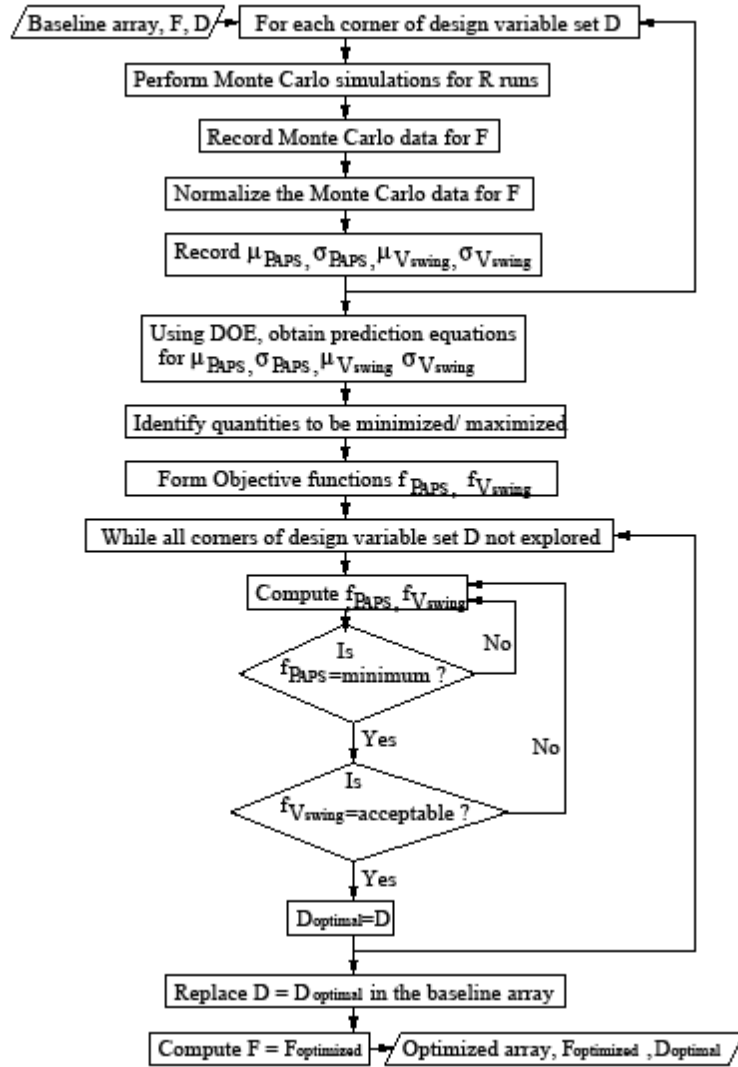


Figure 6.22. Flowchart of the proposed algorithm.

## CHAPTER 7

### CONCLUSION AND FUTURE WORKS

This chapter presents a summary of the dissertation, followed by conclusions drawn from the research. Finally, directions for future research are discussed.

#### 7.1. Summary

This dissertation describes low-power design techniques that were applied to nanoscale and emerging technology based mixed-signal circuits. Optimization approaches have been applied to these circuits to achieve low-power designs which are also process-variation-tolerant.

The optimization methodologies proposed are the following:

- Single iteration automatic approach
- Hybrid Monte Carlo/DOE approach
- Corner-based methodology

The following circuits were subjected to these optimization methodologies:

- 90 nm analog-to-digital converter (ADC)
- 90 nm voltage-controlled oscillator (VCO)
- 90 nm universal voltage level converter (ULC)
- 32 nm active pixel sensor (APS)

The following section presents the conclusions drawn from the experimental results.

#### 7.2. Conclusions

For the ADC, the design of a process- and supply-variation-aware, low-voltage, high-speed circuit was presented. The design was functionally verified and characterized for nanoscale feature sizes (90 nm and 45 nm). The physical design of the ADC was performed by using a 90 nm digital complementary metal oxide semiconductor (CMOS) process,

demonstrating its system-on-a-chip (SoC) readiness. The comparators were designed by using the threshold inverting technique. The nominal results at 90 nm show that the ADC has an integral nonlinearity (INL) of 0.344 least significant bit (LSB) and a differential nonlinearity (DNL) of 0.459 LSB, showing a maximum variation of 10.5% and 5.7%, respectively, when subjected to  $\pm 10\%$  variation in the supply and  $\pm 5\%$  mismatch in the transistor threshold voltages. The analog supply voltage is 1.2 V. At 45 nm, the ADC exhibits INL = 0.46 LSB, DNL = 0.7 LSB at a supply voltage of 0.7 V. This is one of the lowest published power supply values used to implement high speed 6-bit ADCs. Several design issues were also addressed and used in the optimization procedure of the ADC; e.g., current-resistance (IR) drop and low  $V_{LSB}$ . It is demonstrated that the design of low-voltage, high-speed, and SoC-ready ADCs is possible at 90 nm technology and below.

For the VCO, two novel design flows for parasitic- and process-variation-aware design methodology for optimization of performance for radiofrequency (RF) circuit components have been presented. The first design flow, called parasitic aware design flow, considers parasitics. The second design flow considers process variation along with parasitics; hence, it is called parasitic- and process-variation-aware design flow. A high-frequency, low-phase noise, current-starved VCO was used as a case study. The oscillation frequency was treated as the target specification. The degradation of the oscillation frequency that was due to parasitics only was narrowed down from 25% to 1%. The degradation of the oscillation frequency that was due to parasitic and process variation effects was narrowed down from 43.5% to 4.5% in only one iteration of the physical design, a tremendous reduction in overall design time. Thus, I obtained a parasitic- and process-variation-aware design, as the target technology is nanoscale CMOS in which such variations do affect design metrics and yield.

For the ULC, a dual-gate oxide thickness ( $T_{ox}$ ) (DOXCMOS)/ dual-threshold ( $V_T$ ) (DVTCMOS) approach along with transistor geometry variations to reduce the power-delay overhead of a ULC has been proposed. To the best of my knowledge, this is the first ULC being subjected to such power-saving techniques. It was observed that while DVTCMOS might be the preferred technique for achieving lower power, DOXCMOS gives better delay savings. Other analog circuits might also be subjected to such techniques in the future.

The ULC is capable of performing three types of distinct operations on the input signal; i.e., level-up conversion, level-down conversion, and blocking of the input signal. This makes the ULC highly suitable for use in the context of dynamic power management techniques in circuits. The robustness of the level converter is tested by using parametric, load and power analysis. It is observed that a stable output is obtained for voltages as low as 0.6 V and capacitive loads varying from 10 fF to 200 fF. The average power consumption of the level converter is 16.68 milliwatts ( $\mu$ W) with DOXCMOS, and 10.95  $\mu$ W with DVTCMOS, making the design suitable for low power applications. The design is also area-optimal. The physical design of the level converter was also presented. At 90 nm technology, subthreshold leakage is more dominant than gate oxide leakage [5]. Hence, from table 7.1 it can be seen that DVTCMOS achieves more power savings than DOXCMOS. However, the DOXCMOS technique shows better delay savings than DVTCMOS. Depending on the requirements of the designer, a choice can be made.

Table 7.1. Comparison of Results of Optimization Approaches

Approach	$P_{ULC}$	$P_{ULC}$ savings	$Delay_{ULC}$	$Delay_{ULC}$ savings
DOXCMOS	16.68 $\mu$ W	83%	80.39 ps	60%
DVTCMOS	10.95 $\mu$ W	178%	95.4 ps	35%

For the APS, I presented a novel design flow and optimization algorithm suitable for variation-tolerant (robust) design of nano-CMOS-based APS array. A 32 nm  $8 \times 8$  APS array was subjected to this design flow in the presence of simultaneous intra-array mismatch and inter-array process variation. This gives APS designers an insight into the yield of their circuits that might be caused by transistor mismatch and process variation before going into fabrication. Design and analysis of Monte Carlo experiments on the baseline array was carried out leading to 21% power reduction at the cost of 24% output voltage swing reduction.

### 7.3. Future Research

For the ADC, as part of a future work, I plan to carry out the complete design cycle including physical design for this ADC at 45 nm. Alternative encoder architectures will be explored to achieve higher sampling speeds. For the VCO, the current work might be extended to study the simultaneous optimization of oscillation frequency, response linearity and phase noise using the proposed methodology.

As part of future work for the ULC, I plan to implement this design at a lower technology node, i.e., 45 nm. The layout rules will be scaled from 90 nm to 45 nm and the layout of the design will be carried out. Efforts are also being undertaken to include the block functionality in the level converter design itself. In addition, the impact of parasitics on the performance of the ULC physical design using dual- $V_T$  and dual- $T_{ox}$  process kits might be studied. For future work on the APS, I plan to implement the proposed array using alternative technologies such as high- $\kappa$ /metal gate, carbon nanotube (CNT), dual-gate field effect transistors (FETs) and analyze their performance.



## REFERENCES

- [1] *BSIM4 MOS Models, Release 4.5.0.*, <http://www.device.eecs.berkeley.edu/~bsim3/bsim4.html>
- [2] *Histogram Testing Determines DNL and INL Errors*, [http://www.maxim-ic.com/appnotes.cfm/an\\_pk/2085](http://www.maxim-ic.com/appnotes.cfm/an_pk/2085)
- [3] *Maxim Integrated Products. Defining and Testing Dynamic Parameters in High Speed ADCs, 2001*, [http://www.maxim-ic.com/appnotes.cfm/an\\_pk/728](http://www.maxim-ic.com/appnotes.cfm/an_pk/728)
- [4] *Meet the World's First 45nm Processor*, [http://www.intel.com/technology/silicon/45nm\\_technology.htm](http://www.intel.com/technology/silicon/45nm_technology.htm)
- [5] *Semiconductor Industry Association, International Technology Roadmap for Semiconductors*, <http://public.itrs.net>
- [6] A. Abo and P. Gray. 1999. *A 1.5 V, 10-bit, 14.3-MS/s CMOS pipeline analog-to-digital converter*, *IEEE, Journal of Solid State Circuits* 34, no. 5: 599-605. J
- [7] B. Ameliford, F. Fallah, and M. Pedram. 2006. *Reducing the Subthreshold and Gate-tunneling Leakage of SRAM Cells Using Dual- $V_t$  and Dual- $T_{ox}$  Assignment*, *Proceedings of Design Automation and Test in Europe*, 1-6.
- [8] E. Artyomov and O. Y. Pecht. 2006. *Adaptive multiple-resolution cmos active pixel sensor*, *IEEE Transactions on Circuits and Systems* 53, no. 10: 2178-2186. J
- [9] F. Azais, A. Ivanov, M. Renovell, and Y. Bertrand. 1998. *A methodology and design for effective testing of Voltage Controlled Oscillators (VCOs)*, *Proceedings of the Seventh Asian Test Symposium*, 383-387. C
- [10] R. J. Baker. 2005. *CMOS: Circuit Design, Layout and Simulation*, IEEE Press. B
- [11] A. Balijepalli, S. Sinha, and Yu Cao. 2007. *Compact modeling of carbon nanotube transistor for early stage process-design exploration*, *Proceedings of the International Symposium on Low Power Electronics and Design*, 2-7. C
- [12] B. M. Ballweber, R. Gupta, and D. J. Allstot. 2000. *A fully integrated 0.5-5.5 GHz CMOS distributed amplifier*, *IEEE Journal of Solid State Circuits* 35 no. 2: 231-239. J
- [13] S. Basu, B. Kommineni, and R. Vemuri. 2008. *Mismatch Aware Analog Performance Macromodeling Using Spline Center and Range Regression on Adaptive Samples*, *Proceedings of the International Conference on VLSI Design*, 287-293. C

- [14] \_\_\_\_\_. 2008. *Variation Aware Spline Center and Range Modeling for Analog Circuit Performance*, Proceedings of the International Symposium on Quality Electronic Design, 162-167. C
- [15] A. Bellaouar and M. Elmasry. 1995. *Low Power Digital VLSI Design: Circuits and Systems*, Boston: Kluwer Academic Publishers. B
- [16] R. E. Best. 1993. *Phase Locked Loops: Theory, Design and Applications*, McGraw-Hill, 2nd Edition. B
- [17] K. A. Bowman and J. D. Meindl. 2001. *Impact of within-die parameter fluctuations on future maximum clock frequency distributions*, Proceedings of the IEEE Custom Integrated Circuits Conference, 229-232. C
- [18] J. M. Chang and M. Pedram. 1997. *Energy minimization using multiple supply voltages*, IEEE Transactions on VLSI Systems 5, no. 4:436-443. J
- [19] K. B. Cho, A. I. Krymski, and E. R. Fossum. 2003. *A 1.5-V 550  $\mu$ W  $176 \times 144$  Autonomous CMOS Active Pixel Image Sensor*, IEEE Transactions on Electron Devices 50, no. 1:96-105. J
- [20] K. Choi and D. J. Allstot. 2002. *Parasitic-aware design and optimisation of RF power amplifiers*, Proceedings of the IEE Circuits, Devices and Systems 149, no. 5/6:369-375. C
- [21] \_\_\_\_\_. 2004. *Post-optimization design centering for RF integrated circuits*, Proceedings of the International Symposium on Circuits and Systems, 956-959. C
- [22] K Choi and D.J. Allstot. 2006. *Parasitic-aware design and optimization of a CMOS RF power amplifier*, IEEE Transactions on Circuits and Systems I 53, no. 1:16-25. J
- [23] K. Choi, J. Park, and D. J. Allstot. 2003. *Parasitic-aware Optimization of CMOS RF Circuits*, Kluwer Academic Publishers. B
- [24] J. Choudhury and G. H. Massiha. 2004. *Efficient Encoding Scheme for Ultra-Fast Flash ADC*, Proceedings of the 5th Topical Meeting on Silicon Monolithic Integrated Circuits in RF Systems, 290-293. C
- [25] Min Chu, D. J. Allstot, Jeffrey M. Huard, and Kim Y. Wong. 2004. *NSGA-based parasitic aware Optimization of a 5GHz Low-noise VCO*, Proceedings of the Asia South Pacific Design Automation Conference), 169-174. C
- [26] C. Donovan and M. P. Flynn. 2002. *A Digital 6-bit ADC in 0.25 $\mu$ m CMOS*, IEEE Journal of Solid State Circuits 37, no. 3:432-437. J
- [27] J. H. C. Zhan J. S. Duster and K. T. Kornegay. 2004. *A Comparative Study of MOS VCOs for Low Voltage High Performance Operation*, Proceedings of the International Symposium on Low Power Electronics and Design, 244-247. C

- [28] A. Agarwal et al. 2003. *Statistical delay computation considering spatial correlations*, Proceedings of the Asia and South Pacific Design Automation Conference, 271-276.
- [29] A. K. Sultania et al. 2004. *Tradeoffs between Gate Oxide Leakage and Delay for Dual  $T_{ox}$  Circuits*, Proceedings of Design Automation Conference, 761-766. C
- [30] C. Sandner et al. 2005. A 6-bit 1.2Gs/s Low-Power Flash ADC in 0.13 $\mu$ m Digital CMOS, J *IEEE Journal of Solid State Circuits* 40, no. 7:1499-1505.
- [31] C. Shen et al. 2001. *Low voltage CMOS active pixel sensor design methodology with device scaling considerations*, Proceedings of the IEEE Hong Kong Electron Devices Meeting, 21-24. C
- [32] H. C. Tseng et al. 2004. *A Low-Power Rail-to-Rail 6-bit Flash ADC based on a Novel Complementary Average-Value Approach*, Proceedings of the International Symposium on Low Power Electronics and Design, 252-256. C
- [33] L. Wei et al. 1999. Design and Optimization of dual-threshold circuits for Low-Voltage, Low-Power Applications, J *IEEE Transactions on VLSI Systems* 7, no. 1:227-248.
- [34] Liqiong Wei et al. 1999. Design and Opimization of Dual-Threshold Circuits for Low-Voltage Low-Power Applications, J *IEEE Transactions on VLSI Systems* 7, no. 1:16-24.
- [35] M. Liu et al. 2004. *Leakage Power Reduction by Dual  $V_{th}$  designs under probabilistic analysis of  $V_{th}$  variation*, Proceedings of the International Symposium on Low Power Electronics and Design, 2-7. C
- [36] M. Orhansky et al. 2002. Impact of spatial intrachip gate length variability on the performance of high-speed digital circuits, J *IEEE Transactions on Computer-Aided Design* 21, no. 5:544-553.
- [37] O.A. Adeniran et al. 2004. *A CMOS low-power ADC for DVB-T and DVB-H systems*, Proceedings of the International Symposium on Circuits and Systems, 209-212. C
- [38] R. Chau et al. 2000. 30nm physical gate length CMOS transistors with 1.0ps n-MOS and 1.7ps p-MOS gate delays, J *IEDM Technical Digest*, 45-48.
- [39] R. Choi et al. 2002. Fabrication of high quality ultra-thin HfO<sub>2</sub> gate dielectric MOSFETs using deuterium anneal, J *IEDM Technical Digest*, 613-616.
- [40] R. M. Philipp et al. 2007. Linear current-mode active pixel sensor, J *IEEE Journal of Solid State Circuits* 42, no. 11:2482-2491.
- [41] S. Mutoh et al. 1996. A 1-V multithreshold-voltage CMOS digital signal processor for mobile phone application, J *IEEE Journal of Solid State Circuits* 31, no. 11:1795-1802.
- [42] Saibal Mukhopadhyay et al. 2003. Gate Leakage Reduction for Scaled Devices Using Transistor Stacking, J *IEEE Transactions on VLSI Systems* 11, no. 4:716-730.

- [43] T. Kurado et al. 1996. A 0.9-V, 150MHz, 10-mW, 4mm<sup>2</sup>, 2-D Discrete Cosine Transform Core Processor with Variable Threshold (V<sub>t</sub>) Scheme, *IEEE Journal of Solid State Circuits* 31, no. 11:1770-1779. J
- [44] G. Geelen. 2001. *A 6-b 1.1G samples/s CMOS A/D Converter*, Proceedings of the International Solid State Circuits Conference, 127-128. C
- [45] D. Ghai, S. P. Mohanty, and E. Kougianos. 2007. *A 45nm Flash Analog to Digital Converter for Low Voltage High Speed System on Chips*, Proceedings of the 13th NASA Symposium on VLSI Design, 3.1. J
- [46] \_\_\_\_\_. 2008. *A Dual Oxide CMOS Universal Voltage Converter for Power Management in Multi-V<sub>DD</sub> SoCs*, Proceedings of the International Symposium on Quality Electronic Design, 257-260. C
- [47] \_\_\_\_\_. 2008. *A Process and Supply Variation Tolerant Nano-CMOS Low Voltage, High Speed, A/D Converter for System-on-Chip*, Proceedings of the Great Lakes Symposium on VLSI, 47-52. C
- [48] \_\_\_\_\_. 2008. *Parasitic Aware Process Variation Tolerant VCO Design*, Proceedings of the International Symposium on Quality Electronic Design, 330-333. e
- [49] \_\_\_\_\_. 2009. *Design of Parasitic and Process Variation Aware RF Circuits: A Nano-CMOS VCO Case Study*, IEEE Transactions on Very Large Scale Integration Systems. J
- [50] \_\_\_\_\_. 2009. *Variability-Aware Optimization of Nano-CMOS Active Pixel Sensors using Design and Analysis of Monte Carlo Experiments*, Proceedings of the International Symposium on Quality Electronic Design. C
- [51] C. Gopalakrishnan and S. Katkoori. 2003. *Knapbind: an area efficient binding algorithm for low leakage datapaths*, Proceedings of the International Conference on Computer Design, 430-435. C
- [52] \_\_\_\_\_. 2003. *Resource allocation and binding approach for low leakage power*, Proceedings of the International Conference on VLSI Design, 297-302. e
- [53] R. Gupta et al. 1998. *Parasitic-aware design and optimization of CMOS RF integrated circuits*, Proceedings of the IEEE RFIC Symposium, 325-328. C
- [54] A. Hajimiri, S. Limotyrakis, and T. H. Lee. 1999. Jitter and Phase Noise in Ring Oscillators, *IEEE Journal of Solid State Circuits* 34, no. 6:790-804. J
- [55] Chuck Hawkins. 2007. *Little Vias Can Be Vicious*, Proceedings of the 13th NASA Symposium on VLSI Design, 2.1. C

- [56] I. Hwang, S. Lee, and S. Kim. 2000. *A digitally controlled phase-locked loop with fast locking scheme for clock synthesis application*, Proceedings of the IEEE International Conference on Solid-State Circuits, 168-169. C
- [57] F. Ishihara and F. Sheikh. 2004. *Level Conversion for Dual Supply Systems*, IEEE Transactions on VLSI Systems 12, no. 2:185-195. J
- [58] S. Joeres, A. Kruth, O. Meike, G. Ordu, S. Sappok, R. Wunderlich, and S. Heinen. 2004. *Design of a Ring-Oscillator with a Wide Tuning Range in 0.13  $\mu\text{m}$  CMOS for the use in Global Navigation Satellite Systems*, Proceedings ProRISC, 529-535. C
- [59] M. Johnson and K. Roy. 1997. Datapath scheduling with multiple supply voltages and level converters, *ACM Transactions on Design Automation of Electronic Systems* 2, no. 3:227-248. J
- [60] J. Yoo, K. Choi, and A. Tangel. 2001. *A 1-GSPS CMOS Flash A/D Converter for System-on-Chip Applications*, Proceedings of the IEEE Computer Society Workshop on VLSI, 135-139. C
- [61] Z. K. Kalayjian and A. G. Andreou. 2000. *Mismatch in photodiode and phototransistor arrays*, Proceedings of the International Symposium on Circuits and Systems, 121-124. C
- [62] Y. Kanno, H. Mizuno, K. Tanaka, and T. Watanabe. 2000. *Level Converters with High Immunity to Power-Supply Bouncing for High-Speed Sub-1-V LSIs*, Proceedings of the Symposium on VLSI Circuits Digest of Technical Papers, 202-203. C
- [63] J. Kao, S. Narendra, and A. Chandrakasan. 2002. *Subthreshold leakage modeling and reduction techniques*, Proceedings of the IEEE International Conference on Computer-Aided Design, 141-148. C
- [64] K. S. Khouri and N. K. Jha. 2000. *Leakage power analysis and reduction during behavioral synthesis*, Proceedings of the International Conference on Computer Design, 561-564. C
- [65] N.-S. Kim, Y.-J. Yoon, U.-R. Cho, and H.-G. Byun. 2003. *New Dynamic Logic-Level Converters for High Performance Applications*, Proceedings of the IEEE International Symposium on Circuits and Systems, 93-96. C
- [66] D. Kim et al. 2006. *CMOS Mixed-Signal Circuit Process Variation Sensitivity Characterization for Yield Improvement*, Proceedings of the IEEE Custom Integrated Circuits Conference, 365-368. C
- [67] E. Kougianos and S. P. Mohanty. 2009. Impact of Gate-Oxide Tunneling on Mixed-Signal Design and Simulation of a Nano-CMOS VCO, *Elsevier Microelectronics Journal* 40, no. 1:95-103. J
- [68] M. J. Krasnicki et al. 2001. *ASF: A practical simulation-based methodology for the synthesis of custom analog circuits*, Proceedings of the IEEE/ACM International Conference on Computer Aided Design, 350-357. C

- [69] S. H. Kulkarni, A. N. Srivastava, and D. Sylvester. 2004. *A New Algorithm for Improved Vdd Assignment in Low Power Dual V<sub>dd</sub> Systems*, Proceedings of the International Symposium on Low Power Electronics and Design, 200-205. ✓
- [70] S. H. Kulkarni and D. Sylvester. 2003. *Fast and Energy-Efficient Asynchronous Level Converters for Multi-V<sub>DD</sub> Design*, Proceedings of the IEEE International Systems-on-Chip Conference, 169-172. C
- [71] A. Kumar and M. Anis. 2006. *Dual-V<sub>t</sub> Design of FPGAs for Subthreshold Leakage Tolerance*, Proceedings of the 7th International Symposium on Quality Electronic Design, 735-740. ✓
- [72] \_\_\_\_\_. 2007. *Dual-Threshold CAD Framework for Subthreshold Leakage Power Aware FPGAs*, IEEE Transactions on Computer-Aided Design of Integrated Circuits and Systems 26, no. 1:53-66. J
- [73] K. Kwok and C. H. Luong. 2005. Ultra-low-Voltage high-performance CMOS VCOs using transformer feedback, *IEEE Journal of Solid State Circuits* 40, no. 3:652-660. J
- [74] P. Larsson. 1999. A 2 – 1600 –MHz Clock Recovery P<sub>LL</sub> with Low-V<sub>dd</sub> Capability, *IEEE Journal of Solid State Circuits* 34, no. 12:1951-1960. J
- [75] D. Lee, D. Blaauw, and D. Sylvester. 2004. Gate Oxide Leakage Current Analysis and Reduction for VLSI Circuits, *IEEE Transactions on VLSI Systems* 12, no. 2:155-166. J
- [76] D. Lee, J. Yoo, and K. Choi. 2002. *Design Method and Automation of Comparator Generation for Flash A/D Converter*, Proceedings of the International Symposium on Quality Electronics Design (ISQED), 138-142. C
- [77] D. Leenaerts et al. 2001. *CAD solutions and outstanding challenges for mixed-signal and RF IC design*, Proceedings of the IEEE/ACM International Conference on Computer Aided Design, 270-277. C
- [78] F. Li, Y. Lin, L. He, and J. Cong. 2004. *Low Power FPGA using Pre-defined Dual-V<sub>dd</sub>/Dual-V<sub>t</sub> Fabrics*, Proceedings of the International Symposium on FPGAs, 42-50. C
- [79] J. Long, J. Y. Foo, and R. J. Weber. 2004. *A 2.4 GHz Low-Power Low-Phase-Noise CMOS LC VCO*, Proceedings of the IEEE Computer Society Annual Symposium on VLSI, 213. C
- [80] J. McNeill. 1997. Jitter in Ring Oscillators, *IEEE Journal of Solid State Circuits* 32, no. 6:201-204. J
- [81] S. P. Mohanty, D. Ghai, E. Kougianos, and B. Joshi. 2009. *A Universal Level Converter Towards the Realization of Energy Efficient Implantable Drug Delivery Nano-Electro-Mechanical-Systems*, Proceedings of the International Symposium on Quality Electronic Design. C



- [82] S. P. Mohanty and E. Kougianos. 2007. *Simultaneous Power Fluctuation and Average Power Minimization During Nano-CMOS Behavioral Synthesis*, Proceedings of the 20th IEEE International Conference on VLSI Design, 195-200. C
- [96] J. Park, K. Choi, and D. J. Allstot. 2003. *Parasitic-aware design and optimization of a fully integrated CMOS wideband amplifier*, Proceedings of the Asia South Pacific Design Automation Conference, 904-907. C
- [97] M. Pedram and J. M. Rabaey. 2002. *Power Aware Design Methodologies*, Springer. B
- [98] M. J. M. Pelgrom, AAD C. J. Duinmaijer, and A. P. G. Welbers. 1989. Matching Properties of MOS Transistors, *IEEE Journal of Solid State Circuits* 24, no. 5:1433-1440. J
- [99] J. M. Rabaey, A. Chandrakasan, and B. Nikolic. 2003. *Digital Integrated Circuits*. 2nd Ed. Prentice-Hall. B
- [100] B. Razavi. 1996. *Monolithic Phase Locked-loops and Clock Recovery Circuits*, IEEE Press. B
- [101] R. Dehghani and S.M. Atarodi. 2003. Optimised analytic designed 2.5GHz CMOS VCO, *IEE Electronic Letters* 39, no. 16:1160-1162. J
- [102] K. Roy and H. M. Meimand. 2002. *Self-Precharging Flip-Flop (SPFF): A New Level Converting Flip-Flop*, Proceedings of the 28th European Solid-State Circuits Conference, 407-410. C
- [103] K. Roy, S. Mukhopadhyay, and H. Mahmoodi-Meimand. 2003. *Leakage current mechanisms and leakage reduction techniques in deep-submicrometer CMOS circuits*, Proceedings of the IEEE 91, no. 2:305-327. C
- [104] K. Sadeghi, M. Emadi, and F. Farbiz. 2006. *Using Level Restoring Method for Dual Supply Voltage*, Proceedings of the 19th International Conference on VLSI Design, 601-605. C
- [105] T. Sairam, W. Zhao, and Y. Cao. 2007. *Optimizing Finfet technology for high-speed and low-power design*, Proceedings of the ACM Great Lakes symposium on VLSI, 73-77. C
- [106] K. Salama and A. E. Gamal. 2003. Analysis of active pixel sensor readout circuit, *IEEE Transactions on Circuits and Systems-I: Fundamental Theory and Applications* 50, no. 7: 941-944. J
- [107] H. Sanchez, J. Siegel, C. Nicoletta, J. P. Nissen, and J. Alvarez. 1999. A Versatile 3.3/2.5/1.8-V CMOS I/O Driver Built in a 0.2-um, 3.5-nm  $T_{ox}$ , 1.8-V CMOS Technology, *IEEE Journal of Solid State Circuits* 34, no. 11:1501-1511. J

- [108] P. C. S. Scholtens and M. Vertregt. 2002. A 6b 1.6 G sample/s Flash ADC in 0.18  $\mu\text{m}$  CMOS using Averaging Termination, *IEEE Journal of Solid State Circuits* 37, no. 12:1599-1609. J
- [109] Frank Sill, Jiaxi You, and Dirk Timmerman. 2007. *Design of Mixed Gates for Leakage Reduction*, Proceedings of the 17th Great Lakes Symposium on VLSI, 263-268. C
- [110] S. Sinha, A. Balijepalli, and Y. Cao. 2008. *A Simplified Model of Carbon NanoTube Transistor with Applications to Analog and Digital Design*, Proceedings of the International Symposium on Quality Electronic Design, 502-507. C
- [111] B. S. Song, P. L. Rakers, and S. F. Gillig. 2000. A 1-V 6-b 50-M Samples/s Current-Interpolating CMOS ADC, *IEEE Journal of Solid State Circuits* 35, no. 4:647-651. J
- [112] N. Srisantana and K. Roy. 2004. Low Power Design using Multiple Channel Lengths and Oxide Thicknesses, *IEEE Design and Test of Computers* 21, no. 1:56-63. J
- [113] A. Srivastava. 2003. *Simultaneous  $V_t$  selection and assignment for leakage optimization*, Proceedings of the International Symposium on Low Power Electronics and Design, 146-151. C
- [114] A. Srivastava and D. Sylvester. 2003. *Minimizing total power by simultaneous  $V_{dd}/V_{th}$  assignment*, Proceedings of the Design Automation Conference, 400-403. C
- [115] A. Srivastava, D. Sylvester, and D. Blaauw. 2004. *Power minimization using simultaneous gate sizing, dual- $V_{dd}$  and dual- $V_{th}$  assignment*, Proceedings of the Design Automation Conference, 783-787. C
- [116] Maria Stanoeva and Angel Popov. 2005. *Investigation of a Parallel Resistorless ADC*, Proceedings of the International Conference on Computer Systems and Technologies, 8:1-5. C
- [117] S. Sundareswaran, J. A. Abraham, A. Ardelea, and R. Panda. 2008. *Characterization of Standard Cells for Intra-Cell Mismatch Variations*, Proceedings of the International Symposium on Quality Electronic Design, 213-219. C
- [118] C. Svensson, S. Andersson, and P. Bogner. 2006. *On the power consumption of analog to digital converters*, Proceedings of the 24th Norchip Conference, 49-52. C
- [119] K. Uyttenhove and M. Steyaert. 2000. *A 6-bit 1GHz Acquisition Speed CMOS Flash ADC with Digital Error Correction*, Proceedings of the Custom Integrated Circuits Conference, 249-252. C
- [120] Xuejin Wang et al. 2006. *A Novel Parasitic-Aware Synthesis and Verification Flow for RFIC Design*, Proceedings of the 36th European Microwave Conference, 664-667. C



[121] H. S. Weng, R. T. Chang, E. Crabbe, and P. Agnello. 1998. CMOS active pixel image sensors fabricated using a 1.8V , 0.25 $\mu$ m CMOS technology, *IEEE Transactions on Electron Devices* 45, no. 4:889-894. J

[122] H. Wong. 1997 December. *CMOS image sensors-recent advances and device scaling considerations*, International Electron Devices Meeting Technical Digest, 7:201-204. J

[123] C. Xu, W. H. Ki, and M. Chan. 2002. *A low-voltage CMOS complementary active pixel sensor (CAPS) fabricated using a 0.25 $\mu$ m CMOS technology*, *IEEE Electron Device Letters* 23, no. 7:398-400. J

[124] C. Xu, W. Sargeant, K. R. Laker, and J. Van der Spiegel. 2002. *An Extended Frequency Range CMOS Voltage Controlled Oscillator*, Proceedings of the IEEE International Conference on Electronics, Circuits and Systems, 425-428. C

[125] D. Yang and A. El Gamal. 1999. *Comparative Analysis of SNR for Image Sensors with Enhanced Dynamic Range*, Proceedings of the SPIE Electronic Imaging '99 Conference, 197-211. C

[126] J. Yoo, K. Choi, and J. Ghaznavi. 2003. *A 0.07 $\mu$ m CMOS Flash Analog to Digital Converter for High Speed and Low Voltage Applications*, Proceedings of the Great Lakes Symposium on VLSI, 56-59. C

[127] J. Yoo, K. Choi, and D. Lee. 2003. *Comparator Generation and Selection for Highly Linear CMOS Flash Analog-to-Digital Converter*, *Journal of Analog Integrated Circuits and Signal Processing*, 179-187. J

[128] C.-C. Yu, W.-P. Wang, and B.-D. Liu. 2001. *A New Level Converter for Low Power Applications*, Proceedings of the IEEE International Symposium on Circuits and Systems, 113-116. C

[129] C. P. Yuan and Y. C. Chen. 2005. *A Voltage Level Converter Circuit Design with Low-Power Consumption*, Proceedings of the 6th International Conference on ASIC, 309-310. C

[130] G. Zhang, A. Dengi, and L. R. Carley. 2002. *Automatic Synthesis of a 2:1GHz SiGe low noise amplifier*, Proceedings of the IEEE RFIC Symposium, 125-128. C